

Exploration of the Human Purkinje Network in Virtual Populations

Matthias Lange



The
University
Of
Sheffield.

A thesis submitted in partial fulfilment of the requirements for the degree of

Doctor of Philosophy (PhD)

2017

Exploration of the Human Purkinje Network in Virtual Populations

Matthias Lange

Department of Electronic and Electrical Engineering
The University of Sheffield

A thesis submitted in partial fulfilment of the requirements for the degree of

Doctor of Philosophy (PhD)

March, 2017

Abstract

This thesis investigates the Purkinje network (PN) and its dependency on the heart shape (HS) through cardiac simulation on virtual populations (VPs). The heart is a complex organ and essential to the wellbeing of humans; its dysfunction is responsible for more than 27% of all deaths in the UK. The PN delivers the activation impulse to the ventricles of the heart and ensures their synchronous activation. Thus, the morphology of the PN is important, but it varies between species and *in vivo* imaging is not feasible. However, computer simulation could provide an alternative experimental tool.

In simulation of the cardiac electrophysiology, the PN is often replaced by stimulus points on the HS that are fitted to physiological measurements (heart activation times, ECG). Thus, not allowing the study of the PN morphology, nor studies of arrhythmia involving re-entry into the PN. In this thesis, three studies involving explicit models of PNs have been conducted.

First, an efficient algorithm for solving electrophysiology models for the PN is introduced. These allow performing simulations of physiological activations. To minimise the time for simulations, parallelisation with CPU and GPU architectures are investigated, which is of interest for VP studies.

In the second study, false tendons (FTs) are studied, which provide an additional connection from the left bundle branch (LBB) and are potentially beneficial in case of LBB block. Therefore, the reduction in activation times by FT is studied as a function of the HS.

In the third study, an automatically generated VP is used to explore uncertainty in the PN morphology. The conjecture is that the PN structure adapts to the HS. The coverage of the septum and the minimum distance of the PN to the base are varied. The features of the resulting ECG are used to find the PN that gives maximally synchronised contraction.

Aufklärung ist der Ausgang des Menschen aus seiner selbst verschuldeten Unmündigkeit. Unmündigkeit ist das Unvermögen, sich seines Verstandes ohne Leitung eines andern zu bedienen.

Immanuel Kant

Acknowledgement

This work has been supported by many people and the university of Sheffield. Here, I like to take the chance and thank the most influential persons. First, I express my gratitude to Toni Lassila, who supported me through the major part of my thesis. He helped me understand how to write scientific articles, spend much time in reading my text work, and providing me with essential feedback. I also want to thank him for the great many discussion we had on the theoretical considerations of my work, for his advice with experiment design and in conducting the experiments. The support of Toni Lassila is invaluable to me and without it my thesis would not have been possible. Further, I like to thank Luigi Yuri Di Marco for helping me formulating the research question of this thesis, by providing his knowledge and expertise of the heart. He also helped me to write my first publication. Further, I like to thank Simone Palamara for our joint work on the numerical formulation of the electrophysiology problem in the Purkinje network. I also thank my fellow PhD. students for their help, talks, and all the fun we had together. In particular, I like to mention, Isaac Castro Mateos and Nishant Ravikumar who support me with all my concerns on statistics. Finally, I thank Alejandro F. Frangi for offering me the possibility to do my PhD in the topic of my choice.

I also like to highlight the personal support I received. Here the special thanks goes to my family for supported me over a long time. They helped me through my school time, motivated me to study Physiques and supported me during the studies of my PhD.

DECLARATION

I, Matthias Lange, hereby declare that this thesis is the result of my original work and does not include the outcome of work done in collaboration or by other people except where it is specified, acknowledged or cited. I further state that this dissertation as a whole, or part of it, has not been submitted, or, is being concurrently submitted for a degree, diploma or any-other qualification at the University of Sheffield or any other University or similar institution.

Part of this thesis have been extracted from a number of publications, all of which were written primarily by the author of this dissertation, Matthias Lange, during and as a result of this Ph.D. research. Co-authors provided with feedbacks on the manuscripts and/or experiments.

Publications

Published journal articles during the thesis

- [1] **Lange, M.**; Di Marco, L. Y.; Lekadir, K.; Lassila, T.; Frangi and A. F., “In Silico Population Strongly Predicts a Protective Role of False Tendon in Left Bundle Branch Block Cases Protective Role of False Tendon in Subjects with Left Bundle Branch Block: A Virtual Population Study.” *PLoS ONE* 11 no. 1: e0146477.

- [2] Vergara, C.; **Lange, M.**; Palamara, S.; Lassila, T.; Frangi, A. F. and Quarteroni, A. “A coupled 3d-1d numerical monodomain solver for cardiac electrical activation in the myocardium with detailed purkinje network” *Journal of Computational Physics* 308, (2016): 218–238.

- [3] Lekadir, K.; **Lange, M.**; Zimmer, V. A.; Hoogendoorn, C. and Frangi A. F. “Statistically-driven 3D fiber reconstruction and denoising from multi-slice cardiac DTI using a Markov random field model” *Medical image analysis* 27, (2016): 105–116.

Journal articles accepted for publication during the thesis

- [4] **Lange, M.**; Palamara, S.; Lassila, T.; Vergara, C.; Quarteroni, A.; and Frangi A. F. “Improved Hybrid/GPU Algorithm for Solving Cardiac Electrophysiology Problems on Purkinje Networks” *International Journal for Numerical Methods in Biomedical Engineering* (2016)

Published conference proceeding articles during the thesis

- [5] **Lange, M.**; Palamara, S.; Lassila, T.; Vergara, C.; Quarteroni, A. and Frangi A. F. “Efficient numerical schemes for computing cardiac electrical activation over realistic Purkinje networks: method and verification.” *International Conference on Functional Imaging and Modeling of the Heart*, pp. 430-438. Springer International Publishing, 2015.

- [6] Lassila, T.; **Lange, M.**; Porras P, A. R.; Lekadir, K.; Albà, X.; Piella, G.; Frangi, A. F. ”Electrophysiology Model for a Human Heart with Ischemic Scar and Realistic Purkinje Network.” *International Workshop on Statistical Atlases and Computational Models of the Heart*, pp. 90-97. Springer International Publishing (2015).

Contents

1	Introduction: From the Anatomy of the Heart to in silico Electrophysiology Studies of the Heart in Virtual Populations	1
1.1	Thesis Question	8
1.2	Thesis Outline	11
2	Review of Models for Cardiac Electrophysiology	13
2.1	Computational Models of the Heart	15
2.1.1	Geometric Models of the Heart	15
2.1.2	Modelling the Myocardial Fibre Orientation	18
2.1.3	Modelling the Cardiac Activation Sequence	19
2.2	Computational Models of the Purkinje Network	25
2.2.1	Geometrical Modelling	25
2.2.2	Activation Modelling	26
2.3	Computational Models of the Forward ECG	27
2.4	Conclusion	29
3	The Efficiency of a CPU and a GPU-Hybrid Implementation for a Numerical Solver of the Electrophysiology in Purkinje Networks	31
3.1	Motivation	33
3.2	Methods	35
3.2.1	Mathematical Model and Solution Method	36
3.2.2	Hardware Implementation	37
3.3	Numerical Experiments	39
3.3.1	Numerical Error and Convergence	39
3.3.2	Performance Comparison	42

3.4	Conclusion	44
4	A GPU Algorithm for Solving the Cardiac Electrophysiology Problem on Purkinje Networks with Improved Mathematical Consistency	45
4.1	Motivation	47
4.2	Numerical Scheme for Computing Action Potentials in 1-D Networks .	48
4.2.1	Definition and Modification of the Explicit Gap Junction Model	48
4.2.2	Hardware Implementation	51
4.3	Verification of the Proposed Numerical Method	53
4.3.1	Numerical Error and Convergence in Equilibrium	53
4.3.2	Analytical Solution for a Travelling Pulse	56
4.4	Computational Efficiency	63
4.5	Conclusion	66
5	Manual Creation of a Virtual Population to Explore the Benefits of False Tendon in Subjects with Left Bundle Branch Block	69
5.1	Motivation	71
5.2	Methods	73
5.2.1	Ventricular Model	74
5.2.2	The Papillary Muscle	75
5.2.3	Purkinje Fibre Generation	76
5.2.4	Creation of False Tendons	80
5.2.5	Modelling of a Left Bundle Branch Block	81
5.2.6	Ventricular Activation Time Estimation	81
5.3	Virtual Population Experiments and Results	83
5.3.1	Sensitivity of the QRS_d to Different Purkinje Network Topologies	83
5.3.2	Influence of False Tendons on the Ventricular Activation Time .	84
5.3.3	Synchrony in Left and Right Ventricular Activation	88
5.3.4	The Effect of Heart Size and Shape on the False Tendon induced QRS_d Reduction	90
5.4	Limitations	95
5.5	Discussion and Conclusions	96

6	Automatic Creation of a Virtual Population to Investigate the Effect of the Purkinje Network Morphology on the ECG	99
6.1	Motivation	101
6.2	Methods	102
6.2.1	Construction of a Statistical Shape Model of Cardiac Shape . . .	103
6.2.2	The Automatic Pipeline	104
6.2.3	The Surrogate Model	109
6.3	Results	112
6.3.1	Running the Automatic Pipeline	112
6.3.2	Cost Function Behaviour	112
6.3.3	The Surrogate Model	113
6.4	Discussion and Conclusions	114
7	Conclusion and Outlook	121
8	Appendix	127
	Bibliography	130

List of Figures

1.1	Overview of the anatomy of the heart. (a) both atria and both ventricle, illustration from wikimedia CC BY-SA 3.0, https://commons.wikimedia.org/w/index.php?curid=2344163 (b) Ventricles including Purkinje network.	4
1.2	Plan on how to build a model to investigate electrocardiography (ECG) abnormalities caused by false tendons (FT). In a first approach computational less expensive models are build to learn the Purkinje network (PN) and FT model. In a second stage the models are applied to electrophysiology models, leading to electrophysiology model of the heart including the PN and FTs.	9
2.1	Types of surface and volume elements (a) Triangle (b) Tetrahedron	16
2.2	First mode of variation in a statistical shape model of the heart. (a) Shape at minus three standard deviations (b) Mean shape (c) Shape at plus three standard deviations	18
2.3	Simplified structure of the myocardium. Intracellular space (light blue) is insulated by a membrane (red and grey ball) from the extracellular space (white). At the cell membrane charge accumulates (green and yellow) and forms a transmembrane potential (TMP).	20
2.4	Action potential of myocardial cell (red) and a Purkinje cell (black). The four phases of the action potential are labelled	23
2.5	Small tree gown with an L-System. The growing direction is from left to right, and the red dots mark endpoints in the three.	26
2.6	Computational domains for the forward ECG problem.	28

3.1	Workflow for the central processing unit (CPU) (above), and CPU/GPU hybrid (below) implementation. The CPU implementation needs to copy the potential in the gap-junctions and the current, while the hybrid implementation needs to copy the potential of the ghost nodes. White boxes represent CPU tasks, and grey GPU tasks.	39
3.2	The absolute error between the analytic solution of the potential and the numerical solution. For the test case on an infinite line (a), and for the simple branching network (b), where the dotted line has a step size of 0.1 cm, while the solid is 0.00625 cm and the error is multiplied by 10. The active cells are in the region marked with red.	41
3.3	Linear convergence in h (dashed line) and the convergence rates of the potential computed with the CPU (dotted line), and from the CPU/GPU hybrid (solid line). Results are for the single line case (left) and for the simple branching network (right).	42
4.1	Illustration of three Purkinje branches and the gap-junctions that link together the Purkinje cells. The four steps of the algorithm to solve electrophysiological problems are shown. In the middle of the gap-junction are the intracellular potential $\phi_i _g$ and the current I_g . Additional nodes (<i>ghost nodes</i>) are defined to compute the cell membrane model in the cell. All equations are explained in the text.	49
4.2	Detail of the branching node point in the finite element (FE) node points and ghost nodes. The currents $I_{1,2,3}$ are defined from the ghost node the FE nodes.	50
4.3	The workflow for the CPU (above), CPU/GPU hybrid (middle), and GPU (lower) implementation. The CPU needs to copy the transmembrane potential in the gap-junctions and the current, while the CPU/GPU hybrid needs to copy the potential of the ghost nodes. In the GPU implementation there is no copy required.	53
4.4	Problem domains for the equilibrium solutions, where the dashed area are unstable cells. Left for a line segment and right for symmetric bifurcation	54

4.5	Error obtained with different numerical implementations. Upper row: L_2 error as a function of spatial step size h for different implementations; black solid line for CPU, yellow dashed line for hybrid, green dotted line for graphic processing unit (GPU), and red dashed line the comparison with linear convergence rate. (a) solution over one line segment D_1 , (b) over the branching configuration D_2 . Lower row: relative error obtained for the pure-GPU implementation. (c) solution over one line segment D_1 , (d) over the branching configuration D_2 . Blue dotted line corresponds to error for a step size of 0.1 mm, the green solid line the error (enlarged by a factor 10) for step size of 0.00625 mm. The red zone corresponds to the domain of active cells.	57
4.6	Simulation results with the traveling wave. (a) the L^2 error and (b) L^2 -Norm of the solution. The solution was obtained with the CPU (solid), hybrid (dashed) and the GPU (dotted), data shown for a spatial step size of 0.00625 mm. (c) the L^2 error and (d) the conduction velocity after 40 ms against the step discretisation, obtained with the CPU (solid), hybrid (dashed) and the GPU (dotted)	62
4.7	Performance test for two different cell models and four Purkinje networks.	67
5.1	A computed tomography slice and mesh of the left ventricle (red) with the landmarks (yellow). This has been used to build the statistic of the papillary muscle: (1) Attachment point (2) Tip of papillary muscle, (3-4) Landmarks for the diameter estimation.	76
5.2	Different terminations of the false tendon (green) with Purkinje network (PN) (white). (a) False tendon directly connected to the main PN, on a left ventricular surface based on triangles with papillary muscle, where the endocardium is red and the epicardium is blue. (b) False tendon terminating in small Purkinje fibre branching, on a left ventricular volume mesh based on tetrahedra with papillary muscle, with myocardium in red.	78
5.3	The three stages of the Purkinje growing algorithm. (a) First stage with main fibres in blue and endpoints marked by yellow sphere, (b) finer second stage in green and (c) with final branching of the last stage in red.	79

5.4	Myocardial fibre orientation generated with the Streeter model in one exemplary heart.	83
5.5	Shortening given for the direct and delta connected false tendon to various endpoints. The mean QRS duration without false tendon (FT) was 131.9 ± 7.1 ms	85
5.6	Comparison of the activation pattern with and without false tendon for the same heart.(a) The local activation times for the heart without FTs, (b) difference in the activation time of the heart with a FT to the ventricular free wall, (c) the same with a left bundle branch block and a FT to the anterior papillary muscle.	86
5.7	QRS _d prolongation. In a few cases the QRS duration may be prolonged by adding a false tendon. (a) without false tendon, the last point activated is still reached by the wave front from the right ventricle. (b) with false tendon there is an earlier onset of myocardial activation, here seen in the papillary muscle.	88
5.8	Histogram of the QRS _d in the study population (n=70). (a) Cumulative histogram for all sub groups, (b) Histogram for the healthy, the LBBB, all case with direct connected FT and LBBB and all case with delta connected FT and LBBB. (LBBB) left bundle branch block, (PPM) posterior papillary muscle, (APM) anterior papillary muscle, (VFW) ventricular free wall, (FT) false tendon.	89
5.9	Percentage of activated tissue for the healthy heart, the same heart with left bundle branch block (LBBB), for a heart with a direct connected false tendon (FT) to the ventricular free wall and LBBB. The heart in healthy condition and the case of a LBBB with FT are similar, while in case of a LBBB the slope is smaller.	90
5.10	Manual division of the myocardium by a plane in left and right ventricle, used to estimate the activation time in the different ventricles.	91
5.11	The QRS duration (QRS _d) for different sizes of the left ventricle, were a LBBB and a false tendon to the anterior papillary muscle is present. The improvement between the "LBBB, no FT" and "LBBB with FT"-case is given by QRS _{Diff}	93

6.1	Overview of the automatic pipeline for simulation.	103
6.2	The compactness of the statistical shape model.(a) The accuracy dependency on the number of Eigenvectors used. (b) The percentage total variation explained by a given mode of variation. The red line shows the cut-off, such that an accuracy of less $6mm$ (3 pixel) is achieved. . .	104
6.3	The surface reconstruction for the mean. a) mean heart surface mesh b) histogram of triangle surface	105
6.4	Four Purkinje parameter a) free basal area b) control of the left bundle branch (LBB) bifurcation point.	106
6.5	Torso (green), with lungs (blue) forming the torso domain Ω_T and the mean shape of the heart (red) Ω_H	107
6.6	The positioning of the electrodes on the torso, the colouring is according to European standard.	108
6.7	The output of each step in the automatic pipeline. a) Heart surface model b) The Purkinje network (PN) c) The myocardial fibre orientation d) Local activation times of the heart e) Volumetric torso mesh f) The resulting 12 lead electrocardiogram (ECG)	113
6.8	(a) Cost for different separations of the double spike, with the smallest cost for both peaks at the same position ($\mu_1 = \mu_2$). (b) Amplitude of the smaller Gauss-function (N_2) and the second Gauss-function (N_1). .	114
6.9	The cost as predicted from the surrogate model, where the blue circles indicate parameter values for which simulation where performed. The cost is shown in relation to the first shape parameter and (a) the LBB bifurcation point or (b) the right bundle branch (RBB) bifurcation point.	115
6.10	The cost function as predicted from the surrogate model, in relation to LBB bifurcation point and the LBB bifurcation point.	116
6.11	The cost function as predicted from the surrogate model, in relation to the first shape parameter and the free basal area in (a) Left Ventricle (b) Right ventricle point.	117

List of Tables

3.1	The computational time for different Purkinje networks in the left ventricle (LV) and right ventricle (RV).	43
4.1	Comparison of the speed-up in solving the ionic model with previous studies. The speed-up are based on one CPU core, against one GPU. * obtained using 6 CPUs and 6 GPUs. (TP06) model by Ten Tusscher and Panfilov [1], (LR) Model by Luo and Rudy [2], (DFN) model by di Francesco and Noble [3].	66
5.1	Studies of the Prevalence of False Tendons (FTs) in the Human Heart by (a) Autopsy and (b) Echocardiography.	73
5.2	Statistical Parameters of the Anterior Papillary Muscle (APM) and the Posterior Papillary Muscle (PPM), Calculated from Landmarks in the Left Ventricular (LV) Computer Tomography Scans.	77
5.3	Values used for the Deterministic Purkinje Network Growing in the Left Ventricle (LV) [4] and Right Ventricle (RV)	80
5.4	The mean QRS duration for n=70 geometries and different configurations of the heart model, and the proportion with QRS duration longer than the threshold $Q_{d,TH}=120$ ms. (LBBB) Left bundle branch block, (PPM) posterior papillary muscle, (APM) the anterior papillary muscle, and (VFW) the ventricular free wall	87

5.5	For a healthy heart, the same heart with left bundle branch block (LBBB) and the same heart with direct connected false tendon (FT) to the ventricular free wall and LBBB times are compared. The time the action potential needs from the activation of the Bundle of His to the first activation in the left ventricle (LV) and right ventricle (RV) are compared, and the time elapsing from the first activation in the LV/RV to the last activation in the LV/RV. This reveals that in case of LBBB the RV and LV are not synchronous in activation, but a FT reinstates part of the synchrony.	92
5.6	Mean and Standard Deviation of the QRS_{Diff} [ms] in the Different Populations.	94
5.7	Interquartile Range in [ms] of the QRS_d Improvement in each Population and Case.	95
8.1	Initial conditions used for the Stewart et al. 2009 model	129

Acronyms

AP action potential

CPU central processing unit

CRT cardiac resynchronisation therapy

CT computed tomography

ECG electrocardiogram

FEM finite element method

FT false tendon

GPU graphic processing unit

HPC high performance computing

LAT local activation time

LBB left bundle branch

LV left ventricle

MRI Magnetic resonance imaging

PCA principal component analysis

PM papillary muscle

PMJ Purkinje-muscle junction

PN Purkinje network

RBB right bundle branch

RV right ventricle

SSM statistical shape model

TMP transmembrane potential

VFW ventricular free wall

VT ventricular tachycardia

List of Symbols

$:=$	Definition
∇	Nabla operator
$\partial\Omega$	Boundary of the set Ω
$\partial_x f(x, y, z)$	Partial derivative of the function f with respect to x
Φ	Matrix with the Modes of variation of a statistical shape model
ϕ_e	Extracellular potential
ϕ_i	Intracellular potential
ϕ_i^\pm	Intracellular potential in ghost nodes
ϕ_T	Torso potential
σ^*	Equivalent conductivity
σ_e	Extracellular conductivity
σ_i	Intracellular conductivity
φ	Transmembrane potential
\vec{b}	Vector describing the shape in the eigenspace
C_m	Membrane capacity
I_g	Current through the gap-junction
R_g	Gap-junction resistance

S Vector of three dimensional points describing a shape

t Time

u Local activation time

Chapter 1

Introduction: From the Anatomy of the Heart to in silico Electrophysiology Studies of the Heart in Virtual Populations

In this thesis, the focus is on the computational study of the human Purkinje network (PN), which is responsible for the normal activation of the heart [5].

The PN is located in the ventricular part of the heart muscle (Fig. 1.1). The whole heart muscle is formed by four chambers, two smaller (atria) and large (ventricles). Both atria share a common wall, the atrial septum, and both ventricles share the ventricular septum. The right atrium and the right ventricle (RV) are connected by the tricuspid valve, likewise the left atrium and the left ventricle (LV) are connected by the mitral valve. The region separating the atria and ventricle can be approximated with a plane which is called the base of heart. Attached to the mitral/tricuspid valves are the papillary muscles (PMs), which are located in the ventricle. The PMs keep the valves closed during the contraction of the ventricle. While the RV pumps blood to the lungs; the LV pumps it to the body. To pump blood through the body, both ventricles must contract in synchrony with the contraction proceeding from apex towards the base. To ensure this contraction pattern, the ventricles are activated by an electrical impulse, the action potential (AP), which is conducted to the heart muscle by the PN. As such, the PN has a vital role in the synchronisation of the contracting heart, which is essential to human life.

The PN has two functions, the primary is the fast and coordinated conduction of the AP through the ventricle to maintain the apex to base contraction sequence [6–8]. The second function is the back up generation of an AP, in case the sinus node fails [6].

In healthy condition, the AP is generated in the sinus node, which initiates the electrical activation. The sinus node is located in the right atrium and conducts the AP directly to the muscle of the atria. From the atria, the AP is delayed at the atrio-ventricular node, and conducted from the right atria to the RV. In healthy condition, this is the only electrical pathway between atria and ventricles [6].

The atrio-ventricular node form the begin of the electrically insulated fast conduction system of the ventricles. The first part is named bundle of His after its discoverer, the Swiss cardiologist Wilhelm His, Jr. The fibre continues and bifurcates into the left bundle branch (LBB) and the right bundle branch (RBB). The morphology of the subsequent PN depends strongly on the species and is named after the Czech anatomist Jan Evangelista Purkyně. In dogs' and rabbits' hearts, the PN is often detached from the myocardium, while in sheep [4] and human [9] the PN is superficial to the myocardial endocardium. Furthermore, for some animals like sheep and cow the PN

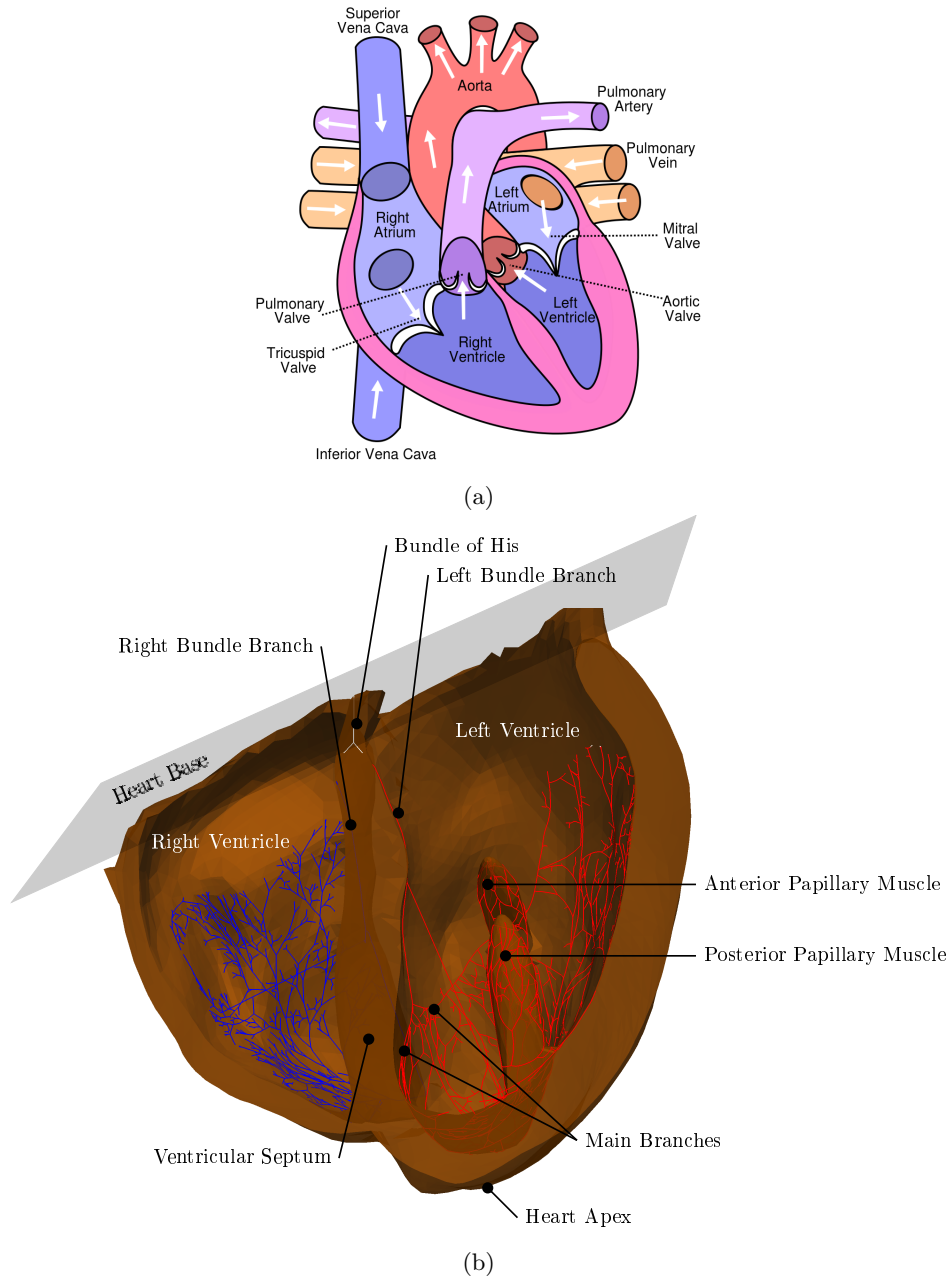


Figure 1.1: Overview of the anatomy of the heart. (a) both atria and both ventricle, illustration from wikimedia CC BY-SA 3.0, <https://commons.wikimedia.org/w/index.php?curid=2344163> (b) Ventricles including Purkinje network.

extends into the myocardium, while in humans the PN is endocardial only [6, 8, 10]. Nevertheless, there are similarities in PNs of the hearts of vertebrates [7].

For humans, it is assumed that the RBB runs in the ventricular septum until it emerges on the right ventricular septum, where it bifurcates. One fibre runs towards the PM and the other towards the right ventricular apex. From the apex, the fibre fans out onto the right ventricular free wall covering large parts of it [5, 11]. However, it is reported that there is no PN on the right ventricular septum.

In case of the LBB, literature is in disagreement whether the LBB ramifies in two or three main branches [8]. These main branches run from their bifurcation to the PMs and from there towards the base of the heart, while bifurcating into smaller branches. These smaller branches cover large parts of the LV endocardium [9]. The fibres in the LV form a dense network with frequent interconnections of fibres.

Beside its physiological function, the PN can be involved in the creation of ventricular tachycardia (VT). VTs are life threatening arrhythmias with heart rates over 120 beats per minute, caused by unphysiological electrical excitation of the ventricle, which results in a high contraction rate of the ventricles without physiological need. This can be the result of slow conduction regions in the PN [6, 12–14]. A common VT has retrograde conduction through one bundle branch and antegrade conduction in the other bundle [6]. Thus, the AP propagates in a closed loop. A further source of arrhythmia is the connection between the PN and the myocardium, in particular in ischemic conditions [15]. A successful treatment of VT is ablation of the tissue region in question [6].

A common variant in the left ventricular geometry are false tendons (FTs). FTs are fibromuscular bands crossing from the left ventricular septum to the PM or ventricular free wall (VFW) [16, 17], and connect different parts of the ventricle. According to Luetmer *et al.* and Kervancioğlu *et al.* [16, 17], most FTs connect the septum and a PM, where Deniz *et al.* reported that most connections are between the septum and the VFW [18]. The FTs, which originating from the septum are usually attached at the basal part of the septum. Other less frequent connections are between two PMs or the PM and the VFW [16]. Frequently, more than one FT is found in a ventricle [19].

The composition of a FT can vary, where the following tissues have been reported: myocardial fibres, blood vessels, connective tissue, fibrous tissue, and conductive tissues [17–19]. Histological examinations showed the presence of Purkinje fibre in 30%

of FTs [19], with the Purkinje fibres being similar to the fibres seen in the bundle of His [20]. The Purkinje fibres can run through the whole FT or alternate with myocardial tissue [18, 21, 22]. Overall, the FT can be an important part of the PN.

FTs are generally assumed to be benign, however, there are reports implicating them in arrhythmias. Abdulla *et al.* conjectured that FTs can give rise to re-entry [17, 20]. Abouezzeddine *et al.* and Betsuyaku *et al.* report cases in which a FT was the origin of a VT. In both cases, ablation of the attachment side cured the VT [23, 24]. It is hypothesised that in the filling phase of the ventricle (diastole) the FT is stretched, and the recurring stretch creates a slow conduction region [24, 25]. This stress is also conjectured to cause premature ventricular contractions [26, 27]. Other case reports indicate that FTs can have a significant influence on the electrocardiogram (ECG). The ECG may show a higher amplitude of the R-wave and an inverted T-wave, features characteristic of ventricular hypertrophy [28, 29].

As discussed above, the PN is of utmost importance to human life, however it is poorly understood. This is related to the fact that the PN is a thin structure, difficult to image *in vivo* with today's imaging technology. Magnetic resonance imaging (MRI) has only been used for some animals where the PN is detached from the myocardium [30]. Other *ex vivo* animal studies injected Indian ink [8] in the network, or use other markers to highlight the PN [11]. However, it would be desirable to study the human heart for information about the human PN, because of the variety in the PN morphology between species. Besides the ethical concerns involved in human studies, the study of the PN is also operationally difficult.

In cases, where *in vivo* studies are infeasible, often models are used to advance the knowledge. This has a long history in the domain of computational modelling of the heart. Already in 1946, a model of the excitation propagation was published and used to describe the propagation in a two-dimensional domain of rectangular shape [31]. This first modelling approaches aimed to reproduce previous clinical observation of activation propagation in simple shapes. Later, these models have been advanced to simulation of the left and right ventricular activation [32], which were usually compared against the measurements conducted by Durrer *et al.* [33]. For these simulations, the parameter values were obtained from different studies usually investigating a single parameter. The investigation leading to the parameter estimation, were often conducted on a single subject, like the myocardial fibre orientation by Streeter [34], or

with average values for the electrical conduction velocity in different tissues, aiming for a general description of an average patient [35]. When modern *in vivo* imaging techniques like computed tomography (CT) and MRI became widely available the development of patient specific computer models started. In such models, the aim was to use as much patient specific parameter values as possible to gain information about the specific case. Generally, the parameter values are limited to the cardiac shape, the outline of ischemic regions [36,37], or measurements of activation time or potential at different endocardial positions [37,38]. Such models allowed *in silico* experiments, where *in silico* describes the fact that the experiment is conducted on a computer [39]. Patient specific modelling [36,40,41] marks the transformation from descriptive modelling to predictive modelling. For the first time cardiac models can be used to predict the outcome of different treatments for a particular patient [42]. Today, large database like the UK Biobank¹ exists and provide patient specific parameter values, like the heart shape, for a huge population. This offers the possibility to perform patient specific cardiac simulations in a large population. In the future, such databases can be used to study the effectiveness of a treatment or a new drug by an *in silico* trial. The aim is to reduce the need for expensive and potentially dangerous clinical trails [39]. Besides that *in silico* trails might be more cost effective, they might also provide more information as to why a drug or treatment failed [39].

In silico trails can be performed over a large database of patient-specific data sets, or by utilising virtual populations. In this thesis, the term virtual population refers to a collection of heart shapes, which are generated from a statistical shape model (SSM). The SSM and the process of generating new heart shapes is explained in Section 2.1.1. The advantage of using a SSM is that the shape of the heart is parametrised, which allows to generated heart shapes of a desired shape. This can be used to generated entire virtual populations without the need for patient images, or to augment a population of real shapes, or enlarge the sample size.

¹Incorporated in England and Wales, registered number 4978912, and registered as a charity in England and Wales, number 1101332. Charity registered in Scotland, number SC039230, <http://www.ukbiobank.ac.uk/>

1.1 Thesis Question

This thesis is part of the bigger vision to explain the rare observation of an enlarged R-spike, and inverted T-wave in the ECG caused by a FT [28,29]. Clinically, the ECG alternations can lead to the mis-diagnose of ventricular hypertrophy [29], which could indicate a serious underlying heart condition, where FTs are assumed to be benign.

Therefore, a way to differentiate between ventricular hypertrophy and the benign FTs is needed. One possible approach is to extract features from the ECG, like the QRS duration, and use machine learning techniques to build a classifier. The machine learning needs large amounts of ECGs data with the same condition (either FT, or ventricular hypertrophy) for the training phase, however this data are not available for the case of FT. A computational model of the heart, including a FT, can potentially provide a replacement for the missing experimental data. The models need to be developed to reproduce the clinically observed indicators of inversion of the T-wave and enlarged R-spike. Then the model can be used in virtual population studies, and thereby the statistical characterisation of the ECG alternations caused by the FT be learned.

To tackle this problem, a model for the PN, FT, and the shape of the heart needs to be developed. The parameter values of the first two models need to be learned from *in silico* experiments reproducing physiological results. A brief overview of the problem is shown in Figure 1.2. The vision includes three crucial parts, first a model of the human PN, second a model of the FT and third the automatic simulation of virtual population studies. Therefore, the thesis aims to study the activation sequence of the human heart for different morphologies of the human PN, including the alternation by a FT, in virtual populations. More specifically, the cardiac activation time is studied in relation to the coverage of the endocardium by the PN. To this end, an automatic pipeline of computer tools is developed to generate new heart shapes from a SSM and perform simulations of electrical activity in the human heart. The pipeline includes a tool for the generation of physiological PN and its morphological variability.

There are multiple challenges on the way: the development of a combined PN and heart model, the automatic creation of the geometries for the heart and the PN, and the integration of all tools, from the creation of the hearts to the simulation of the activation time, in an automatic pipeline. To be able to perform virtual population

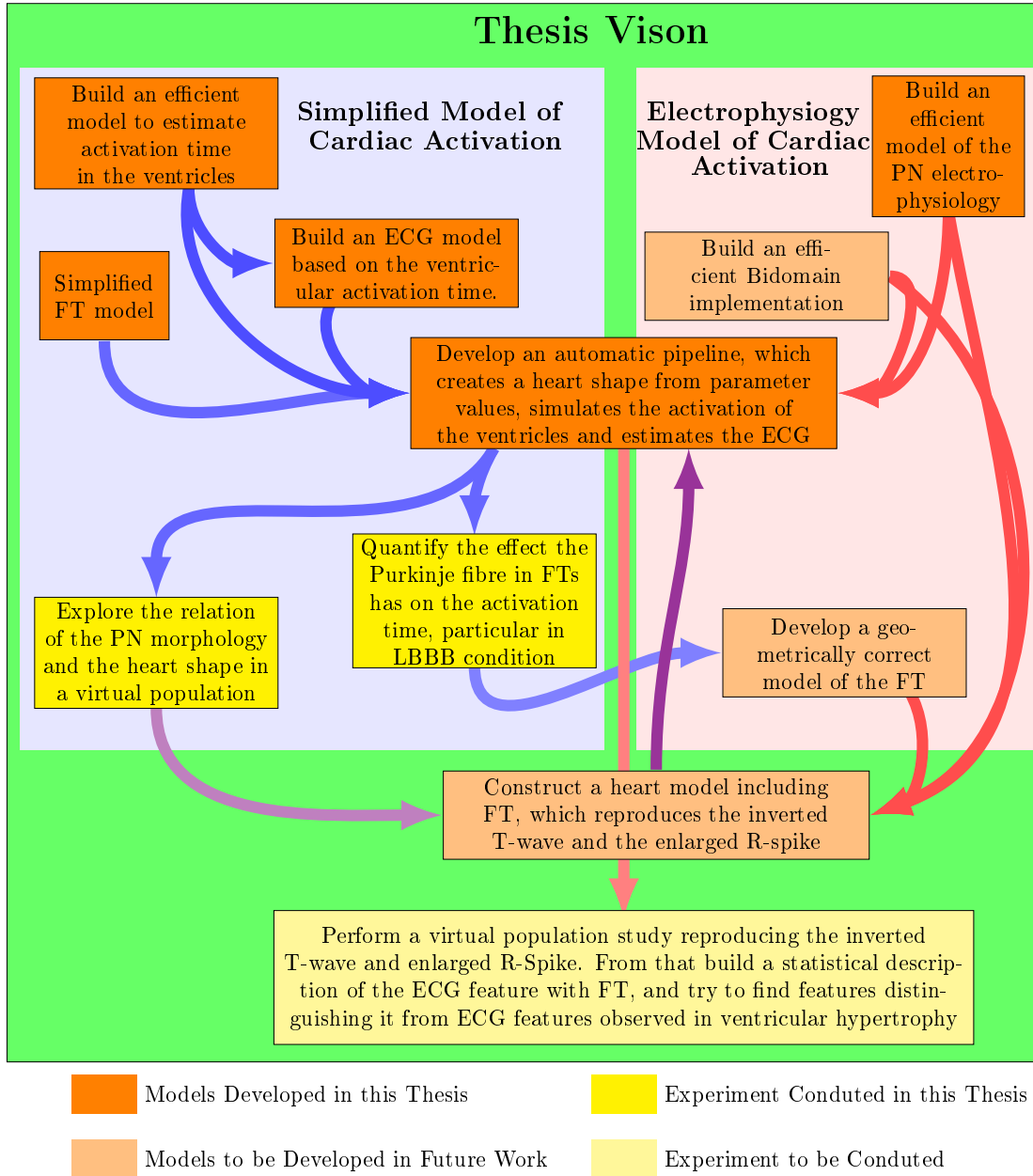


Figure 1.2: Plan on how to build a model to investigate electrocardiography (ECG) abnormalities caused by false tendons (FT). In a first approach computational less expensive models are build to learn the Purkinje network (PN) and FT model. In a second stage the models are applied to electrophysiology models, leading to electrophysiology model of the heart including the PN and FTs.

studies, hundreds of simulations need to be conducted, therefore the automatic pipeline can not include manual intervention by the user. Furthermore, the automatic pipeline should depend on parameters to control the shape of the heart geometry and the PN. The four objectives of this theses are

1. **Build a computationally efficient electrophysiology model of the PN for simulation of virtual populations**

Different models for the simulation of the electrophysiology in the PN exist. Some of these models are able to simulate the propagation of APs through the PN based on ionic exchange mechanisms. However, no special effort has been made to achieve computationally efficient implementations of solvers for the electrophysiology in the PN. As the aim of this thesis is to perform virtual population studies, computational time is critical. Thus, it is important to explore different parallelisation strategies, which should be accompanied by verification studies. The verification ensures that any simplifications made for an efficient solver implementation do not affect the solution accuracy.

2. **Build an automatic pipeline for the construction and execution of a computational heart model.**

To perform virtual population studies of hearts, a manual creation of heart geometries is not feasible. Therefore, an automatic pipeline is developed to create anatomically realistic heart shapes, based on a SSM of the heart. For a systematic generation of virtual populations, the heart shape is controlled by parameters, as should be the coverage of the endocardium by the PN. For a given heart shape and PN, simulations of the activation sequence are performed and used to estimate the ECG.

3. **Perform a virtual population study on the effect of FTs in LBB block condition.**

The FT can connect to the PN, where an additional connection in the PN presents a significant change to the topology of the PN. However, so far no computational model includes them. To study potential benefits provided by the presence of a FT in conduction dysfunction of the PN, a virtual population study is performed. The study examines whether FTs can reduce the prolonged activation time resulting from a dysfunction of the fast conduction system.

4. Explore the relation between the PN morphology in different heart shapes and the simulated ECG.

As the PN varies between species and many studied are based on animals, the knowledge of the human PN has a high degree of uncertainty. This is particular true when it comes to the extent to which the PN covers the endocardium. It can even be conjectured that the PN morphology will influence the synchronicity between activation in the RV and LV. Therefore, this study estimates the effect of the PN morphology on the activation sequence. To explore this, the automatic pipeline from the second objective should be used.

1.2 Thesis Outline

In Chapter 2, previous work completed in cardiac modelling is reviewed, where the focus is on the healthy heart, and the explicit modelling of the PN. Therefore, the review starts with different geometric heart models used in literature and continues with an introduction to mathematical models for cardiac electrophysiology. A derivation of the bidomain model is given, and it is explained how the model can be simplified to arrive to the monodomain or eikonal models. The second focus is on the PN, for which different approaches in modelling and generation of geometrical models are reviewed; a review of electrophysiology modelling of the PN is also provided. The chapter concludes with a brief overview of the mathematical modelling of the ECG.

Chapter 3 introduces different implementations of monodomain based solver for the PN. One implementation relies only on the use of central processing units (CPUs), where the second is a hybrid implementation using both CPUs and graphic processing units (GPUs). The accuracy of both implementations is assessed by constructing a test problem with an analytic solution. However, the convergence test with respect to the spatial discretisation exhibits sublinear convergence. In a subsequent work, presented in Chapter 4, it is shown that the convergence can be improved, by changing the mathematical description of the bifurcation points in the PN. For the revised formulation to solve for the electrophysiology of the PN three implementations are presented: a pure CPU, a pure GPU, and a hybrid implementation. To evaluate the performance of these different implementations the simulation runtime for four different spatial complexities and two different ionic model is compared.

In Chapter 5, a semi-automatic virtual population study is performed. The aim is to quantify the reduction in activation time, which can be achieved by a FT in LBB block condition. Therefore, a virtual population of 70 hearts is semi-automatically created from a SSM. For all hearts, a PN is generated with a deterministic algorithm and simulations of the activation time in LBB block condition are performed. Subsequently, simulations with six different FT configuration are performed to compare the total activation time between cases with and without FT.

In Chapter 6, the effect of the uncertainty in the PN morphology is explored. To that end, an automatic pipeline is developed, which draws instances of heart shapes from a SSM and performs simulations of the ECG. The pipeline uses a parameterisation of the cardiac geometry consisting of 27 shape parameters and four Purkinje morphology parameters. For the cardiac geometry, a SSM of the heart shape is implemented in a computer program to automatically generate a heart surface mesh, based on the shape parameter values. The four Purkinje parameters are used in the PN growing algorithm to control the coverage of the endocardium by the PN. Two Purkinje parameters control the minimum distance of the PN from the heart base in LV and RV, respectively. The other two parameters control the length of the main branches of the LBB and RBB, respectively. The algorithm is integrated in a second computer program. The pipeline is completed by further computer programs: One from the `LifeV` library², which assigns the myocardial fibre orientation, a solver for the local activation times in the heart, and the computer software `SCIRun`³ that obtains the forward ECG solution. The resulting pipeline runs without intervention from the user. Using this pipeline, an experiment is conducted to optimise Purkinje parameter values such that the resulting ECG exhibits only one R-spike.

A summary of the work, and evaluation of the objectives is given in Chapter 7. The chapter concludes with an outlook to future work.

²The `LifeV` (<http://www.lifev.org>) finite element library is the joint collaboration between four institutions: EPFL, Politecnico di Milano, INRIA, and Emory University.

³`SCIRun`: A Scientific Computing Problem Solving Environment, Scientific Computing and Imaging Institute (SCI), Download from: <http://www.scirun.org>

Chapter 2

Review of Models for Cardiac Electrophysiology

In recent years, computer simulations have extended the experimental possibilities in medical applications. Such that, today, computer simulations are used to aid in the planning, operation of surgeries [42, 43], and in *in silico* trials [44, 45]. One reason for this development is that computers have become more powerful and less expensive. The other reason is the continuing advancement in cardiac modelling. In the following section, the theory of computational modelling of the healthy heart is reviewed. The cardiac model is composed of a model for the healthy myocardium, a model of the myocardial fibre orientation, a model of the PN, and finally a model for the ECG.

2.1 Computational Models of the Heart

Computational models of the heart are composed of the heart shape, a model of the inertial stimulation of the myocardium (*e.g.* a PN or carefully selected stimulus sides), the myocardial fibre orientation, and a model of the activation propagation. In this section, an overview of these topics is provided. An exception is the initial stimulus of the heart, which is discussed in more detail in Section 2.2.

2.1.1 Geometric Models of the Heart

The description of the heart morphology is an essential part of the heart model, since it influences [46] both the activation time and sequence (Section 2.1.2). In general, the shape and size of the heart depends on the subject. In particular, the wall thickness may be larger for athletes or patients suffering from diseases like pulmonary hypertension. In this thesis, an additional interest is on the shape. This is because the PN is on the endocardial surface (Chapter 1), and can be greatly affected by the heart shape.

For computer simulations, the heart shape is usually described by a surface mesh, which is often built from triangular elements (Fig. 2.1a). The triangles form a triangulation of the heart surface. To describe the volume enclosed by a surface a volumetric representation is needed. These are usually achieved by filling the volume of interest with tetrahedron (Fig. 2.1b), or other polyhedrons.

Here, the interest is on the surface description of the heart shape. It can be as simple as a tissue slab or as complex as the reconstruction of the heart shape from images. The smaller tissue slabs are used where the effect of interest does not depend on the particular heart shape and can be reproduced in a rectangular shaped

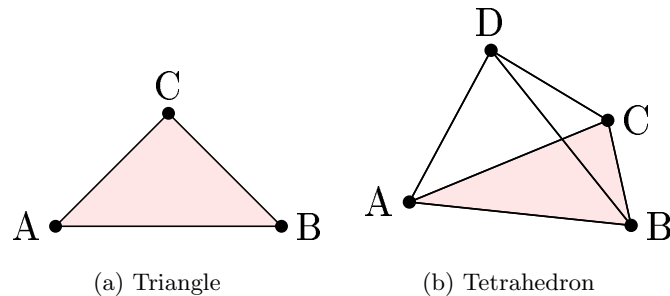


Figure 2.1: Types of surface and volume elements (a) Triangle (b) Tetrahedron

domain [1, 47–52]. Simplified geometries of the LV can be obtained from a truncated ellipsoid [41, 51–53]. These allow the algorithmic generation of the LV, however it is only an approximation of the anatomical shape. The first detailed models of the heart were based on animal studies. Nielsen *et al.* generated an electronic representation from mechanical measurements of ten dog hearts [54]. The position data were then used to approximate the surface with a bi-cubic function, resulting in a smooth representation of the geometry. Stevens *et al.* [55] extended the technique to digitise the shape of a porcine heart to improve the representation of the basal area. Vetter and McCulloch [56] and Tusscher *et al.* [57] constructed a digital heart geometry from photographs of successive short-axis slices of the heart.

In order to get a better *in vivo* volumetric visualisation of the heart, MRI [30, 58–60] or CT [51, 61, 62] is employed. Applying segmentation [63–65] and meshing techniques [66], volumetric meshes of the heart can be constructed from *in vivo* images.

More recently, SSMs of the human heart have been developed [67, 68], which give a statistical characterisation of the shape over a population of hearts. The construction of the model requires a consistent selection of anatomical landmarks for all shapes in the population. There are different methods for the landmark selection including manual annotation, mesh to mesh registration [44, 68], volume to volume registration, parametrisation to parametrisation and population to population methods. After the landmark selection is completed for all different shapes, the corresponding landmarks of the shapes need to be aligned to each other [69, 70]. The alignment puts the shapes at same spatial position, which is necessary to compare the shapes.

From the aligned landmarks the SSM is constructed. Usually, a landmark is a three

dimensional vector $\vec{S} \in \mathbb{R}^3$. Then, the m landmarks \vec{s}^j , $j \in \{1, \dots, m\}$, form the vector

$$\vec{S} = (s_1^1, s_2^1, s_3^1, \dots, s_1^m, s_2^m, s_3^m)^T, \quad (2.1)$$

where the subscript indicates the component and the superscript T the transposed. In this setting, each shape is represented by a $3m$ -dimensional vector of m landmarks, and after n observations there are \vec{S}^i vectors, $i = \{1, \dots, n\}$. The mean shape of the population is constructed by averaging

$$\bar{\vec{S}} = \frac{1}{n} \sum_{i=1}^n \vec{S}^i. \quad (2.2)$$

However, the possible types of deformations in the population are restricted. Therefore, it is common to apply a dimensionality reduction technique to extract the possible modes of variation. The most common technique is principal component analysis (PCA), which performs an eigenvalue decomposition of the covariance matrix. As the number of training cases (n) is commonly much smaller than $3m$, PCA returns $n-1$ modes of variation (non-zero eigenvectors). The eigenvalue (λ_i) associated to each mode provides information about the fraction of total variation described by that mode of variation.

After the PCA is completed, any new shape, $\hat{\vec{S}}$, can be created by:

$$\hat{\vec{S}} := \bar{\vec{S}} + \Phi \cdot \vec{b} \quad (2.3)$$

where Φ is a matrix with the modes of variation and \vec{b} is a vector describing the shape in the eigenspace, commonly named model parameters. As a rule of thumb, the range of variation in the parameters \vec{b}_i is limited to 3 times the standard deviation, $\sqrt{\lambda_i}$, of each mode, which measures their relative influence.

SSMs have been used to describe the shape of the ventricles and atria in the heart [68, 71]. They have even been applied to virtual population studies investigating the influence of shape on the activation time [44] and studying the relation of shape and ischaemia conditions [45]. The advantage of SSMs is that they do not represent only a single instance of the shape but the variability of shape in the entire population used for training. With this information, it is possible to systematically generate new physiological heart shapes with the desired amount of variability.

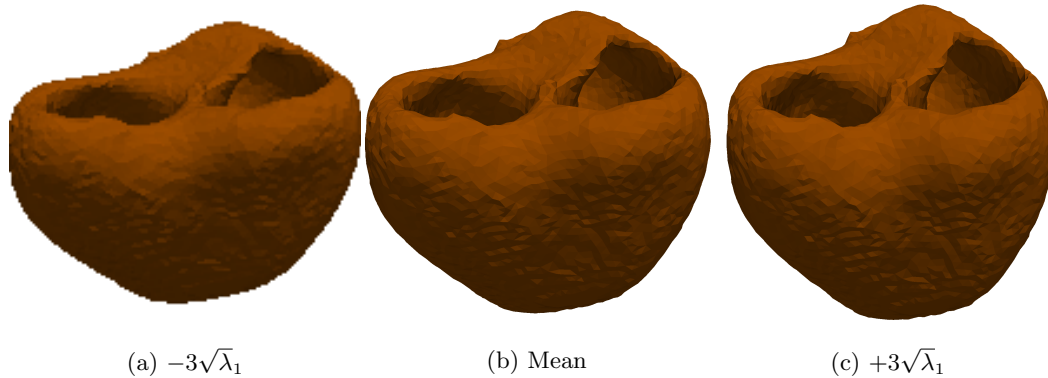


Figure 2.2: First mode of variation in a statistical shape model of the heart. (a) Shape at minus three standard deviations (b) Mean shape (c) Shape at plus three standard deviations

2.1.2 Modelling the Myocardial Fibre Orientation

The heart model includes a model of the myocardial fibre orientation. The myocardial fibre orientation is important for the activation propagation models (Sec. 2.1.3), as the conduction along the myocardial fibre orientation is about twice as fast as perpendicular to it.

In literature, the myocardial fibre orientation is often reconstructed from information obtained *ex vivo*. For simple geometries, like slabs, the myocardial fibre orientation is created artificially [48, 56]. For realistic shaped ventricles, mechanical measurements can be obtained [54], the myocardial fibre orientation can be traced in photographs [57], or reconstructed from diffusion tensor MRI [58]. The advantage of the above methods is that they can provide a personalised myocardial fibre orientation with good resolution. However, the data extraction is performed *ex vivo*.

The statistical descriptions of the myocardial fibre orientation can be used for algorithmic generation. The standard reference for canine myocardial fibre orientations is Streeter *et al.* [34] and is still used frequently. It describes a linear model for the change in fibre orientation transmurally from the endocardium to the epicardium, and from the apex to the heart base. A more detailed model was developed by Lombaert *et al.* [72]. Their model characterises the transmural fibre orientation in each of the 17 segments of the 17 American Heart Association segment model [73]. The advantage of the above algorithmic formulae for fibre orientations is that they can be used to

assign an average fibre orientation to any ventricle, which can also be considered as a limitation as it does not take into account subject-specific fibre orientations.

Combination of a statistical description of the myocardial fibre orientation and the personalised diffusion tensor MRI the personalised high resolution myocardial fibre orientation can be predicted. Such models have been developed in [74]. Advancements of this model would combine the ventricular shape and the myocardial fibre orientation in a single model. This would allow to predict personalised myocardial fibre orientations based in the ventricular shape, only. However, such approaches are still an active topic of research.

2.1.3 Modelling the Cardiac Activation Sequence

In the literature, the main model for cardiac electrophysiology is the bidomain model. Two simplified models of the bidomain model are widely used, the monodomain model and the eikonal model. In the following subsection, an overview of these models is given.

Volume Conductor

First the equations for the electrical potential in a passive medium are derived. The equations will be used in the next section to derive the bidomain equations of the electrical activity of the heart, and in Section 2.3 for the simulation of the ECG. The derivation of the volume conductor follows the work by Sundnes *et al.* [75].

From the laws of electrostatics, the electric field \vec{E} is known and can be written as a potential ϕ

$$\vec{E} = -\nabla\phi. \quad (2.4)$$

In addition, Ohm's law states

$$\vec{J} = \tilde{\sigma}\vec{E}, \quad (2.5)$$

where $\tilde{\sigma}$ is the conductivity tensor and \vec{J} the current. Combining (2.4) and (2.5) results

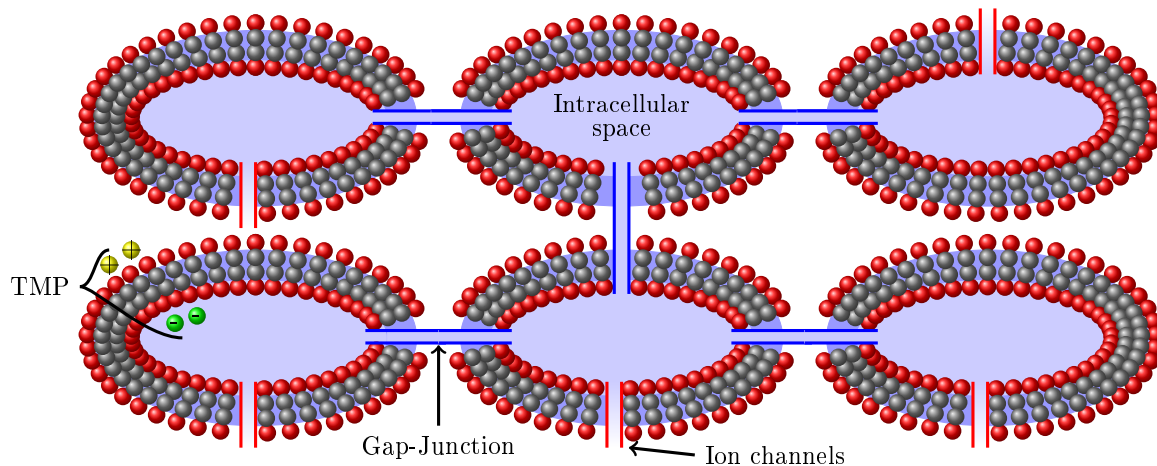


Figure 2.3: Simplified structure of the myocardium. Intracellular space (light blue) is insulated by a membrane (red and grey ball) from the extracellular space (white). At the cell membrane charge accumulates (green and yellow) and forms a transmembrane potential (TMP).

in

$$-\tilde{\sigma}\nabla\phi = \vec{J}. \quad (2.6)$$

This equation describes a volume-conductor.

The Bidomain Model

From the volume-conductor equations (2.6), the bidomain model can be derived. This model is the most detailed representation of cardiac tissue commonly used in literature [48, 76–80].

The bidomain model is based on the observation that in the myocardium the intracellular and the extracellular spaces are separated by a cell membrane (Fig. 2.3). In both domains (2.6) is valid

$$-\tilde{\sigma}_i\nabla\phi_i = \vec{J}_i \quad (2.7)$$

$$-\tilde{\sigma}_e\nabla\phi_e = \vec{J}_e, \quad (2.8)$$

where the subscript i indicates the intracellular space and the e the extracellular space. The physiological assumption that the heart is an electrically closed system means that

the charge in the heart must be conserved. As a consequence, the current can only flow between the intracellular and extracellular space. Therefore, any change in the \vec{J}_i must have opposite change in \vec{J}_e

$$\nabla \cdot \vec{J}_i = -\nabla \cdot \vec{J}_e \quad (2.9)$$

$$\Rightarrow \nabla \cdot (\tilde{\sigma}_i \nabla \phi_i) + \nabla \cdot (\tilde{\sigma}_e \nabla \phi_e) = 0. \quad (2.10)$$

The cell membrane restricts the flow of charged particles between intra- and extracellular spaces, thus the charge accumulates at the cell membrane (Fig. 2.3). Denoting charge at the intracellular membrane q_i and on the extracellular membrane q_e results in the total charge being $q := 1/2(q_i - q_e)$. This charge generates a potential between the intra- and extracellular spaces $\varphi := \phi_i - \phi_e$. The potential can be written in terms of the charge

$$\varphi = \frac{q}{\chi C_m} \quad (2.11)$$

$$\Rightarrow \varphi = \frac{q_i - q_e}{2\chi C_m}, \quad (2.12)$$

where C_m is the capacity of the cell membrane and χ is the surface-to-volume ration. The potential changes as the charge moves through the cell membrane. This is captured in the time derivative

$$\chi C_m \partial_t \varphi = 1/2 \partial_t (q_i - q_e). \quad (2.13)$$

Again, using the assumption of conservation of charge in the heart results in $\partial_t (q_i + q_e) = 0$. This reduces (2.13) to

$$\chi C_m \partial_t v = \partial_t q_i = \partial_t q_e \quad (2.14)$$

Furthermore, the current in a point is equal to the charge accumulation over time and the ionic current through the membrane

$$\begin{aligned} -\nabla \cdot \vec{J}_i &= \partial_t q_i + \chi I_{ion} \\ -\nabla \cdot \vec{J}_e &= \partial_t q_e - \chi I_{ion} \end{aligned} \quad (2.15)$$

Combining (2.14) and (2.15) gives

$$-\nabla \cdot \vec{J}_i = \chi(C_M \partial_t \varphi + I_{ion}). \quad (2.16)$$

Here (2.7) is inserted

$$\nabla \cdot (\tilde{\sigma}_i \nabla \phi_i) = \chi(C_M \partial_t \varphi + I_{ion}). \quad (2.17)$$

This is the second equation of the bidomain formulation. In the two variables (ϕ_e, φ) formulation, the problem becomes

$$\begin{aligned} \Rightarrow \nabla \cdot (\tilde{\sigma}_i \nabla (\varphi + \phi_e)) + \nabla (\tilde{\sigma}_e \nabla \phi_e) &= 0 \\ \nabla \cdot (\tilde{\sigma}_i \nabla (\varphi + \phi_e)) &= \chi(C_M \partial_t \varphi + I_{ion}). \end{aligned} \quad (2.18)$$

With appropriate boundary conditions this problem is known as the bidomain problem.

The problem is completed by the description of ionic current I_{ion} over the cell membrane. The opening and closing of specific ion channels results in change of the transmembrane potential (TMP). This specific dynamic (Fig. 2.4) of the TMP is called action potential (AP), and is formed by five phases. Phase zero is the upstroke of the initial activation, Phase one is the first downward deflection after the upstroke. It follows the plateau phase two in which the AP stays nearly constant, and the repolarisation phase three where the AP return to the resting state, phase four. Hodgkin and Huxley [81] gave the first mathematical model of such an ion current. So far, most ionic models are based on this initial description. They have been developed further to incorporate different ionic channels and are adapted to different cells types. For the myocardium, the Bueno-Orovio (or minimal) model [82] is frequently used, which is adapted to the human myocardium. More complex models for the human ventricular cell are the ten Tusscher-Panfilov model from 2004 [83] and from 2006 [1]. There are other models for animals like the Luo-Rudy model 2 [84]. For the PN, specialised ionic models have been developed. The first model of the ionic dynamics of the Purkinje cell membrane was developed by Noble [85]. It was followed by other models from di Francesco and Noble [3] and the model by Stewart *et al.* [86]. Compared to the models of the myocardium, cell models of the Purkinje cells have a longer AP duration, which is defined as the time from upstroke of the AP to the return to the resting state. A comparison of AP generated by a myocardial cell and a Purkinje cell is shown in

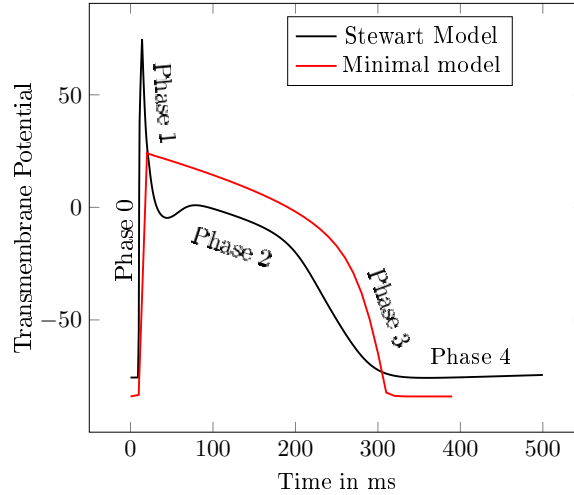


Figure 2.4: Action potential of myocardial cell (red) and a Purkinje cell (black). The four phases of the action potential are labelled

Figure 2.4.

The Monodomain Model

The bidomain model can be simplified to only one potential, assuming a fixed ratio between the intra- and extracellular conductivity at all points

$$\tilde{\sigma}_e := \lambda \tilde{\sigma}_i. \quad (2.19)$$

This simplification reduces the computational complexity [87]. However, it cannot be used where the extracellular potential is explicitly needed, for example in defibrillator simulations [87]. The monodomain approach is frequently used [48, 58, 78–80, 88], where a benchmark test between solvers can be found in the publication by Niederer *et al.* [48].

To utilise the simplification, a rearrangement of the terms in (2.18) is beneficial

$$\begin{aligned} \nabla \cdot (\tilde{\sigma}_i \nabla \varphi) + \nabla \cdot (\tilde{\sigma}_i \nabla \phi_e) &= \chi (C_M \partial_t \varphi + I_{ion}) \\ \nabla \cdot (\tilde{\sigma}_i \nabla (\varphi)) + \nabla \cdot ((\tilde{\sigma}_i + \tilde{\sigma}_e) \nabla (\phi_e)) &= 0. \end{aligned} \quad (2.20)$$

Replacing the extra cellular conductivity and summing both equations

$$\nabla \cdot (\tilde{\sigma}_i \nabla \varphi) - \frac{1}{1 + \lambda} \nabla \cdot (\tilde{\sigma}_i \nabla(\varphi)) = \chi(C_M \partial_t \varphi + I_{ion}) \quad (2.21)$$

$$\Rightarrow \frac{\lambda}{1 + \lambda} \nabla \cdot (\tilde{\sigma}_i \nabla(\varphi)) = \chi(C_M \partial_t \varphi + I_{ion}) \quad (2.22)$$

yields the monodomain equation.

The Eikonal Model

The eikonal model is a different simplification of the bidomain model. The full derivation of the model can be found in [89, 90].

The idea is to only model the local activation time of the heart. The local activation time at a specific location is the time point where the TMP attains the value equal to half of the maximum AP amplitude (Fig. 2.4). In the eikonal model, the evolution of the activation wave-front is modelled, instead of the ionic current. Nevertheless, the eikonal approximation gives a good approximation of the myocardial activation time, as has been shown by different authors [91–93].

In [94] it is shown that from the bidomain equation a simplification can be reached:

$$\partial_x \partial_x w(x) + c_0 \partial_x w(x) + f(w(x)) = 0, \quad (2.23)$$

where w describes a travelling pulse, and c_0 is a dimensionless number quantifying the excitability of the myocardium and $f(u(x))$ depends on the ionic model. The pulse describes the transition from resting potential to the depolarised state. As shown in [90], the travelling pulse can be converted in the local activation time $u(x)$ which is the solution of the problem

$$\rho \sqrt{\nabla u^T M \nabla u} = 1 \quad (2.24)$$

$$u(x_i) = u_0(x_i), x_i \in \mathbb{S} \quad (2.25)$$

ρ is the conduction velocity along the fibre orientation, and M is the symmetric matrix giving the vector along the fibre orientation and the local anisotropy. \mathbb{S} is the set of stimulus points.

This problem can be solved with standard numerical methods, like Euler-forward in-

tegration method. Additionally, it can also be solved with the fast marching method [92]. This method exploits that the activation time increases monotonically from the sources to solve the equation, a more detailed description is given in Section 5.2.6

2.2 Computational Models of the Purkinje Network

2.2.1 Geometrical Modelling

The geometric modelling of the PN has advanced from manually drawing two dimensional networks to the automatic generation of three dimensional PN.

Different methods were used to generate two dimensional PNs. In the simplest construction, the PN was hand drawn [5, 11, 58, 95]. The drawing was guided by measurements of the endocardial activation sequence reported in Durrer *et al.* [33]. A semi manual approach is followed in [5, 46, 96], where the junctions between the PN and myocardium are manually placed. The network between the junctions is automatically generated. Berenfeld and Jalife [97] digitalised representations of the PN from the literature and mapped them to a two dimensional endocardial surface. To fit the images, scaling was applied. Manual corrections were done where the digitalisation produced errors.

Semi-automatic or automatic generation algorithms for three dimensional PNs have been proposed based on fractal L-Systems. An L-System starts from a single branch, which bifurcates, yielding two new branches (Fig. 2.5). Each new branch can stop growing and become an end point or continue bifurcating. Abbound *et al.* [32] introduced this approach to model the PNs as a tree in 1991, where [98] extended the approach to build large networks. In the model, different stages of the PN have then been distinguished, where the first stage is a very coarse network, the second stage is a refinement of the first, and the third stage adds endpoints of the PN. Physiological adaptations to the model have been made to direct the generation of the main bundles towards the PM [4, 99, 100]. Recently, there has been work done to adapt the PN to patient specific endocardial measurements of the activation time [38, 41]

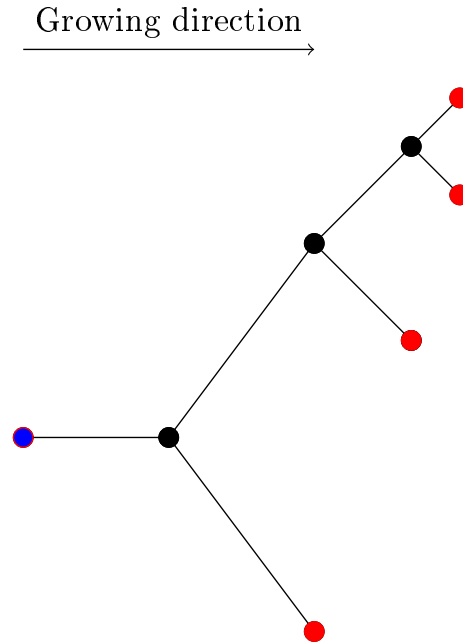


Figure 2.5: Small tree grown with an L-System. The growing direction is from left to right, and the red dots mark endpoints in the three.

2.2.2 Activation Modelling

The PN activation can be modelled with approaches similar to the myocardium (Sec. 2.1.3), as Purkinje cells are specialised myocardial cells. Thus, the activation times can be simulated with a cellular automata model [11], with the eikonal model [38, 101], or the finite element method (FEM) [58, 97, 102, 103]. Berenfeld and Jalife [97] used the monodomain equation and represented the PN as a regular grid, which enabled them to mathematically describe bifurcation of fibres by appropriated coupling condition.

In one dimensional FEM simulations of the PN, bifurcations are modelled by coupling three different branches together. Bordas *et al.* [102] solve the problem by introducing a special finite element basis function at the bifurcation, which linearly interpolates over three domains. For the one dimensional monodomain equation Vigmond and Clements [103] demonstrated a numerical method to solve the problem based on Kirchhoff's current law. In the approach of Vigmond and Clements, the current is obtained using Hermite polynomials, as basis function for the FEM.

2.3 Computational Models of the Forward ECG

The electrical activity of the heart can be measured on the body surface by the ECG, which measures the voltage between different points on the body surface. The numerical simulation of this body surface potential is called the forward ECG problem. In this section, different methods are introduced for the simulation of the surface potential.

For the forward ECG problem, the torso and heart are assumed to consist of two different domains Ω_T and Ω_H , respectively (Fig. 2.6). Then the torso domain is represented as a source free volume conductor, where (2.6) holds. The assumption that the torso is free of electrical charges, and sources is used with the divergence theorem

$$\nabla \cdot \vec{J} = 0. \quad (2.26)$$

Inserting (2.6) and using ϕ_T as the torso potential results in

$$-\nabla \cdot (\tilde{\sigma} \nabla \phi_T) = 0. \quad (2.27)$$

For this problem, the boundary conditions need to be defined. The first being the assumption that no current leaves the body: $\partial_n \vec{J} = 0$ on the torso surface $\partial\Omega_T$, where ∂_n is the derivative in normal direction. At the boundary between the heart and the torso $\partial\Omega_H$, i.e. epicardium, the extracellular potential of the heart ϕ_e and the torso potential ϕ_T are required to be the same $\phi_T|_{\partial\Omega_H} = \phi_e|_{\partial\Omega_H}$. A natural assumption is that all current leaving the heart enters the torso $\partial_n \phi_T|_{\partial\Omega_H} = \partial_n \phi_e|_{\partial\Omega_H}$, which gives the fully coupled model. However, for forward simulations also the stronger no-flux conditions [104] between heart and torso have been used $\partial_n \phi_T|_{\partial\Omega_H} = \partial_n \phi_e|_{\partial\Omega_H} = 0$. This is called uncoupling, as the heart and torso problem are solved separately. In summary, the forward ECG problem is

$$\begin{aligned} -\nabla \cdot (\tilde{\sigma}_T \nabla \phi_T) &= 0, \\ \partial_n \phi_T|_{\partial\Omega_T} &= 0, \\ \partial_n \phi_T|_{\partial\Omega_H} &= \begin{cases} \partial_n \phi_e|_{\partial\Omega_H} & \text{for fully coupled} \\ \partial_n \phi_e|_{\partial\Omega_H} = 0 & \text{for uncoupled} \end{cases}. \end{aligned} \quad (2.28)$$

The fully coupled model is the gold standard. The uncoupled model has the obvious limitations that external pacing can not be simulated. Apart from this limitation, the

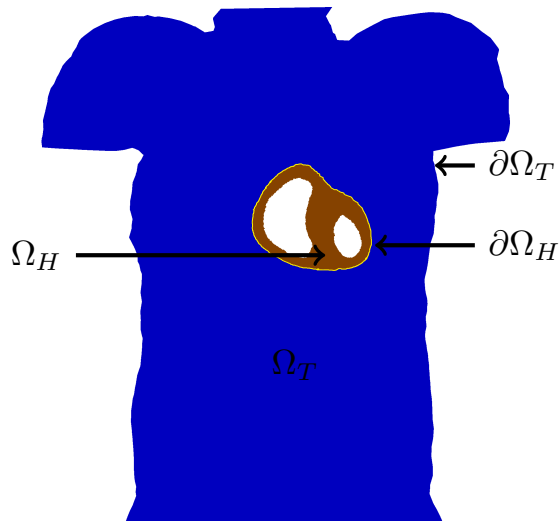


Figure 2.6: Computational domains for the forward ECG problem.

uncoupling can affect the amplitudes of the different waves in the ECG. However, the QRS wave and the QT interval are captured correctly [104].

Another uncoupling approach decouples the intracellular and the extracellular space, by using the TMP instead of the extracellular potential. Assuming the TMP φ is known, the second equation in (2.20) gives the extracellular potential ϕ_e in the heart. The torso potential ϕ_T is given by (2.27), and the problem can be described by

$$\begin{aligned} \nabla \cdot (\tilde{\sigma}_i \nabla(\varphi)) + \nabla \cdot ((\tilde{\sigma}_i + \tilde{\sigma}_e) \nabla(\phi_e)) &= 0. & \forall x \in \Omega_H \\ \nabla \cdot (\tilde{\sigma}_T \nabla(\phi_T)) &= 0. & \forall x \in \Omega_T \end{aligned} \quad (2.29)$$

$$\partial_n \phi_T|_{\partial\Omega_H} = \partial_n \phi_e|_{\partial\Omega_H} \quad (2.30)$$

$$\phi_T|_{\partial\Omega_H} = \phi_e|_{\partial\Omega_H} \quad (2.31)$$

$$\partial_n \phi_T|_{\partial\Omega_T} = 0 \quad (2.32)$$

Thus, ϕ_e is identified with ϕ_T and solved to

$$\begin{aligned} -\nabla \cdot ((\tilde{\sigma}_i + \tilde{\sigma}_e) \nabla(\phi_T)) &= \nabla \cdot (\tilde{\sigma}_i \nabla(\varphi)) & \forall x \in \Omega_H \\ \nabla \cdot (\tilde{\sigma}_T \nabla(\phi_T)) &= 0. & \forall x \in \Omega_T \end{aligned} \quad (2.33)$$

$$\partial_n \phi_T|_{\partial\Omega_T} = 0 \quad (2.34)$$

This way the potential distribution can be computed on the body surface from the TMP only, which can then be used to simulate an ECG. The advantage of this formulation is, that the monodomain equation can be used to describe the AP dynamic in the heart. However, this also means that the limitation of the monodomain model apply here as well.

An estimation of the ECG signal can be obtained by integrating the contribution of the TMP to a particular lead point x_L [47, 58]

$$\phi_T|_{x_L} = \int_{\Omega_H} \nabla\varphi(x) \cdot \left(\tilde{\sigma}_e(x) \nabla \left(\frac{1}{R(x)} \right) \right) d\Omega_H \quad (2.35)$$

where the torso is assumed to have a homogeneous conductivity $\tilde{\sigma}_e$. The function $R(x)$ denotes the distance from x to the lead position x_L .

2.4 Conclusion

In the literature, virtual populations of heart have been created and simulations of their activation times have been previously performed [44, 45]. Some of these techniques can be used or extended to achieve the objectives outlined in Section 1.1.

The geometric model of the heart can be obtained from MRI or CT images. This allows the generation of highly detailed geometric models, which replicate the morphology of the human heart. It has even been shown how to build a SSM of human hearts from CT images [68, 71]. These shape models need to be adapted such that they can be used to build virtual hearts suitable for the volumetric mesh generation and numerical computer simulations.

For the generation of the PN automatic algorithms exist. However, the algorithms in literature need to be extended to generate FTs. Additionally, parameters to control the extent to which the PN covers the endocardium need to be introduced. The best fitting method for the purpose of this thesis is the method from [99] as it is based on physiological observation of the PN structure.

For the modelling of the activation of the heart, existing models can be used. The model choice depends on the specific application, and varies between chapters of this thesis. For the virtual population studies conducted in Chapter 5 and 6 an efficient and computational inexpensive model is needed. As in this thesis only healthy myocardium

is modelled, the model is required to be accurate for healthy myocardium only. The eikonal model is a promising candidate, as simulation can be performed on desktop computers and the activation time approximated with the eikonal model is in good agreement with results obtained from bidomain or monodomain simulations [91–93]. Thus, the eikonal model is an optimal choice for the virtual population studies. On the other hand, the detailed electrophysiology, including the ionic dynamic, of the PN can not be modelled with an eikonal model. Consequently, in Chapter 3 and 4, the monodomain model is used, which is still computationally less expensive than the bidomain main model but can represent the ionic dynamic. The limitation of this approach is that pacing experiments are not possible.

Chapter 3

The Efficiency of a CPU and a GPU-Hybrid Implementation for a Numerical Solver of the Electrophysiology in Purkinje Networks

To be able to conduct virtual population studies, an efficient implementation for the numerical solution of the electrophysiology problem is needed. In this chapter, a numerical solver is presented for the fast conduction system in the heart using both a central processing unit (CPU) and a hybrid CPU/graphic processing unit (GPU) implementation. To verify both implementations, an analytical solution is constructed and it is shown that the L^2 -error between the numerical and analytic solution decreases when shortening the discretisation length. Finally, a performance test of the implementations with networks of varying complexity is performed.

This chapter is adapted from the conference proceeding [105], where the motivation is from [106].

3.1 Motivation

The Purkinje fibres form an extensive branching network of fast conducting cells within the ventricular sub-endocardium of the human heart. This network covers large areas of the ventricles and ensures their rhythmic contraction, in response to signals traversing from the atrioventricular (AV) node along the His bundle and its branches [8,107]. The fibres consist of specialised cardiac muscle cells that conduct the action potential (AP) towards the ventricular myocardium at the Purkinje-muscle junctions (PMJs).

Even if the function of the Purkinje network (PN) is well-known, their involvement in arrhythmia is less well understood. It is suspected that the PN can generate an AP spontaneously [108], or it can be essential to the initiation of some ventricular tachycardias (VTs) [109,110]. The PN can cause VT if a unidirectional block in the main bundle is present. Assuming that the left bundle branch (LBB) has a unidirectional block with no orthodromic conduction (conduction in physiological direction from the bundle of His to the myocardium), but slow antidromic conduction (conduction from the myocardium towards the bundle of His). Then the AP would be conducted through the right bundle branch (RBB) towards the ventricular septum, from where it travels in the direction of the left ventricular PN and enters in the antidromic direction. In antidromic direction the AP can pass through the unidirectional block and arrives at the previously excited PN. If the loop is long enough or the conduction slow enough, the cells in the previously excited PN have passed their absolute refractory period. Thus, a new AP can be generated. Equally, unidirectional blocks downstream in the

PN are believed to form loops and consequently generate VTs [109].

It is challenging to investigate the effect of the PN on arrhythmias in a clinical setting, because the PN is very thin and fragile. This makes it difficult to perform imaging or *in vivo* electrophysiological measurements. However, in recent years *in silico* experiments have become feasible, and can provide information about the PN, which are difficult to obtain from clinical settings [42]. It has even been suggested to include the PN in cardiac simulations designed to aid interventions [42].

As discussed in Section 2.2.2, different models for the PN have been suggested. Including the bidomain [30], the monodomain [36, 103], and the eikonal model [38]. The eikonal model has several limitations, the most significant of which is the absence of an ionic model. This renders the eikonal model impractical for re-entry simulations, or simulations of ischemic processes in the heart because the absolute and the relative refractory period of the cell cannot be simulated. Another limitation is the inability to simulate the physiological delay in the conduction of the AP of 3 ms to 12 ms from the PN to the myocardium at the PMJs. This delay has to be included in the model manually. Another recently observed limitation of the eikonal model has been the assumption of constant conduction velocity, which is not correct due to the push and pull effect [111]. Therefore, the eikonal model has a limited range of applications. Some of these limitations can be overcome if the monodomain model is used.

The monodomain model describes the propagation of the AP based on the ion exchange over the cell membrane. For this model certain observations have been made in conjunction with the PN. Most importantly, it has been shown that coarse networks are not able to reproduce physiological activations [36, 42, 58, 100]. A further indication that the PN needs a certain density comes from the fact that a single PMJ might fail to conduct the AP from the PN to the myocardium. However, if the PMJ density is high enough some PMJs are redundant. Thus, to obtain realistic activation patterns dense networks are required.

High density of the network or ionic model will reflect on the computational costs. Currently, it is possible to solve the monodomain equation on the densest of PN in a few hours, as will be shown. For the simulation of one case this might not be a strong limitation. However, it becomes important when simulations are performed for virtual population studies. In these experiments, a variety of different configurations in shape, size, and possibly dysfunction of the heart are performed. This variation in parameters

leads to large studies with more than 700 simulations, as will be seen in Chapter 5. In such studies, the time demand for simulation of the PN activation with the monodomain model will exceed feasible limits. Therefore, a reduction of the computational time for the numeric solver is required. A reduction of the computational time can be achieved by processing the problem in parallel. High performance computing (HPC) facilities offer this parallel computing power. However, the sparsity structure of the linear system resulting from the PN problem causes a higher communication demand than usual for one dimensional problems. This reduces the speed-up from using multiple CPUs. To overcome the scalability issue shared memory systems can be used. For the current task, the GPU poses a promising choice, as outlined in the next paragraph.

There are two major advantages of the GPU when used with the PN problem. 1) The GPU is a highly parallel shared memory system and 2) the electrophysiology problem in the PN is small enough to fit on one GPU. The first advantage means that a substantial reduction in computational time is expected, as more than 100 cores are processing at the same time. The second advantage relates to the fact that memory is often a limitation when using the GPU, as the memory size is small in comparison to a desktop machine. However, for the PN problem the common amount of 2 GB memory for a GPU is sufficient to store the whole problem. Furthermore, the ionic models can be processed independently of each other. This makes the electrophysiology problem of the PN a good candidate for acceleration with the GPU.

Using new computational devices, like the GPU, can also introduce new errors. Validation of the method would be the best, however all Purkinje models currently lack *in vivo* validation due to difficulties in measuring APs in the subendocardial PN. As such, the importance of numerical verification first and foremost has been identified as a key stepping stone to the wider development and acceptance of numerical models and methods for simulating PN activation [58].

3.2 Methods

First, a briefly explanation of the approach of Vigmond *et al.* [103] is given, and then the implementation on the CPU and on a CPU/GPU hybrid platform are explained.

3.2.1 Mathematical Model and Solution Method

The monodomain equation is considered in one dimension, because the PN can be approximated by a network of 1-D line segments. Here it is assumed that the extracellular space of the myocardium is not affected by the PN, and it is ignored in the following. The monodomain equation (2.22) in one dimension reads

$$\partial_x(\sigma_i(x)\partial_x\varphi(x,t)) = \beta(C_m\partial_t\varphi(x,t) + I_{ion}(\varphi, \xi)), \quad (3.1)$$

where x is the local coordinate, φ is the transmembrane potential (TMP), I_{ion} is the current that flows through the ion channels, ξ are the state variables of the membrane model, β is the surface-to-volume ratio of the cell membrane, σ_i is the intracellular conductivity, and C_m is the membrane capacitance.

To derive a coupling condition between two or more line segments the idea of Vigmond *et al.* [103] is followed. The equations on each line segment are coupled together by a boundary condition resulting from the enforcement of continuity of the potential and the conservation of charges (Kirchhoff's law). To satisfy the boundary conditions, the TMP, φ , and the current, I , are needed. Since $I = \sigma_i\partial_x\varphi$, the spatial derivatives of the TMP need to be computed.

The system is discretised using a cubic Hermite finite element method (FEM), which allows the current I to be recovered as a continuous quantity. In view of the numerical discretization with the FEM, each node of the mesh is assumed to be located in the *gap-junction* between two cells, where the unknowns are the intracellular potential ϕ_i and the current I_g through the *gap-junction*. Two ghost nodes are created on both sides of the *gap-junction*, where the TMP φ_{\pm} , and ionic channel current I_{ion} are defined. The advantage of the ghost nodes is that with the *gap-junction* modelled as a resistor R , the current I_g can be obtained from Ohm's law

$$\varphi_{\pm} = \phi_i - \phi_e \mp \frac{I_g R}{2}, \quad (3.2)$$

where ϕ_e is the extracellular potential, which is taken constant in this chapter. This is because the Purkinje cells have a negligible contribution to the extracellular space in the myocardium.

To correct for the introduced *gap-junction* resistance, the equivalent conductivity

$\sigma^* = (\sigma_i l)/(l + \sigma_i R \pi \rho^2)$ is used, where l is the length of the Purkinje cell and ρ the radius. This means, that σ_i is the conductivity in the cell only, while σ^* is the conductivity of the cell and the *gap-junction*. In this notation (3.1) becomes

$$\partial_x(\sigma^* \partial_x \phi_i^\pm) = \beta(C_m \partial_t \varphi_\pm + I_{\text{ion}}(\varphi_\pm, \xi_\pm)) \quad , \quad (3.3)$$

where ϕ_i^\pm is the intracellular potential in the ghost nodes. Furthermore, an operator splitting technique is applied to (3.3):

$$\begin{cases} \partial_t \varphi + L_1(\varphi) = 0 \\ \partial_t \varphi + L_2(\varphi) = 0 \end{cases} \quad , \quad (3.4)$$

where $L_1 = I_{\text{ion}}$ is part of the differential operator that represents the nonlinear term of (3.3), whereas $L_2 = \partial_x(\sigma^* \partial_x)$ represent the diffusion term of (3.3). A fractional-step method with a discretization of the temporal derivatives by a first-order approximation is introduced, where the superscript n refers to the numerical solution computed at time t^n and each timestep is of size Δt :

$$\frac{\varphi^{n+1/2} - \varphi^n}{\Delta t} = -L_1(\varphi^n), \quad \frac{\varphi^{n+1} - \varphi^{n+1/2}}{\Delta t} = -L_2(\varphi^{n+1}). \quad (3.5)$$

Now the cable equation can be solved in four steps (Algorithm 1). To handle branching and joining of segments in the PN, the node where the three segments join is created three times. The repeated point is used to enforce the boundary conditions, and thus couple together the solutions obtained for the different line segments. In the case that segment 1 bifurcates into segments 2 and 3, the continuity of the potential $\phi_1 = \phi_2 = \phi_3$ is enforced and the conservation of current $I_1 = I_2 + I_3$ is used. This implementation covers the case where segments 1 and 2 join to form segment 3, in which case the coupling condition of the currents is $I_1 = I_3 - I_2$. These boundary conditions are introduced in the FEM system matrix associated to (3.9) and the right hand side.

3.2.2 Hardware Implementation

Next, the CPU and the CPU/GPU hybrid implementations is outlined. The solver for the cable equation uses the FEM in Step 4, and is implemented using the `LifeV`

Algorithm 1 to Solve the Cable Equation with a Splitting Scheme

Step 1. Recover the transmembrane potential φ_{\pm}^n with (3.2) from $I_g^n, \phi_i^n, \phi_e^n$.

Step 2. Solve the first equation of the (3.5), which is the update of the ionic current in the ghost nodes

$$\varphi_{\pm}^{n+1/2} = \varphi_{\pm}^n - \frac{I_{\text{ion}}(\varphi_{\pm}^n, \xi)}{C_m} \Delta t . \quad (3.6)$$

Step 3. Compute $\phi_i^{n+1/2}$ and $I_g^{n+1/2}$ with the new values of $\varphi_{\pm}^{n+1/2}$ in the real node:

$$\phi_i^{n+1/2} = \frac{\varphi_+^{n+1/2} + \varphi_-^{n+1/2}}{2} + \phi_e^n , \quad I_g^{n+1/2} = \frac{\varphi_+^{n+1/2} - \varphi_-^{n+1/2}}{R} . \quad (3.7)$$

Step 4. Use the FEM for the second stage of the operator splitting. By noticing $\phi_i = \frac{\phi_i^+ + \phi_i^-}{2}$ and using the linearity of L_2 , we find:

$$\beta C_m \partial_t (\phi_i - \phi_e) = \partial_x (\sigma^* \partial_x \phi_i) . \quad (3.8)$$

Introducing a discretization in time results in:

$$\beta C_m \frac{(\phi_i^{n+1} - \phi_e^{n+1}) - (\phi_i^{n+1/2} - \phi_e^n)}{\Delta t} = \partial_x \sigma^* \partial_x \phi_i^{n+1} , \quad (3.9)$$

which is solved with the FEM with 1-D cubic Hermite shape functions.

library¹. Only Steps 1-3 of the algorithm are parallelised and the linear system in Step 4 is solved serially. The reason for this is that the solution of the Ionic model can be advanced in time, independent from the heart mesh geometry and is computationally intensive. On the other hand, it is less trivial to parallelise the solving of the linear system. The resulting computational workflow is shown in Figure 3.1.

The Steps 1, 3, and 4 are always implemented on the CPU, only Step 2 is run on the GPU. In the hybrid implementation, between Steps 1 and 2, an additional copy of the TMP φ_{\pm} from the CPU to the GPU is made. To minimize the time spent copying the data, CUDA² streams are used, which allow asynchronous tasks to be queued to the GPU. All computations are performed with a Dell Precision-WorkStation-T7500 featuring two Intel(R) Xeon(R) CPUs E5620 at 2.40GHz and NVIDIA Quadro 4000 GPU with 256 CUDA Cores.

¹The **LifeV** (<http://www.lifev.org>) finite element library is the joint collaboration between four institutions: EPFL, Politecnico di Milano, INRIA, and Emory University.

²The **CUDA** (<http://docs.nvidia.com/cuda/>) toolkit is of the NVIDIA cooperation

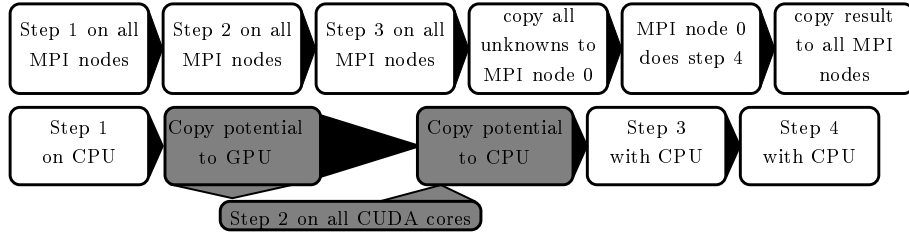


Figure 3.1: Workflow for the CPU (above), and CPU/GPU hybrid (below) implementation. The CPU implementation needs to copy the potential in the gap-junctions and the current, while the hybrid implementation needs to copy the potential of the ghost nodes. White boxes represent CPU tasks, and grey GPU tasks.

3.3 Numerical Experiments

To verify the correct and efficient implementation of the solvers, two numerical experiments are performed. The first experiment uses an analytical solution to estimate the absolute error and then to carry out a convergence test. The second experiment compares the performance of the CPU and CPU/GPU hybrid algorithm.

3.3.1 Numerical Error and Convergence

First, a simplified model is introduced and two test problems with analytical solutions are developed. The non-physiological ionic model is [112]

$$\partial_t \varphi = p\varphi, \quad (3.10)$$

where φ is the TMP and p is a model parameter. Depending on the sign of p the cells are stable ($p < 0$) and return exponentially to 0, or are unstable ($p > 0$) and the TMP increases exponentially.

Next, two different test cases are introduced and their analytical solution is derived. For the first case the domain D_1 considered is an infinite line, which is composed of three subintervals $D_{1,1} = (-\infty, -a)$, $D_{1,2} = [-a, a]$, and $D_{1,3} = (a, \infty)$. In $D_{1,2}$ unstable cells are assumed, while in the surrounding regions $D_{1,1}$, $D_{1,3}$ the cells are

stable, which results in a spatial varying parameter of the simplified model

$$p(x) = \begin{cases} p_2 & \text{for } x \in D_{1,2} \\ -p_1 & \text{otherwise} \end{cases}, \quad (3.11)$$

where $p_1, p_2 > 0$. Inserting the cell model in (3.1), results in the following equation to solve

$$\begin{aligned} C_m \partial_t \varphi &= \delta \partial_x^2 \varphi - p(x) \varphi \\ \varphi_1(-a) &= \varphi_2(-a), \quad \varphi_2(a) = \varphi_3(a) \\ \varphi_1'(x)|_{x=-a} &= \varphi_2'(x)|_{x=-a}, \quad \varphi_2'(x)|_{x=a} = \varphi_3'(x)|_{x=a}, \\ \varphi_1(-\infty) &= 0, \quad \varphi_3(\infty) = 0, \end{aligned} \quad (3.12)$$

with $\delta = \sigma^*/\beta$. The solution presented by Artebrant *et al.* [112] is

$$\varphi = \begin{cases} c_1 e^{\sqrt{p_1/\delta} x} & x < -a \\ \cos(\sqrt{p_2/\delta} x) & \|x\| \leq a \\ c_1 e^{-\sqrt{p_1/\delta} x} & x > a \end{cases} \quad \text{with,} \quad \begin{aligned} p_1 &= p_2 \tan^2(\sqrt{p_2/\delta} a), \\ c_1 &= \cos(-\sqrt{p_2/\delta} a) e^{\sqrt{p_1/\delta} a} \end{aligned}, \quad (3.13)$$

where a and p_2 are the model parameters.

In the second test case, the domain D_2 is a double-bifurcation with an analytical solution. The domain consist of two rays, $D_{2,1} = (-\infty, -a)$ and $D_{2,2} = (-\infty, -a)$ joining to form a line segment $D_{2,3} = [-a, a]$ in the middle, which then splits again into two rays $D_{2,4} = (a, \infty)$, $D_{2,5} = (a, \infty)$, resulting in a domain of five subintervals in total. The line segment $D_{2,3}$ consists of active cells, while $D_{2,1}$, $D_{2,2}$, $D_{2,4}$ and $D_{2,5}$ consist of passive cells. The problem is symmetric with respect to zero, thus only one half of the entire problem domain is of interest. Furthermore, the rays $D_{2,1}$ and $D_{2,2}$ are identical, thus it suffices to solve the following problem for only one of them:

$$\begin{aligned} \delta \varphi_1'' - p_1 \varphi_1 &= 0, & \forall x \in D_{2,1} \\ \delta \varphi_3'' + p_2 \varphi_3 &= 0, & \forall x \in D_{2,3} \\ \varphi_1(-a) = \varphi_3(-a) &, & 2 \varphi_1'(x)|_{-a} = \varphi_3'(x)|_{-a}, \quad \varphi_1(-\infty) = 0, \end{aligned} \quad (3.14)$$

where the factor of two in the derivatives is a result of Kirchhoff's current law. The solution is very similar to the problem on one infinite line, with the ansatz functions $\varphi_1 = c_1 e^{k_1 x}$, $\varphi_3 = c_3 \cos(k_2 x)$ the constant c_1 is still given by (3.13). A relation between

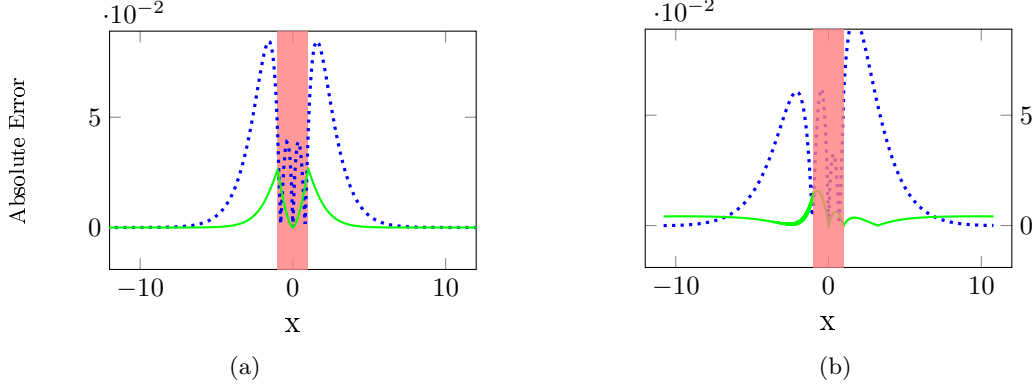


Figure 3.2: The absolute error between the analytic solution of the potential and the numerical solution. For the test case on an infinite line (a), and for the simple branching network (b), where the dotted line has a step size of 0.1 cm, while the solid is 0.00625 cm and the error is multiplied by 10. The active cells are in the region marked with red.

p_1 and p_2 follows from

$$\begin{aligned}
 2\varphi_1'(-a) &= \varphi_3'(-a) \\
 \stackrel{(3.13)}{\Rightarrow} 2k_1(c_3 \cos(-k_2a)e^{k_1a})e^{-k_1a} &= -k_2c_3 \sin(-k_2a) \\
 \Rightarrow p_1 &= \frac{p_2}{4} \tan^2(\sqrt{p_2/\delta}a).
 \end{aligned} \tag{3.15}$$

Again, φ_3 is fixed at one point to get a unique solution.

Comparison of the Absolute Error:

For numerical simulations, the parameter values $p_2 = 1 \text{ kS}$, $a = 1 \text{ cm}$, $C_m = 1 \text{ }\mu\text{F}$, and $c_2 = 1 \text{ mV}$ are used. The length has been chosen to $l = 62.5 \text{ }\mu\text{m}$, and a radius of $\rho = 16.0 \text{ }\mu\text{m}$, which is within the physiological limits [113]. Furthermore, the arbitrary choice $\delta = 1 \text{ kS/cm}^2$, $R = 0.1 \text{ k}\Omega$ is made. Recall that $\delta = \sigma^*/\beta$, from which the conductivity $\sigma_i = 1967 \text{ kS cm}^{-1}$ is found. The spatial discretisation step h is then chosen to be an integer multiple of l , i.e. $h = nl$, $n \in \mathbb{N}$. By choosing the discretisation a multiple of the cell length, it is ensured that the explicit gap-junctions are modelled at actual cell to cell connections. Additionally, this choice ensures the compatibility of the equivalent conductivity and the explicit gap-junction, as the homogenisation is over the cell conductivity and the gap-junction conductivity.

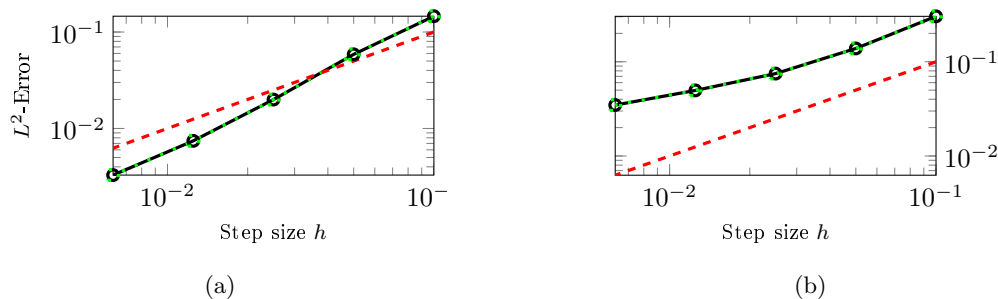


Figure 3.3: Linear convergence in h (dashed line) and the convergence rates of the potential computed with the CPU (dotted line), and from the CPU/GPU hybrid (solid line). Results are for the single line case (left) and for the simple branching network (right).

Convergence Test:

For the error convergence test, the simulations were run with the same parameters as before for $n = \{1, 2, 3, 4, 5\}$ in the spatial discretisation and the L^2 -Error was calculated for each step size (Fig. 3.3). The CPU and CPU/GPU hybrid implementation give the same linear convergence of the error for the test with the line segment D_1 and a sublinear convergence for the domain D_2 . As the FEM uses Hermite polynomials a fourth order convergence would be expected. The only linear convergence is likely to be due to the usage of the virtual nodes in Step 1 and 3 of the algorithm 1, because linear approximation over the gap-junction is used. The sublinear convergence in the domain D_2 is related to a mathematical inconsistent formulation of the gap-junction, as will be discussed in more detail in Chapter 4.

3.3.2 Performance Comparison

To compare the efficiency of the two implementations, four PNs were generated with the method described in Section 5.2.3. The last two PNs have density consistent with physiological PNs for the left ventricle (LV) and for both ventricles, respectively. The simulation was performed with a spatial resolution of 0.1 mm and a temporal step size of 0.02 ms. The duration of 45 ms was chosen because all networks were fully depolarised by that time. The membrane model of Di Francesco-Noble was used [3]. The CPU code was run with eight parallel processes, while the hybrid code was run with one CPU. Table 3.1 shows both the PNs and the total computational time spent

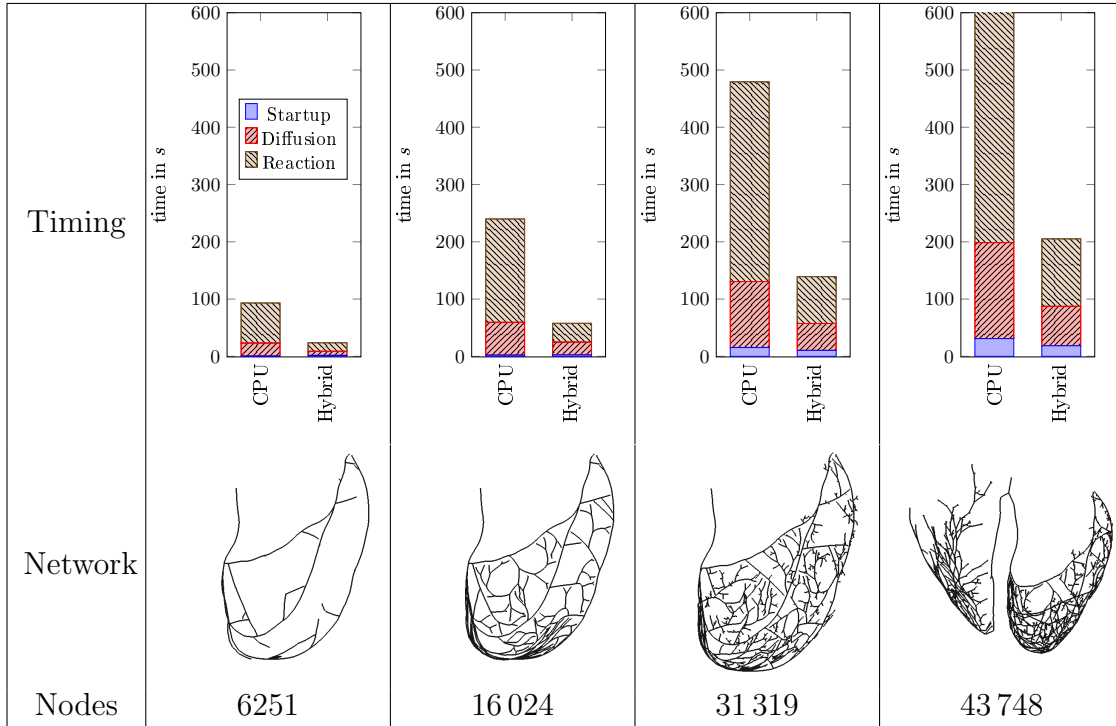


Table 3.1: The computational time for different Purkinje networks in the left ventricle (LV) and right ventricle (RV).

obtaining the respective solutions. Furthermore, the same figure shows the time spent solving the diffusion problem and the reaction problem separately. In the pure CPU implementation, the majority of the time is used to solve the ionic models. This is due to the fact that a detailed ionic model with 15 state variables was used, while the linear system for the diffusion step is comparably simple to solve, as the moving activation front is limited to the vicinity of a few node points. For the hybrid implementation the situation changes, and the time for solving the reaction and diffusion steps are roughly the same, because the GPU offers a larger number of parallel cores. As a result the solution of the reaction step is ca. 4.7 times faster with the GPU. Also, a decrease in the time spent solving the diffusion step is noticed. This can be a result of several factors, including that for the CPU implementation all eight processes need to copy there data to a single CPU.

3.4 Conclusion

An extension of the work of Vigmond *et al.* [103] was presented, to solve realistic PNs, and implemented it both on a CPU and in a hybrid CPU/GPU architecture. To evaluate the accuracy of both implementations a convergence test of the L^2 -Error was calculated over a line, which showed that the solver converges linearly with the step size. The branching points introduced a small additional error in the numerical solution, causing a sub-linear convergence. Both implementations had equivalent numerical accuracy.

The performance test indicated that the hybrid implementation using 256 CUDA cores and 1 CPU was in average 5.8 times faster than the CPU implementation run with 8 CPUs. This motivates future work on developing an implementation, which performs all the remaining steps of the algorithm on the GPU to realize even greater performance gains.

Chapter 4

A GPU Algorithm for Solving the Cardiac Electrophysiology Problem on Purkinje Networks with Improved Mathematical Consistency

In the previous Chapter, the efficient implementation of a numerical solver for the electrophysiology problem in the Purkinje network (PN) has been investigated. It was shown that the graphic processing unit (GPU) offers a powerful computational device, which can be used to reduce computation times in numerical simulations. However, the convergence test in a bifurcating fibre yielded unsatisfactory results. In this chapter the formulation of the gap-junction model is changed to obtain a better convergence rate. Furthermore, the numerical test is extended to time dependent solutions.

This chapter is adapted from the journal publication [106].

4.1 Motivation

The algorithm in Chapter 3 showed a sub-linear convergence of the numerical solution if a bifurcation point was present. This indicates a potential problem in the mathematical formulation of the gap-junction formulation. Consequently, a revised numerical method, which is mathematically more consistent is presented. As electrophysiology measurements are widely unavailable at this time validation is not possible, thus verification is performed. In Chapter 3 only the static solution has been verified. This is insufficient, as the electrophysiology problem is a dynamic problem. Thus, the verification is performed for a time dependent problem in this chapter.

Furthermore, the last chapter showed that the GPU is a strong computational device. Already the hybrid implementation between central processing unit (CPU)/GPU out performed the pure CPU more than 5 times. This motivates a pure GPU implementation to reduce the computational time further, and potentially outperform the hybrid implementation. To investigate this a comparison concerning the performance of the implementations is made. Therefore, four different PNs are created, where the smallest one has 6251 nodes and the largest one has 43748 nodes. The electrophysiology for these networks is simulated with two different ionic models: the model developed by di Francesco and Noble [3] and with the model developed by Stewart et al. [86].

4.2 Numerical Scheme for Computing Action Potentials in 1-D Networks

4.2.1 Definition and Modification of the Explicit Gap Junction Model

To solve the action potential (AP) in the PN, the algorithm from Chapter 3 is improved. Again, the one-dimensional cable equation is extended to describe the propagation of the potential at the branching points. Each Purkinje branch is modelled as a separate problem on a one-dimensional line segment, which is then coupled to other branches by interface conditions determined by the continuity of potential and Kirchhoff's current law. For the latter, the input and output currents at the branching points are needed, which for example can be obtained from a numerical derivative of the potential. As in the previous chapter, the finite element method (FEM) is applied using Hermite basis functions, such that the derivatives of the solutions are degrees of freedom in the formulation.

To close the monodomain equations approximated using Hermite basis functions, the concept of explicit gap-junction models is introduced. This involves writing Kirchhoff's laws at the bifurcations explicitly in terms of the currents and potentials. Gap-junctions are specialised intercellular connections between Purkinje cells. In the classical monodomain model for the myocardium, the effect of these gap-junctions is conflated into the conductivity tensor by a homogenisation process [114]. In the types of models considered for the PN in this work, all gap-junctions between two cells are homogenised into a single gap-junction (Fig. 4.1). This gap-junction is then modelled explicitly [103, 115]. Also, the bifurcation is modelled based on the homogenisation formula. This allows to model bifurcations with a single gap-junction connecting three cells, in order to correctly capture the slow down of the AP propagation when approaching a bifurcation and the acceleration there after ("push-and-pull" effect).

Let us consider the case of two Purkinje cells connected by a gap-junction (inset of Fig. 4.1). Then the degrees of freedom of the problem are the intracellular potential ϕ_i and the current I_g across the gap-junction, where I_g relates to ϕ_i by the derivative:

$$I_g = \pi \rho^2 \sigma_i^* \left. \frac{\partial \phi_i}{\partial l} \right|_g, \quad (4.1)$$

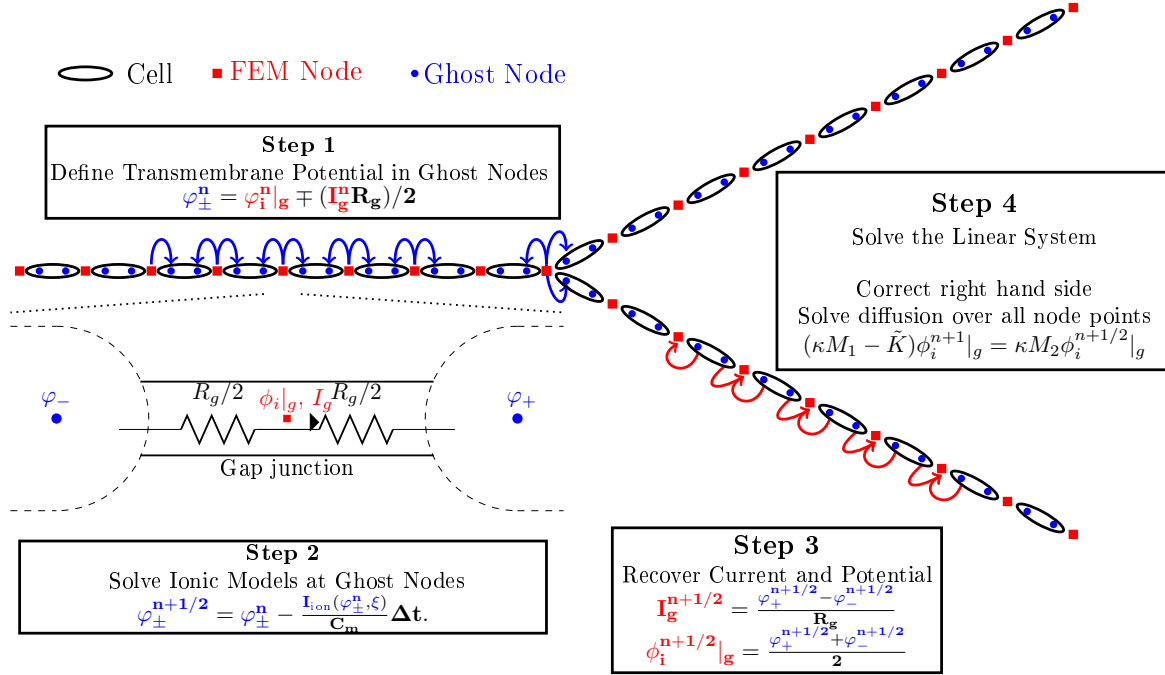


Figure 4.1: Illustration of three Purkinje branches and the gap-junctions that link together the Purkinje cells. The four steps of the algorithm to solve electrophysiological problems are shown. In the middle of the gap-junction are the intracellular potential $\phi_i|_g$ and the current I_g . Additional nodes (*ghost nodes*) are defined to compute the cell membrane model in the cell. All equations are explained in the text.

where σ_i^* is the equivalent conductivity defined later, ρ the Purkinje cell radius and l the cell length. Both quantities I_g and $\phi_i|_g$ are formally located in the middle of the gap-junction (in red in Fig. 4.1). The ionic channel current I_{ion} is calculated in the cells at the ghost nodes (in blue in Fig. 4.1), which means for each node point the cell membrane model needs to be evaluated twice.

The relation between the intracellular potential ϕ_i in the gap-junction and the transmembrane potential (TMP) in the two neighbouring cells φ_{\pm} is given by Ohm's law

$$\varphi_{\pm} = \phi_i - \phi_e \mp \frac{I_g R_g}{2},$$

where R_g is the gap-junction resistance and ϕ_e is the extracellular potential. The latter is assumed to be constant throughout this chapter. Furthermore, up to a multiplicative factor I_g represents the derivative of ϕ_i by Ohm's law.

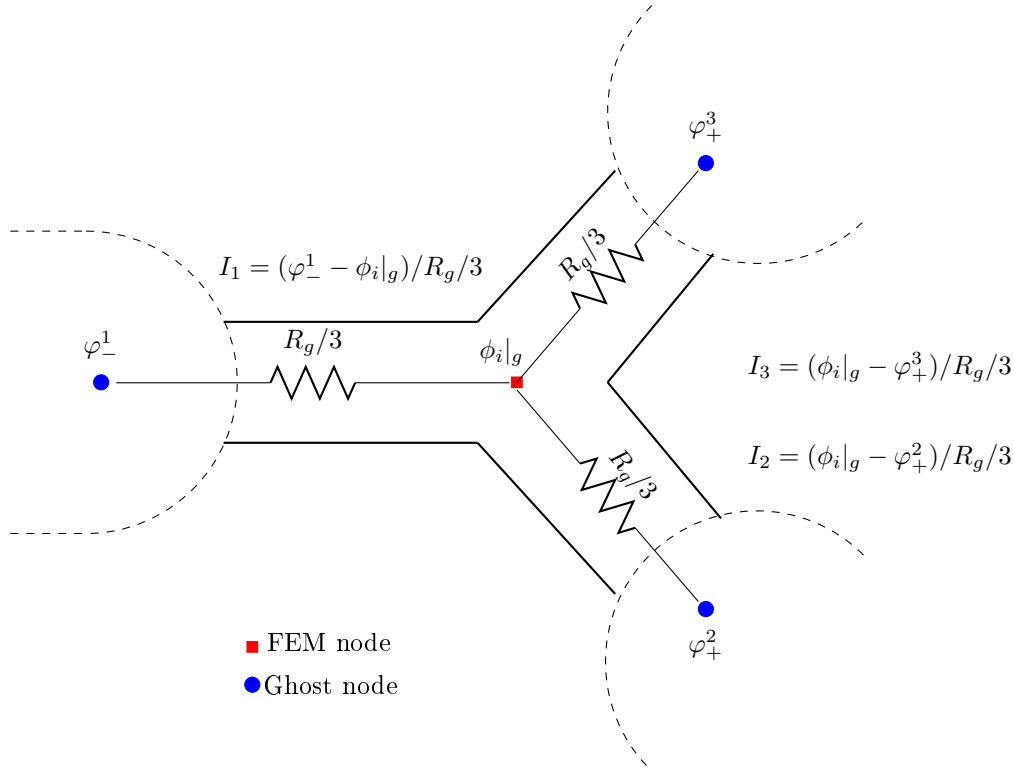


Figure 4.2: Detail of the branching node point in the finite element (FE) node points and ghost nodes. The currents $I_{1,2,3}$ are defined from the ghost node the FE nodes.

The values $\phi_{i|g}, I_g$ at the branching point are repeated in order to allow each segment to be solved separately. The three endpoints of the segments are then assumed to connect in the gap-junction of the three cells (see Fig. 4.2). In contrast to the method in Chapter 3, each of the points gets only one cell membrane model associated with it instead of two. The single cell membrane model will then be solved in the corresponding cell segment. The currents are given from each cell to the branching point as indicated in Figure 4.2. This adjustment is necessary because in the previous method there are six ghost nodes at each branching point, but only three actual cells. As it will be seen, the more concise formulation will also result in a more accurate numerical solution in comparison with analytical solutions.

Once the explicit gap-junction model is in place, the compatibility of the macroscopic conductivity tensor with the gap-junction resistance needs to be ensured. Therefore, it is assumed that σ_i is the intracellular conductivity without any effect of gap-junctions

and the equivalent conductivity is introduced under the assumption of a cylindrical volume conductor $\sigma_i^* = (\sigma_i \ell) / (\ell + \sigma_i R_g \pi \rho^2)$, where ℓ is the length of the Purkinje cell and ρ its radius. Note that this assumes that any discretisation has a step length $h = Z\ell$, which is an integer multiple Z of the cell length ℓ . In this notation (2.22) becomes

$$\partial_x \sigma_i^* \partial_x \varphi_{\pm} = \beta (C_m \partial_t \varphi_{\pm} + I_{\text{ion}}(\varphi_{\pm}, \xi_{\pm})). \quad (4.2)$$

To approximate the solution of (4.2) in time the operator splitting technique from Section 3.2.1 is used. The four steps are outlined in Figure 4.1.

4.2.2 Hardware Implementation

In the following Section, the different characteristics of the three implementations are detailed. They are all performed using the `LifeV` library¹, which provides methods to assemble the finite element stiffness and mass matrices and the right hand side coming from boundary conditions, time discretization and forcing terms. Furthermore, linear solvers and preconditioners are provided through the `Trilinos`² linear algebra library.

In all implementations, the linear system is solved with the generalised minimal residual method with incomplete LU factorisation for preconditioning of the linear system. The generalised minimal residual method was used as the system matrices are not symmetric due to the coupling condition enforcement at the junctions. In each iteration the preconditioner is applied to the linear system. This is done by solving first for the lower triangular system and then solving for the upper triangular system.

To advance the ionic cell models in time an explicit forward Euler method has been used. The more efficient Rush-Larsen method could not be used, due to problems with the numerical stability of the Stewart model. This is also reflected in the stiffness of the resulting ordinary differential equation system from the ionic models. As a result of the high stiffness, a timestep of 0.002 ms for the Euler method was needed. This timestep is a factor of ten smaller than the timestep for the linear system of the diffusion part. Therefore, in each global timestep the ionic model has been solved ten times.

The pure CPU implementation was parallelised with the help of the OpenMPI

¹The `LifeV` (<http://www.lifev.org>) finite element library is the joint collaboration between four institutions: EPFL, Politecnico di Milano, INRIA, and Emory University.

²<http://www.trilinos.org>

framework, which allows, in the proposed algorithm, to perform Steps 1 to 3 in a distributed way with linear partitioning. The linear system is solved (Step 4) with one OpenMPI process to eliminate communication between CPUs while solving the linear system. Furthermore, the computationally most expensive step in the algorithm is Step 2. This implies that all other processes need to send their data to the serial process and after solving the problem the solution needs to be redistributed (see Figure 4.3 for the workflow).

In the CPU/GPU hybrid implementation the membrane models are solved on the GPU. Therefore, before Step 2 the TMP is copied to the GPU, then the membrane model variables are updated, and the TMP is copied back from the GPU to the CPU. These three tasks are generated and queued in a CUDA stream, which allows for asynchronous GPU tasks. After the CPU has scheduled all task groups, it waits for their completion, and subsequently returns to Steps 3 and 4 on the CPU.

The third implementation does all the computation on the GPU, thus there is no memory copy between the steps. Steps 1 and 3 use the same code on the GPU as on the CPU, and in Step 2 the code from the hybrid implementation is reused, but without the memory copy. To solve the linear system in Step 4, the mass matrix and the stiffness matrix are built on the CPU with the `LifeV` framework, and the resulting sparse matrices are copied to the GPU. The same is done for the preconditioner, which is built on the CPU and then copied to the GPU. The generalised minimal residual method on the GPU is the same as on the CPU, but uses `cuSPARSE` and `cuBLAS` for the matrix operation. Solving for the upper and lower triangular matrix in the preconditioner is optimised with the CUDA framework, which provides a parallel implementation for the solution process [116].

There are two different hybrid and GPU implementations in the performance test, which correspond to using different levels of floating point precision. GPUs are designed for single precision and thus have much higher number of floating point operations in single precision than in double precision mode. Therefore, the same GPU code has been implemented using both double precision, and selectively dropping down to single precision where numerical stability was verified not to be affected. This is referred to as *mixed-mode*.

All computations were performed with a Dell Precision-WorkStation-T7500 featuring two Intel(R) Xeon(R) CPUs E5620 at 2.40GHz and a NVIDIA Quadro 4000 GPU

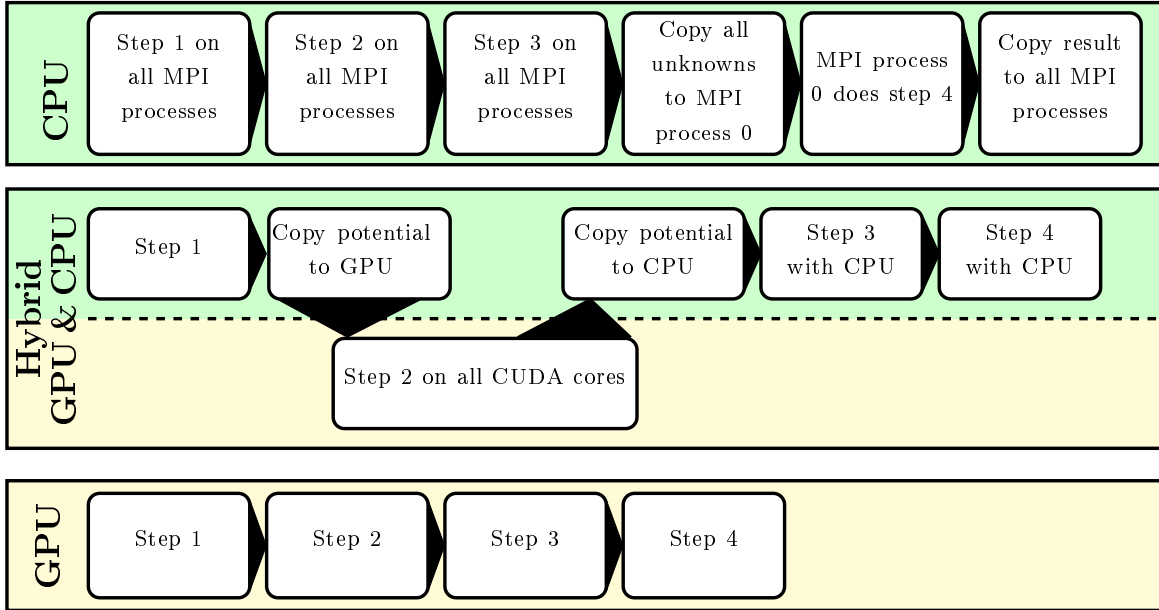


Figure 4.3: The workflow for the CPU (above), CPU/GPU hybrid (middle), and GPU (lower) implementation. The CPU needs to copy the transmembrane potential in the gap-junctions and the current, while the CPU/GPU hybrid needs to copy the potential of the ghost nodes. In the GPU implementation there is no copy required.

with 256 CUDA cores.

4.3 Verification of the Proposed Numerical Method

Two verification tests are performed. The first evaluates the accuracy of the solution in equilibrium against an analytical solution, and the second uses a travelling pulse solution to verify the dynamic solution.

4.3.1 Numerical Error and Convergence in Equilibrium

In the first experiment, an equilibrium solution for the monodomain equation (4.2) is sought. The approach is similar to Section 3.3.1, but with a finite line. Consider the simplified cell membrane model [117] given by

$$\partial_t \varphi = p\varphi, \quad (4.3)$$

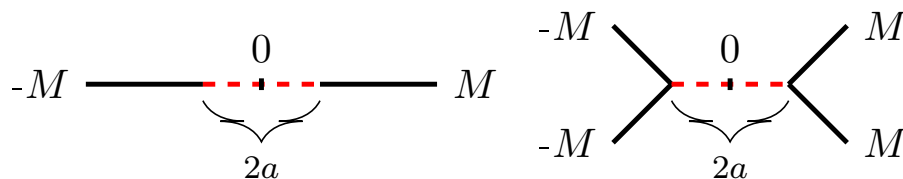


Figure 4.4: Problem domains for the equilibrium solutions, where the dashed area are unstable cells. Left for a line segment and right for symmetric bifurcation

where φ is the TMP and p is a model parameter. Depending on p the solution is stable ($p < 0$), or it is exponentially unstable if ($p > 0$). The cell membrane model is then applied to two different test geometries. The first geometry is a finite one-dimensional line segment (Fig. 4.4, left) $D_1 = [-M, M]$, $M > 1$, which is divided in three parts $D_{1,1} = [-M, -1]$, $D_{1,2} = [-1, 1]$, and $D_{1,3} = [1, M]$. The cell membrane model is chosen to be unstable in $D_{1,2}$, and stable elsewhere.

$$p(x) = \begin{cases} p_1 & \text{for } x \in D_{1,2} \\ -p_2 & \text{elsewhere} \end{cases},$$

where $p_i > 0$. The simplified cell membrane model is then introduced in the monodomain equation (4.2). Letting $\delta = \sigma_i/\beta$ and, assuming that the conductivity σ_i has no spatial dependency, the problem to be solved becomes

$$\begin{aligned} C_m \partial_t \varphi &= \delta \partial_x^2 \varphi - p(x) \varphi, \\ \varphi_1(-1) &= \varphi_2(-1) \quad , \quad \varphi_2(1) = \varphi_3(1), \\ \varphi_1'(-1) &= \varphi_2'(-1) \quad , \quad \varphi_2'(1) = \varphi_3'(1), \\ \varphi_1(-M) &= 0 \quad \quad \quad , \quad \varphi_3(M) = 0. \end{aligned} \tag{4.4}$$

The solution can be deduced with the canonical *ansatz* $V_i(x) = c_1 \exp(kx) + c_2 \exp(-kx)$, as shown by Artebrant *et al.* [112]. For a line segment the solution is:

$$V(x) = \begin{cases} \sinh(\kappa(M+x)) & , \quad x \in D_{1,1} \\ d \cos(kx) & , \quad x \in D_{1,2} \\ \sinh(\kappa(M-x)) & , \quad x \in D_{1,3} \end{cases}, \tag{4.5}$$

where $d = \sinh(\kappa(M-1))/\cos(k)$ and parameters $\kappa = \sqrt{p_1/\delta}$ and $k = \sqrt{p_2/\delta}$. To satisfy the differentiability conditions $\varphi_1'(x)|_{x=-1} = \varphi_2'(x)|_{x=-1}$, $\varphi_2'(x)|_{x=1} = \varphi_3'(x)|_{x=1}$,

in (4.4) the relation

$$k \tan(k) = \frac{\kappa}{\tanh(\kappa(M-1))}$$

must hold.

The second problem is formulated in the symmetric domain D_2 with a branching and joining point (Fig. 4.4, right). The domain consists of five line segments, the first two, $D_{2,1} = [-M, -1]$ and $D_{2,2} = [-1, 1]$, join the segment $D_{2,3} = [-1, 1]$, which branches into two further segments $D_{2,4} = [1, M]$ and $D_{2,5} = [1, M]$. As in the first domain, the middle segment $D_{2,3}$ has unstable cells while the outer branches $D_{2,1}, D_{2,2}, D_{2,4}$, and $D_{2,5}$ are stable. The problem is symmetric with respect to zero, thus it is sufficient to look at the negative domain only. Furthermore, $D_{2,1}$ and $D_{2,2}$ are equal, thus it is sufficient to find the solution on one of them. This means the following problem needs to be solved

$$\begin{aligned} \delta\varphi_1'' - p_1\varphi_1 &= 0 \quad \forall x \in D_{2,1} \\ \delta\varphi_3'' + p_2\varphi_3 &= 0 \quad \forall x \in D_{2,3} \end{aligned} \quad ,$$

$$\varphi_1(-1) = \varphi_3(-1), \quad 2\varphi_1'(x)|_{x=-1} = \varphi_3'(x)|_{x=-1}, \quad \varphi_1(-M) = 0$$

where the first two equations are due to Kirchoff's current law.

Following an exponential *ansatz*, the solution can be constrained to be unique by choosing the maximum amplitude $\varphi(0) = 1$, which leads to

$$\begin{aligned} \varphi_{1,2} &= c_1 \sinh(\kappa(M+x)), \\ \varphi_3 &= \cos(kx), \\ \varphi_{4,5} &= c_1 \sinh(\kappa(M-x)), \end{aligned} \quad (4.6)$$

where $c_1 = \cos(-k)/\sinh(\lambda_1(M-1))$ and the relation between κ and k changes to

$$k \tan(k) = \frac{2\kappa}{\tanh(\kappa(M-1))}.$$

Numerical solution in equilibrium

For the numerical solution $\delta = 1$ is chosen, which imposes the condition $1 = \sigma^*/\beta$. With a physiological cell length of $\ell = 62.5 \mu\text{m}$, a diameter of $16.0 \mu\text{m}$, and a gap-junction resistance chosen to $R = 0.1 \text{ k}\Omega$, the intracellular conductivity becomes $1967.5 \text{ kS cm}^{-1}$.

Furthermore, the spatial step size h is chosen as an integer multiple of the cell length ℓ .

On the line D_1 the parameter values $p_2 = 0.0946441$, $M = 20$ are chosen, and the capacitance of the cell membrane is assumed $C_m = 1 \mu\text{F}$. For the branching domain D_2 the parameters are set to $M = 10$, $p_2 = 1$, with $\delta = 1$.

The resulting error distribution over the line and the branching domain is shown in Figure 4.5, where the largest contribution of the error comes from the passive cell region. The convergence test shows that with decreasing spatial step size the L_2 -error reduces faster than linearly for the single-interval domain D_1 (Fig. 4.5) and linearly for the example in the branching domain D_2 . Note that without the modification introduced in Section. 4.2.1 only sub-linear convergence behaviour was obtained for the branching domain case (compare with Fig. 3.3), indicating that the modification is required for the accuracy of the numerical method.

4.3.2 Analytical Solution for a Travelling Pulse

In this section, the convergence of the dynamic solution is investigated. Therefore, an analytic solution for a travelling wave of the linearised FitzHugh-Nagumo equation [118, 119] is constructed and then solved numerically.

For the construction of the solution to the FitzHugh-Nagumo model the work of Rinzel and Keller [118] is followed. To solve the monodomain equation, they used the two variable ionic model, with the TMP φ and the recovery variable w

$$\begin{aligned} \partial_t \varphi = I_{ion} &= f(\varphi) + w \\ \partial_t w &= bV \\ f &= V(a - \varphi)(1 - \varphi) \end{aligned}, \quad (4.7)$$

where f can be piece-wise linearised to $f = \varphi - H(\varphi - a)$, with $0 \leq a \leq 1/2$ and H is the Heaviside function. The solution of the linearised problem (4.7) on an infinite line is well-known [78, 118].

Next consider the monodomain equation (4.2) over an infinite line under the assumption that σ_i^* does not depend on x and couple it to the linearised FitzHugh-Nagumo

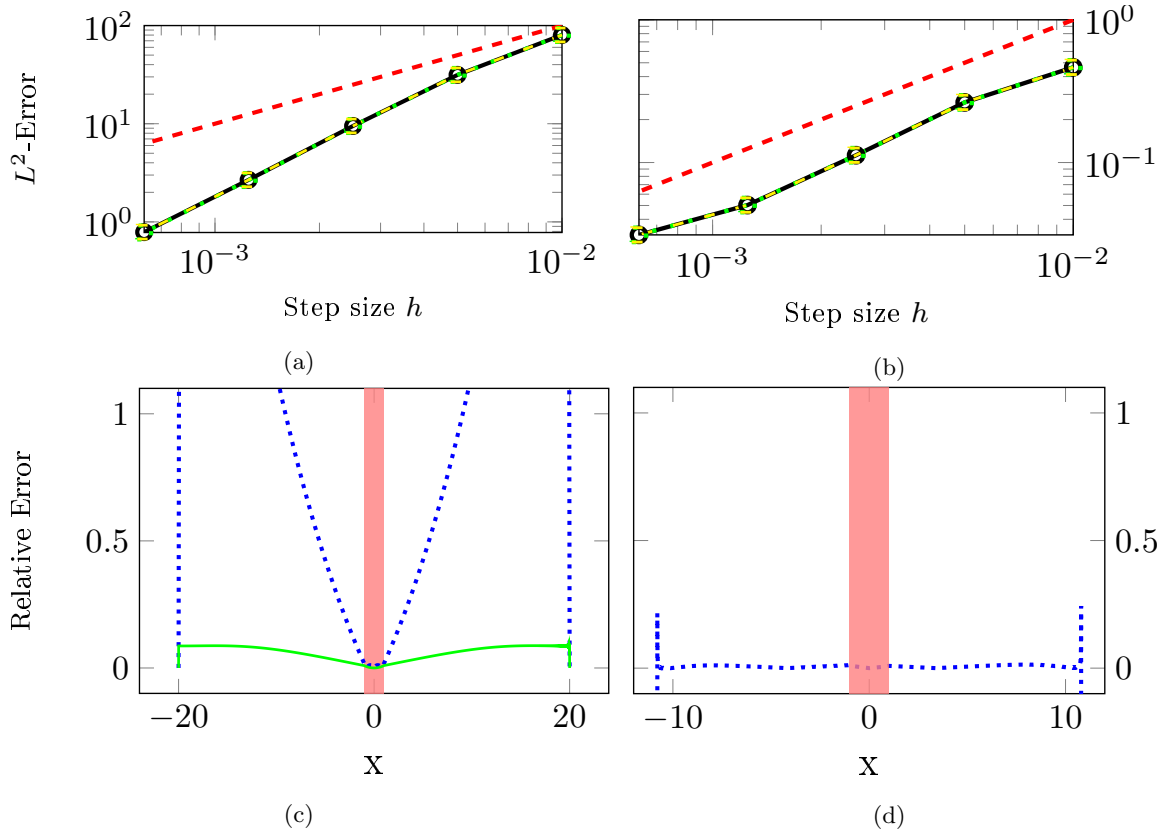


Figure 4.5: Error obtained with different numerical implementations. Upper row: L_2 error as a function of spatial step size h for different implementations; black solid line for CPU, yellow dashed line for hybrid, green dotted line for GPU, and red dashed line the comparison with linear convergence rate. (a) solution over one line segment D_1 , (b) over the branching configuration D_2 . Lower row: relative error obtained for the pure-GPU implementation. (c) solution over one line segment D_1 , (d) over the branching configuration D_2 . Blue dotted line corresponds to error for a step size of 0.1 mm, the green solid line the error (enlarged by a factor 10) for step size of 0.00625 mm. The red zone corresponds to the domain of active cells.

cell membrane model

$$\begin{aligned}
 C_m \partial_t \varphi &= \frac{\sigma_i^*}{\beta} \partial_x^2 \varphi - f(\varphi) - w \\
 \partial_t w &= b\varphi \quad , b \geq 0 . \\
 f(\varphi) &= \varphi - H(\varphi - a) \quad , 0 \leq a \leq 1/2
 \end{aligned} \tag{4.8}$$

To be equivalent to the approach in [118], it is assumed that $\sigma_i^*/\beta = 1$ and $C_m = 1$.

By differentiating the first equation in (4.8) with respect to time, the system can be rewritten in one equation

$$\begin{aligned}
 \partial_t^2 \varphi &= \partial_t \partial_x^2 \varphi - \partial_t f(\varphi) - \partial_t w, \\
 \Rightarrow \partial_t^2 \varphi &= \partial_t \partial_x^2 \varphi - \partial_t f(\varphi) - b\varphi.
 \end{aligned} \tag{4.9}$$

To solve this problem the travelling wave *ansatz* $\varphi(x, t) = \varphi_c(z)$ where $z = x + ct$ with $c > 0$ is introduced. Furthermore, it is assumed that $\varphi_c(0) = a$ and $\lim_{|z| \rightarrow \infty} \varphi_c(z) \rightarrow 0$, and from the intermediate value theorem follows the existence of a $z_1 \neq 0$ with $\varphi_c(z_1) = a$. The system to be solved can be rewritten as

$$\begin{aligned}
 c^2 \varphi_c'' &= c \varphi_c''' - c f'(\varphi_c) \varphi_c' - b\varphi \\
 0 &= \varphi_c''' - c \varphi_c'' - f'(\varphi_c) \varphi_c' - (b/c) \varphi \\
 0 &= \begin{cases} \varphi_c''' - c \varphi_c'' - \varphi_c' - (b/c) \varphi & \forall z \in \mathbb{R} \setminus \{0, z_1\} \\ \varphi_c''' - c \varphi_c'' - (b/c) \varphi & z \in \{0, z_1\} \end{cases} ,
 \end{aligned} \tag{4.10}$$

with boundary condition $\lim_{|z| \rightarrow \infty} \varphi_c(z) \rightarrow 0$ and where $'$ indicates a derivative with respect to z . The solution can be obtained in the three regions $z < 0$, $0 \leq z \leq z_1$ and $z > z_1$. Following an exponential ansatz for the differential equation the roots of the cubic polynomial need to be found

$$p(\lambda) = \lambda^3 - \lambda^2 - \lambda - (b/c). \tag{4.11}$$

If the discriminant is non-negative there are three distinct real solutions, while for a negative discriminant two of the solutions are complex. Let λ_1 be the positive real solution while λ_2 and λ_3 are the possible complex solutions. Then, the solution to the

differential equation (4.10) is [78]

$$\varphi_c = \begin{cases} a \exp(\lambda_1 x) & z < 0 \\ (a - p'(\lambda_1))^{-1} \exp(\lambda_1 x) - p'(\lambda_2)^{-1} \exp(\lambda_2 x) - p'(\lambda_3)^{-1} \exp(\lambda_3 x) & 0 \leq z \leq z_1 \\ p'(\lambda_2)^{-1} (\exp(-\lambda_2 z_1) - 1) \exp(\lambda_2 x) + p'(\lambda_3)^{-1} (\exp(-\lambda_3 z_1) - 1) \exp(\lambda_3 x) & z > z_1. \end{cases} \quad (4.12)$$

In the following, it is shown that φ_c is real, even with complex eigenvalues λ_2, λ_3 . Here the fact that $\text{Re}(\lambda_2) = \text{Re}(\lambda_3)$ and $\text{Im}(\lambda_2) = -\text{Im}(\lambda_3)$, where $i = \sqrt{-1}$ is used.

$$\Rightarrow \varphi_c = \begin{cases} a \exp(\lambda_1 x) & z < 0 \\ \frac{\exp(\lambda_1 x)}{(a - p'(\lambda_1))} - \left(\frac{e^{i\text{Im}(\lambda_2)x}}{p'(\text{Re}(\lambda_2) + i\text{Im}(\lambda_2))} + \frac{e^{-i\text{Im}(\lambda_2)x}}{p'(\text{Re}(\lambda_2) - i\text{Im}(\lambda_2))} \right) e^{(\text{Re}(\lambda_2)x)} & 0 \leq z \leq z_1 \\ \frac{e^{\lambda_2(x-z_1)} - e^{\lambda_2 x}}{p'(\lambda_2)} + \frac{e^{\lambda_3(x-z_1)} - e^{\lambda_3 x}}{p'(\lambda_3)} & z > z_1 \end{cases} , \quad (4.13)$$

$$\Rightarrow \varphi_c = \begin{cases} a \exp(\lambda_1 x) & z < 0 \\ \frac{\exp(\lambda_1 x)}{(a - p'(\lambda_1))} - \left(\frac{\alpha - i\beta}{\alpha^2 + \beta^2} e^{i\text{Im}(\lambda_2)x} + \frac{\alpha + i\beta}{\alpha^2 + \beta^2} e^{-i\text{Im}(\lambda_2)x} \right) e^{(\text{Re}(\lambda_2)x)} & 0 \leq z \leq z_1 \\ \frac{e^{\lambda_2(x-z_1)}}{p'(\lambda_2)} + \frac{e^{\lambda_3(x-z_1)}}{p'(\lambda_3)} - \left(\frac{e^{(\lambda_2)x}}{p'(\lambda_2)} + \frac{e^{\lambda_3 x}}{p'(\lambda_3)} \right) & z > z_1 \end{cases} , \quad (4.14)$$

$$\alpha = 3(\text{Re}(\lambda_2)^2 - (\text{Im}(\lambda_2))^2) - 2\text{Re}(\lambda_2) - 1,$$

$$\beta = 6(\text{Re}(\lambda_2))(\text{Im}(\lambda_2)) - 2(\text{Im}(\lambda_2)).$$

Note that $\alpha, \beta \in \mathbb{R}$. Then applying Euler's formula

$$(a + bi)e^{-ci} + (a - bi)e^{ci} = 2(a \cos(c) + b \sin(c)) \quad a, b, c \in \mathbb{R}. \quad (4.15)$$

to write the formula in the region $0 \leq z \leq z_1$ as real expression

$$\Rightarrow \varphi_c = \begin{cases} a \exp(\lambda_1 x) & z < 0 \\ \frac{\exp(\lambda_1 x)}{(a-p'(\lambda_1))} - 2\left(\frac{\alpha}{\alpha^2+\beta^2} \cos(\text{Im}(\lambda_2)x) + \frac{\beta}{\alpha^2+\beta^2} \sin(\text{Im}(\lambda_2)x)\right)e^{(\text{Re}(\lambda_2)x)} & 0 \leq z \leq z_1 \\ \frac{e^{\lambda_2(x-z_1)}}{p'(\lambda_2)} + \frac{e^{\lambda_3(x-z_1)}}{p'(\lambda_3)} - \left(\frac{e^{(\lambda_2)x}}{p'(\lambda_2)} + \frac{e^{\lambda_3 x}}{p'(\lambda_3)}\right) & z > z_1 \end{cases}, \quad (4.16)$$

$$\alpha = 3(\text{Re}(\lambda_2))^2 - (\text{Im}(\lambda_2))^2 - 2\text{Re}(\lambda_2) - 1,$$

$$\beta = 6(\text{Re}(\lambda_2))(\text{Im}(\lambda_2)) - 2(\text{Im}(\lambda_2)).$$

For the term in $z > z_1$ the steps used in the region $0 \leq z \leq z_1$ are applied twice, which results in the real expression

$$\varphi_c = \begin{cases} a \exp(\lambda_1 x) & z < 0 \\ \frac{\exp(\lambda_1 x)}{(a-p'(\lambda_1))} - 2\left(\frac{\alpha}{\alpha^2+\beta^2} \cos(\text{Im}(\lambda_2)x) + \frac{\beta}{\alpha^2+\beta^2} \sin(\text{Im}(\lambda_2)x)\right)e^{(\text{Re}(\lambda_2)x)} & 0 \leq z \leq z_1 \\ 2\left(\frac{\alpha}{\alpha^2+\beta^2} \cos(\text{Im}(\lambda_2)(x-z_1)) + \frac{\beta}{\alpha^2+\beta^2} \sin(\text{Im}(\lambda_2)(x-z_1))\right)e^{(\text{Re}(\lambda_2)(x-z_1))} - & z > z_1 \\ -2\left(\frac{\alpha}{\alpha^2+\beta^2} \cos(\text{Im}(\lambda_2)x) + \frac{\beta}{\alpha^2+\beta^2} \sin(\text{Im}(\lambda_2)x)\right)e^{(\text{Re}(\lambda_2)x)} & \end{cases} \quad (4.17)$$

Rintzel and Keller showed that (4.12) is a solution only if the parameter a satisfies the relation with the parameters b and c , which is outlined in the following. The relation assumes the eigenvalues λ_i $i = 1, 2, 3$ are known for given b, c , which then define the function

$$f(s) := 2 - s + \frac{p'(\lambda_1)}{p'(\lambda_2)} s^{(-\lambda_2/\lambda_1)} + \frac{p'(\lambda_1)}{p'(\lambda_3)} s^{(-\lambda_3/\lambda_1)}.$$

The root s_0 of the function f defines

$$a = \frac{1 - s_0}{p'(\lambda_1)}. \quad (4.18)$$

This relation can be satisfied for any b with at most two c_i , where $c_1 \leq c_2$. The slow pulse c_1 is an unstable solution, while c_2 is a stable solution [78, 118]. To obtain the value of z_1 for the given set of parameter a, b, c the following equation needs to be

solved

$$\exp(-\lambda_1 z_1 s_0) = 1 - ap'(\lambda_1). \quad (4.19)$$

Numerical Simulation of the Travelling Wave

For the verification of the dynamic solution the following values are used $a = 0.225$ mV, $c = 1.2$ cm ms⁻¹, $b = 0.2$ and $z_1 = 6.633$ cm. In the numerical problem, the parameter values $\sigma_i = 1967.5$ kS cm⁻¹, $\beta = 1$, $R = 0.1$ k Ω and $C_m = 1$ μ F are used. The solution (4.12) is used to initialise the numerical solution at the time 0 ms on a line of length 160 cm, and origin at 85 cm. With these values the wave exits the domain after 50 ms. The final time is chosen such that the wave in the numerical simulation stabilises in shape and then propagates for about 20 ms. All simulations use a temporal time step of 0.001 ms.

The first experiment is performed for spatial resolution of 0.006 25 mm, where the L^2 -error is calculated at each time step and plotted against the time for all three solvers (Fig. 4.6, top, left). For the first time steps the error increases slower compared to the error increase after about 20 ms. Thereafter, a linear increase of the error is observed. This can be explained with the plot of the L^2 -norm of the solution (Fig. 4.6, top, right), which is changing until 20 ms and thereafter can be considered as constant. The changes are due to the fact that the maximal amplitude of the wave is changing. The stable, slightly larger pulse, has after 20 ms a higher conduction velocity of about $c = 1.201\ 32$ m s⁻¹, which is responsible for the linearly increasing error over time.

The verification is concluded with a convergence test in the L_2 error and the conduction velocity for the dynamic simulation. Therefore, the L_2 error and the conduction velocity after 40 mm are evaluated for different step discretisations $h = \{1$ mm, 0.51 mm, 0.25 mm, 0.125 mm, 0.0625 mm $\}$. The L_2 error converges superlinearly (Fig. 4.6, bottom, left). More importantly, the conduction velocity approaches the theoretical value of 1.2 m s⁻¹ at a step size of 0.0625 mm (Fig. 4.6, bottom, right). Again, the improved method of Section 4.2.1 converges to the exact conduction velocity.

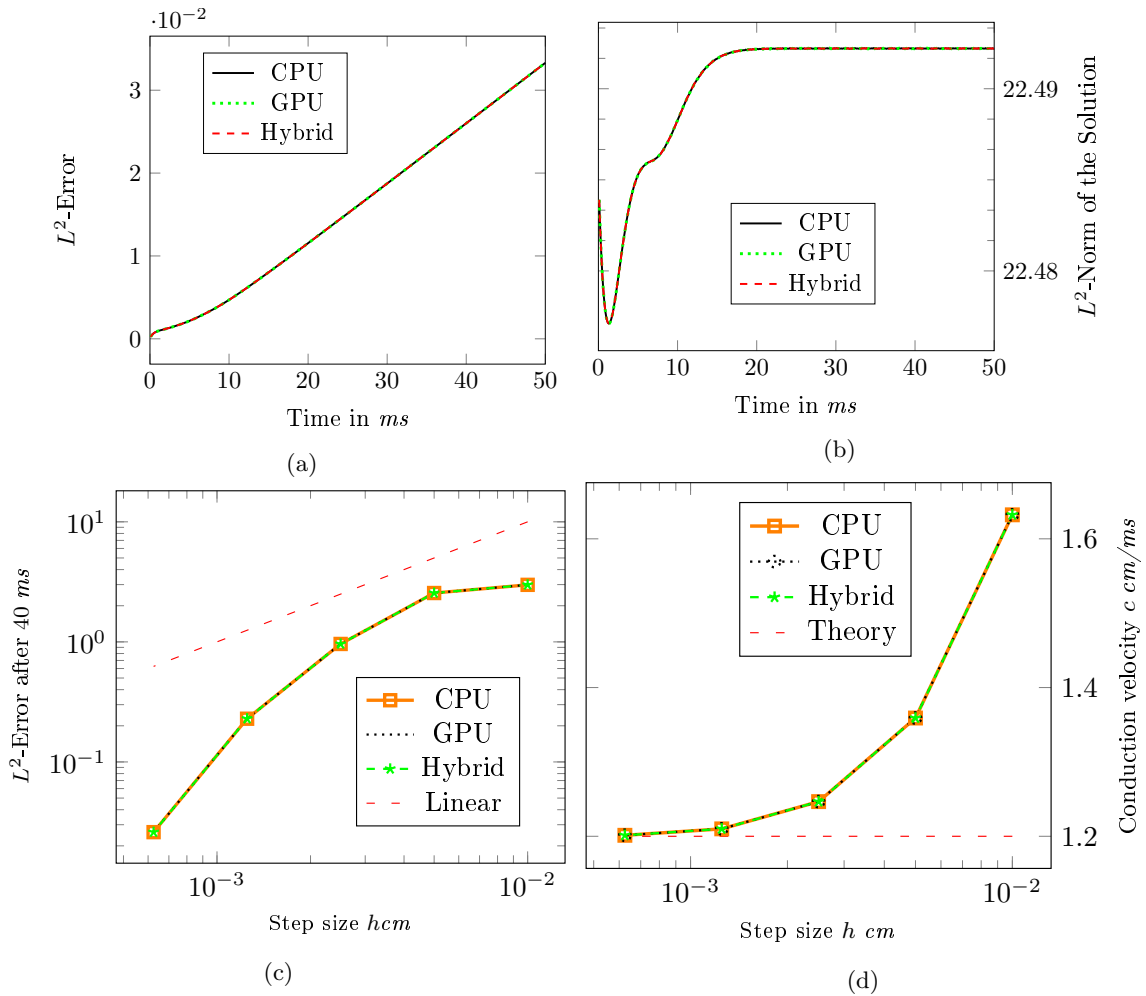


Figure 4.6: Simulation results with the traveling wave. (a) the L^2 error and (b) L^2 -Norm of the solution. The solution was obtained with the CPU (solid), hybrid (dashed) and the GPU (dotted), data shown for a spatial step size of 0.00625 mm. (c) the L^2 error and (d) the conduction velocity after 40 ms against the step discretisation, obtained with the CPU (solid), hybrid (dashed) and the GPU (dotted)

4.4 Computational Efficiency

Next, the computational performance of the different solver implementations is evaluated on problems of varying size and complexity. The number of degrees of freedom is therefore varied either by increasing the complexity of the PN (spatial complexity), or by switching to a more complex cell membrane model (model complexity).

The four PNs of varying levels of detail from Section 3.3.2 are considered. In order of increasing complexity, the first PN consists of the main Purkinje branches only, the second one has another level of branching giving a physiological covering of the LV, and the third network has another level of Purkinje branches added to increase the density of the Purkinje-muscle junction (PMJ), resulting in a physiological PN for the left ventricle (LV). The fourth case is a dense PN for both the LV and right ventricle (RV). All PNs are discretised with a spatial resolution of 0.1 mm and are generated without loops for compatibility with other solvers (see Fig. 4.7).

Two different cell membrane models were used to test the influence of model complexity. The first and simpler Di Francesco-Noble model [3], which has been used in previous works [103], has 15 state variables. The model has been obtained from the CellML database and used without modification to the initial states or constants. The second membrane model used here has been published by Stewart *et al.* [86], and is based on modifications to the ten Tusscher-Panfilov model, and has 20 state variables. The model was obtained from the CellML repository, although the initial conditions were set to the values stated in Appendix Table 8.1. The change in initial conditions was made to avoid the early self-excitation that is present in Purkinje cells but should not manifest itself under physiological conditions. For both membrane models a cell length of 0.01 mm, cell radius of 0.005 mm, and an intracellular conductivity of $40 \text{ S}^{-1} \text{ cm}^{-1}$ were assumed, where the last two values were chosen to obtain realistic conduction velocities in the range between 3 m s^{-1} and 4 m s^{-1} . The gap junction resistance was chosen as $500 \text{ k}\Omega$. For the simulation, a temporal step size of 0.01 ms has been used and the simulation was run for 50 ms, after which all networks were fully depolarised.

In the pure CPU implementation eight processes are run in parallel, while the hybrid and GPU implementations are run using one CPU process. The simulations were run in two different configurations on the GPU, the first in double precision, while the

second was in single precision. For all simulations, the time spent on setting up the problem is measured, which includes reading the mesh and assembling the matrices and preconditioners. Further, the time needed for solving the membrane models and the diffusion equation is reported in Figure 4.7.

As expected the hybrid and pure GPU implementations are faster than the pure CPU implementation (Fig. 4.7), and a further speed-up is observed moving from double precision to single precision in the pure GPU implementation. The reason for the speed-up with the single precision in the pure GPU implementation is that the particular GPU used has roughly twice the number of floating point operations per second in single precision than it has in double precision. The reduction of computational time by the usage of single precision in hybrid implementation was limited. One possible reason for this might be that the particular GPU used is able to handle the entire double precision problem without full occupation. The second reason might be that the TMP needs to be converted from double precision to single precision, which is done in serial on the CPU.

The amount of time needed to solve the reaction part of the problem varies considerably between the pure CPU, hybrid, and pure GPU implementations. The pure CPU implementation is always the slowest, but the hybrid implementation performs more favourably on less complex membrane models, while the pure GPU implementation performs better with more complex membrane models. This is much more evident in the single precision versions. A possible reason for this can be found in the workflow of the hybrid and pure GPU implementations (Fig. 4.3), where a memory copy from the GPU to the CPU takes place in each time step of the hybrid implementation. In the pure GPU implementation this is unnecessary because values are used on the GPU only. This explains why the GPU implementation performs better with increasing complexity of the membrane model.

Solving the diffusion step with the pure GPU implementation is nearly always the slowest. We note that the hybrid implementation is faster than the pure CPU, as in the CPU implementation the TMP and the current need to be sent from all the OpenMPI nodes to the master node and the results communicated back. The linear system itself is solved in the same way in the pure CPU and the GPU/CPU hybrid cases. In the pure GPU implementation the same algorithm is used, but the matrix operations are performed on the GPU. For small Purkinje systems, meaning very sparse

and small matrices, the performance of the pure GPU implementation is behind the pure CPU and hybrid implementations. With increasing spatial complexity the pure GPU performance becomes better compared to the pure CPU performance, which likely is related to the size of the problem. Due to the overhead introduced by each CUDA operation, for very small problem sizes the benefits of GPU parallelism are lost.

After comparing the various implementations of this chapter, results are compared with previously published studies (Tab. 4.1). The speed-up for the reaction part is the focus here, because no comparable speed-up was studied for solutions on 1-D networks. Most studies compare the speed-up of a single GPU against a single CPU core. Therefore, the previous simulation of the bi-ventricular PN has been run on one core with the di Francesco-Noble model. It took 13 497 s to solve the reaction part. This means that the pure-GPU formulation was 123 times faster in mixed precision mode and in double precision mode it was 30 times faster. This is compared against four different studies, which use an explicit time-stepping method and report their speed-ups. The first study is conducted by Mena and Rodrigues [120] and investigates the speed-up for different number of nodes in the mesh. Their results are based on the ionic model by Ten Tusscher and Panfilov [1], which is integrated with the Rush-Larsen method. The best speed-up achieved was 120, where a single CPU core is compared against one NVIDIA Tesla M2090 GPU with 512 CUDA cores. This is the highest speed-up reported in the comparison, and the single precision implementation performs slightly better. The double precision mode is outperformed by the study of Mena and Rodrigues, as well as by the study of Rocha *et al.* [121]. In their study the Luo and Rudy [2] model was solved by an Euler forward method. The usage of a GPU with 480 CUDA cores resulted in a speed-up of 51 over one CPU. The remaining two studies reported smaller speed-ups than the double precision implementation achieved. Vigmond *et al.* [122] compared the speed-up for the cell model by Mahajan *et al.* [123]. For integration the Rush-Larsen method was employed where possible and otherwise the Euler forward or Runge-Kutta methods. This allowed them to reduce the computational time by a factor of about 11, when using a single GPU with 240 CUDA cores. In the work of Neic *et al.* [124] a larger whole ventricular simulation with the Mahajan ionic model is performed. Therefore, they employed a minimum of six GPUs with 448 CUDA cores each, and compared it against an implementation with six CPUs. The reported timings for the time spent solving the ordinary differential equation system shows a reduction

Study	#CUDA cores	Speed-up	Degrees of freedom	Ionic model	Temporal step size [ms]
Mena [120]	512	120	1 900 000	TP06	0.020
Rocha [121]	240	51	824 328	LR	0.010
Vigmond [122]	240	11	27 000 600	Mahajan	0.025
Neic [124]*	448	12	116 100 000	Mahajan	0.025
Hybrid	256	123	1 387 410	DFN	0.002
Full GPU	256	30	1 387 410	DFN	0.002

Table 4.1: Comparison of the speed-up in solving the ionic model with previous studies. The speed-up are based on one CPU core, against one GPU. * obtained using 6 CPUs and 6 GPUs. (TP06) model by Ten Tusscher and Panfilov [1], (LR) Model by Luo and Rudy [2], (DFN) model by di Francesco and Noble [3].

by a factor of 12. Overall, the presented single precision implementation has the best speed-up of all studies, but also the double precision implementation shows an average improvement for the speed-up.

4.5 Conclusion

An improved parallel algorithm has been presented for solving the monodomain cardiac electrophysiology equations on one-dimensional branching PN that is suitable for simulating activation on realistic PNs in human-size hearts. Then a verification scheme of the numerical solution was developed, which was applied to three different implementations: pure-CPU, pure-GPU, and hybrid. Finally, the performance of the implementations was compared.

The verification of the first implementation in Chapter 3 of the original proposed algorithm by Vigmond and Clemens [103] showed sublinear convergence in the L_2 -error for branching fibres. To improve the convergence, in this Chapter, a new explicit gap-junction formulation has been described, which is also more consistent in terms of the connection between multiple Purkinje fibre endpoints. Furthermore, a modification to the effective conductivity tensor was needed to ensure mathematical compatibility with the new formulation. Both improvements together led to a linear convergence as was demonstrated in the verification study. The results also showed convergence of the conduction velocity in the numeric solution towards its theoretical value. Im-

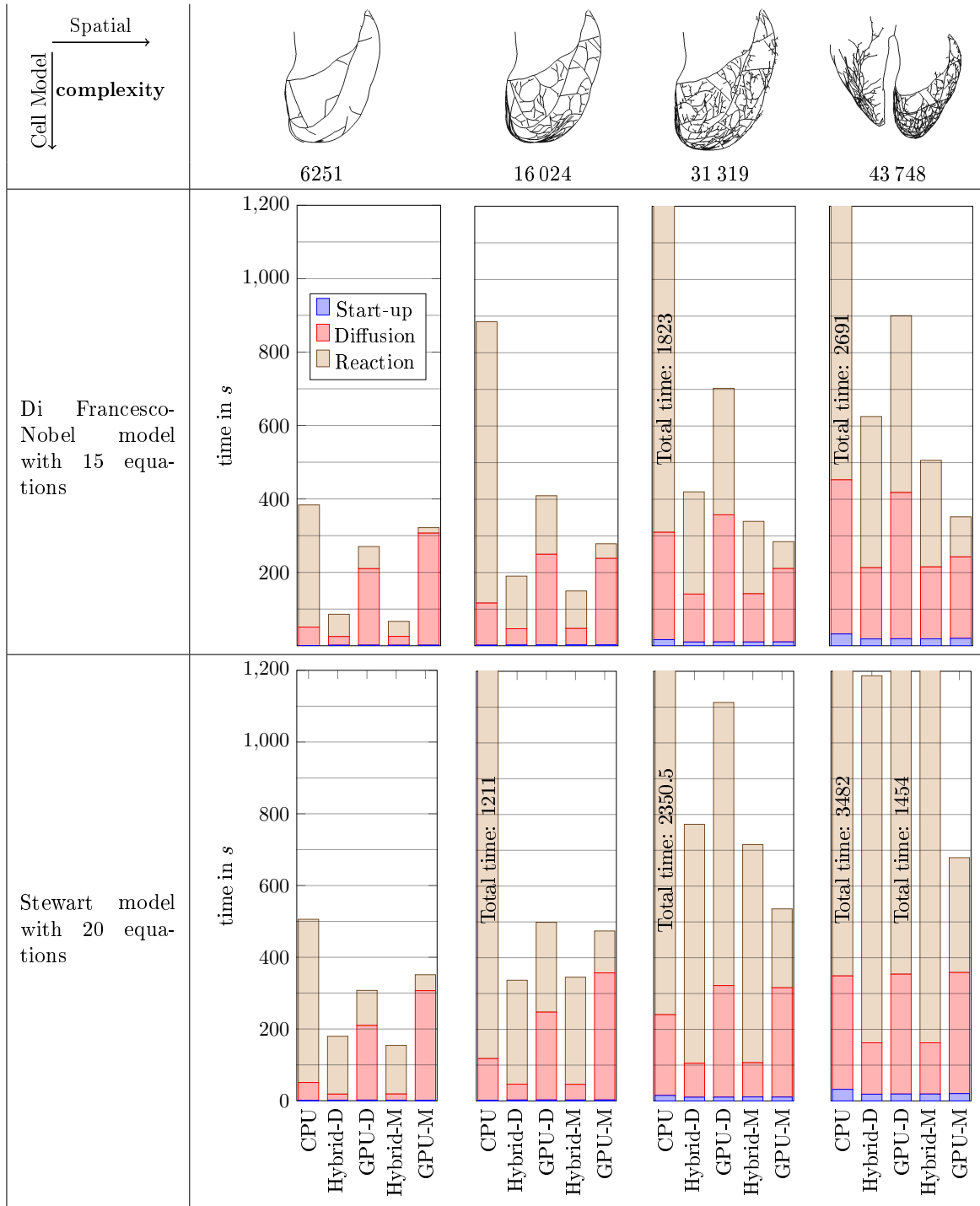


Figure 4.7: Performance test for two different cell models and four Purkinje networks.

portantly, there were no notable differences in convergence rates between the three different implementations.

After establishing that all three implementations achieved the same accuracy, the selection of an implementation is based on the relative computational performances of each implementation. The first observation was that GPU based methods outperformed the implementation of eight parallel CPUs. The largest benefit on the parallel pure-GPU implementation was obtained either when a fully detailed biventricular (spatially complex) network was used, or when sufficiently complex membrane models were used, such as the model proposed by Stewart *et al.* 2009 considered in this study. For simpler LV-only models, or when using simpler membrane models, such as the Di Francesco-Noble model considered in this study, the hybrid implementation may be more attractive. In either case, the benefits of GPU-accelerated computation of AP in the fast conduction system have been demonstrated.

The implementation proposed in this study, results in a substantial reduction of computational time over conventional multi-processor implementations. Moreover, it relies on GPU hardware which is widely available. Thus, there is no need to use less available or expensive high performance computing facilities. The speed-up gained by the GPU implementation enables running more simulations in less time. Therefore, it is more feasible to perform virtual population studies, where large numbers of experiments are required.

The PN model can be combined with different models of the myocardium to conduct simulations of the ventricular activation. Currently, the eikonal model of activation time is the only model feasible for virtual population studies in terms of computational time. However, the model of the PN can also be coupled with monodomain or bidomain approaches for the myocardium [111].

Chapter 5

Manual Creation of a Virtual Population to Explore the Benefits of False Tendon in Subjects with Left Bundle Branch Block

After investigating models of the electrophysiology in the Purkinje network (PN) in the last chapters, the focus is moved to study the morphology of the PN. In this chapter, a virtual population study of the ventricular activation time of the human heart in the presence of false tendons (FTs) is presented. Therefore, a computational model of the human heart that includes a FT, PN, and papillary muscle (PM) is built. Based on this models, simulations are performed to investigate the effect of different types of FTs on hearts with the electrical conduction abnormality of a left bundle branch (LBB) block. A virtual population of 70 human hearts is manually constructed from a statistical shape model, and a total of 560 simulations are run to assess ventricular activation time with different FT configurations.

This chapter is adopted from journal the publication [125].

5.1 Motivation

FTs are additional fibrous or fibromuscular strings occasionally located inside the ventricles, which are attached to either the ventricular wall, the septum, or the PM [17]. Autopsy investigations have shown a high prevalence of these anomalies, ranging from 34% to 68% of the population (Table 5.1) in healthy humans. A wider prevalence range is reported in echocardiographic studies, from less than 1% to more than 85% (Table 5.1), which shows the difficulty in imaging FTs *in vivo*, which in turn makes it difficult to study their significance and possible effects on the cardiac function.

As described in Chapter 1, autopsy studies show that FTs comprise different tissue types including connective, conductive, and fibrous tissues, as well as blood vessels [17, 19, 20, 26, 126], which suggests that their presence is likely to intervene in the cardiac electrical conduction and more generally in the function of the heart. This is further supported by reports of isolated premature ventricular contractions [26, 27, 127], electrical activation re-entry [19], tachycardia [23, 24], and electrocardiogram (ECG) changes [28, 29, 128, 129] in subject with FTs. So far, due to the complexity of the FTs and the challenges associated with their *in vivo* imaging, their exact significance, effects and possible risks to the human heart remain largely unclear [19, 25, 130].

On the other hand, despite their relatively high prevalence and the increasing clinical interest associated with FTs, to the best of knowledge of the author of this thesis there exists in the literature no computational model assessing the activation times of the

human heart that includes the influence of FTs. Yet, such a model would constitute a valuable complement of clinically-motivated studies for simulating and understanding the effects of FTs on specific aspects of the cardiac function such as electrical conduction. Furthermore, it would allow the study of the role of FTs under a wide range of scenarios through the use of virtual populations and numerical simulations, both in the healthy heart and also in relation to specific cardiac anomalies, such as the LBB block.

LBB block is a condition affecting 1-2% of the general population [131], for whom the activation of the left ventricle (LV) is delayed due to the disruption of the electrical conduction along the LBB. In the presence of a complete LBB block, the LV is activated by the electrical stimulus propagating from the right ventricle (RV). Thus, the overall ventricular activation time increases, as reflected by the widening of the QRS complex in the surface ECG.

As the risk of cardiovascular mortality increases for QRS lengths above 80 ms [132], patients suffering from this condition may benefit from cardiac resynchronisation therapy (CRT). However, the installation of CRT devices carries inherent risks, and international clinical guidelines [133,134] indicate an empirical threshold ($QRS_{d,TH}=120$ ms) of the QRS duration (QRS_d), below which CRT is not recommended. On the other hand, FTs could in principle reduce QRS_d and thus the risk of cardiovascular mortality.

Consequently, the objective of this chapter is twofold. First, to the best of the thesis authors knowledge the first computational model of the human heart that includes a FT is proposed. Subsequently, the model is used to test the hypothesis that the presence of FT in the LV reduces the LBB block induced QRS prolongation. The reduction is then quantified with respect to the cardiovascular mortality risk based on [132], in particular whether the QRS_d falls below $QRS_{d,TH}$.

To this end, the following key technical challenges are addressed: 1) Derive a representative virtual population of ventricular models, where each shape is manually checked for mesh intersection and repaired if needed. For the ventricular models different configurations of FTs are generated. 2) Introduce a computational approach for modelling the PMs, which is a critical step in this process as FTs are in some configurations connected to the PMs. 3) Extend the existing literature on the PN to incorporate both the PM and FTs. 4) Generate several types of FTs based on the existing literature from autopsies and histological studies. To validate the model, a total

	Reference	Study size	FT prevalence (%)
(a)	Gerlis <i>et al.</i> [135]	686	48
	Luetmer <i>et al.</i> [16]	483	55
	Boyd <i>et al.</i> [136]	474	68
	Abdulla <i>et al.</i> [20]	100	34
	Grzybiak <i>et al.</i> [137]	180	40
	Kervancioglu <i>et al.</i> [17]	8	63
(b)	Okamoto <i>et al.</i> [138]	132	46
	Nishimura <i>et al.</i> [139]	1000	<1
	Perry <i>et al.</i> [140]	3847	<1
	Suwa <i>et al.</i> [26]	1117	6
	Sethuraman <i>et al.</i> [141]	1012	<1
	Brenner <i>et al.</i> [142]	100	61
	Vered <i>et al.</i> [143]	2079	2
	Malouf <i>et al.</i> [144]	488	25
	Casta and Wolf [22]	218	14
	Suwa <i>et al.</i> [27]	187	71
	Cangelosi <i>et al.</i> [145]	916	26
	Cocchieri and Bardelli [146]	273	29
	Kervancioglu [17]	368	26
	Lie <i>et al.</i> [147]	99	85

Table 5.1: Studies of the Prevalence of False Tendons (FTs) in the Human Heart by (a) Autopsy and (b) Echocardiography.

of 560 simulations of the ventricular activation time are performed to assess the action potential (AP) propagation under different FT configurations and in the presence or absence of a LBB block.

5.2 Methods

The proposed computational model requires the modelling of various structures and elements that are involved in the definition and electrical function of FTs. These include the ventricles, within which the FTs are located. In this *in silico* study, a virtual population of 70 ventricles is generated from a statistical shape model (SSM) of the heart, as detailed in Section 5.2.1. Next, the computational model is enriched, as described in Section 5.2.6, with PMs as they can serve as connection points for the

FTs. Additionally, due to its importance in electrical conduction, a new PN that takes into account the presence of PMs is generated in Section 5.2.3. The modelling of the FTs themselves is presented in Section 5.2.4. Finally, using the solver and protocol detailed in Section 5.2.6, simulations of the ventricular activation time are performed based on the introduced computational model and the virtual population of ventricles.

5.2.1 Ventricular Model

To simulate the effect of FTs on the human heart, a sample of hearts with variable ventricular geometries is required. Previous simulation works have used simplified geometries of the LV as discussed in Chapter 1, which can differ from the human heart in many aspects. Instead, in this chapter a virtual human heart population is generated from a SSM, which accounts for differences in the shape and size of the ventricles, but without linking the hearts into any specific patient instances.

More specifically, the *in silico* population of human ventricles produced in this study is based on the SSM of heart by Hoogendoorn *et al.* [68], which was built from 134 real patients based on high resolution CT image data, which resulted in high quality and realistic surface meshes of the cardiac structures. Such a SSM is typically constructed from a representative sample of human subjects and provides an average shape of the anatomy, together with the main axes of deviations from this average. Mathematically, each shape can be described using the following equation:

$$\hat{\vec{S}} = \vec{\bar{S}} + \Phi \vec{b}, \quad (5.1)$$

where $\hat{\vec{S}}$ is a vector of size $3m$ representing the shape in terms of its m 3D landmark points. Here $\vec{\bar{S}}$ corresponds to the mean shape of the model and Φ is a $3m \times t$ matrix that encapsulates t eigenvectors describing the main directions of variation in the model. Each unit vector is associated with an eigenvalue λ_i , $i \in \{1, \dots, t\}$ that describes the amount of variation observed along each axis. Finally, $\vec{b} = (b_1, \dots, b_t)^T$ is a vector that encapsulates the b_i weights that control the deviation of the shape $\hat{\vec{S}}$ from the mean $\vec{\bar{S}}$.

For this chapter the choice $t = 10$ modes of variation is made to generate the virtual shapes, by randomly varying the deviation weights b_i within the allowable bounds of the model $-3\sqrt{\lambda_i} \leq b_i \leq +3\sqrt{\lambda_i}$ [67]. A virtual population of 70 ventricular meshes is generated and used to run a large number of AP propagation simulations based on

varying configurations of the PMs, FTs, and the PN, as detailed in subsequent sections.

5.2.2 The Papillary Muscle

The PMs are common endpoints for the FTs and therefore they must be modelled so that the computational model has the capability to represent such configurations. However, due to the complexity of PMs, *in silico* models of the heart usually do not include PMs (nor the trabeculae). In this thesis a statistical approach to PM modelling is proposed. More specifically, seven computed tomography (CT) datasets of the 134 datasets in [68] are used to assess key anatomical features of the PM [148–150]. These include length, diameter, attachment points, angle inclination from base to tip, and distance to the LV (more details can be found in Table 5.2). Subsequently, the statistical variability of these parameters was estimated, which allows to generate in new virtual PMs with varying properties. Only subjects with a single posterior PM and a single anterior PM are included in the sample. This is sufficient for the experiments with the FT, as the majority of FTs connect to one PM [19]. Furthermore, the anterior PM is in most cases singular [151].

The CT image data were acquired from patients who underwent a CT examination as part of their routine diagnostic protocol for suspected coronary artery disease. The CT scanner used for this purpose was a 64-row detector Toshiba Aquilion 64 system (Toshiba Medical Systems, Tochigi, Japan), with contrast material of 80 to 100ml Xenetic 350 applied at a rate of 5ml/s, which allowed to enhance the appearance of the PMs. The obtained resolution of the images was of $0.4 \text{ mm} \times 0.4 \text{ mm} \times 0.8 \text{ mm}$.

To obtain the length, diameter and direction from the base to the tip of the PM (referred to as orientation), key anatomical landmarks were consistently defined on the CT images by using the medical image analysis software GIMIAS¹. More specifically, four landmarks were selected manually as the center point of the area where the PM joins the LV (*i.e.*, attachment point), the tip of the PM and two landmarks that determine the diameter of the PM (Fig. 5.1). Two further quantities were automatically calculated from a LV SSM instance, which were fitted to the image, *i.e.* the center of the mitral valve and the left ventricular apex. Table 5.2 shows the relationships

¹The Graphical Interface for Medical Image Analysis and Simulation (GIMIAS) v1.5 (www.gimias.org) is developed by the Center for Computational Image and Simulation Technologies in Biomedicine (CISTIB) at The University of Sheffield (UK)

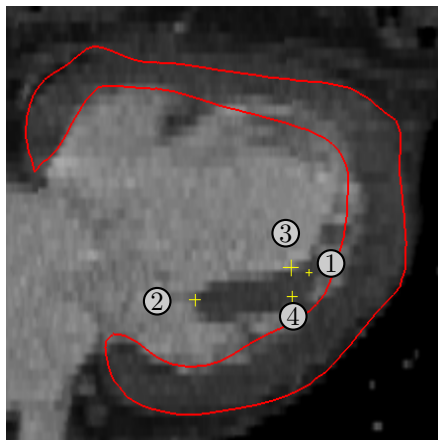


Figure 5.1: A computed tomography slice and mesh of the left ventricle (red) with the landmarks (yellow). This has been used to build the statistic of the papillary muscle: (1) Attachment point (2) Tip of papillary muscle, (3-4) Landmarks for the diameter estimation.

between the landmarks and the PM parameters, together with the mean and standard deviation values.

The PM model in this work is represented by combining a cylinder and a paraboloid, where this choice of shape is based on images of PM found in the literature [151–153]. The parameters for the cylinder and paraboloid are indicated in Table 5.2. The cylinder is defined as 60% of the PM length. The remaining part of the PM is represented by the paraboloid given in cylinder coordinates with origin at the center of the bottom of the cylinder $z(r, \phi) = L - 4 \cdot 0.4Lr^2/(d^2)$ where d is the diameter of the resulting PM, L is the length, $0.4L$ is the height of the paraboloid, and r is the radial direction.

The PM is then placed at one of the statistically defined attachment points, oriented according to the statistics, and merged with the ventricular model, which results in a new LV surface with a PM as illustrated in Figure 5.2.

5.2.3 Purkinje Fibre Generation

The pattern in which the AP travels in the ventricle is critical to the efficiency of the heart contraction and, therefore, it is important to consider the PN in our simulation. As discussed in Section 2.2.2, the PN is difficult to image and is therefore constructed with an algorithm. However, existing techniques do not take into account the presence

Parameter	Landmark relation	APM	PPM
LV axis	A line connecting the LV apex and the center of mitral valve.	N/A	
LV length in [mm]	Length of the LV axis.	98.0 ± 8.5	
Normalised [†] PM diameter	Distance between landmark ⁽³⁾ and ⁽⁴⁾ .	8.9 ± 1.7	8.3 ± 1.9
Normalised [†] PM length	Distance between the attachment point ⁽¹⁾ and tip ⁽²⁾ .	33.6 ± 5.3	27.6 ± 5.5
PM attachment triangle	The triangle in the LV-Mesh that is closest the attachment point ⁽¹⁾ .	N/A	N/A
Angle in degree between PM tip and attachment point	Angle between the line from the attachment point ⁽¹⁾ to the LV axis and the line from the tip ⁽²⁾ to the LV axis in a plane perpendicular to the LV axis.	19.9 ± 6.3	27.8 ± 12.2
PM tip distance in [mm] from LV	A line starting from the LV axis and perpendicular to it through the tip point and intersection the LV-Mesh.	24.1 ± 3.1	21.7 ± 3.8

⁽ⁱ⁾ Landmark (i) in Fig. 5.1, for $i=\{1,2,3,4\}$

N/A: Not applicable

[†] normalised with respect to LV length and multiplied by 100

Table 5.2: Statistical Parameters of the Anterior Papillary Muscle (APM) and the Posterior Papillary Muscle (PPM), Calculated from Landmarks in the Left Ventricular (LV) Computer Tomography Scans.

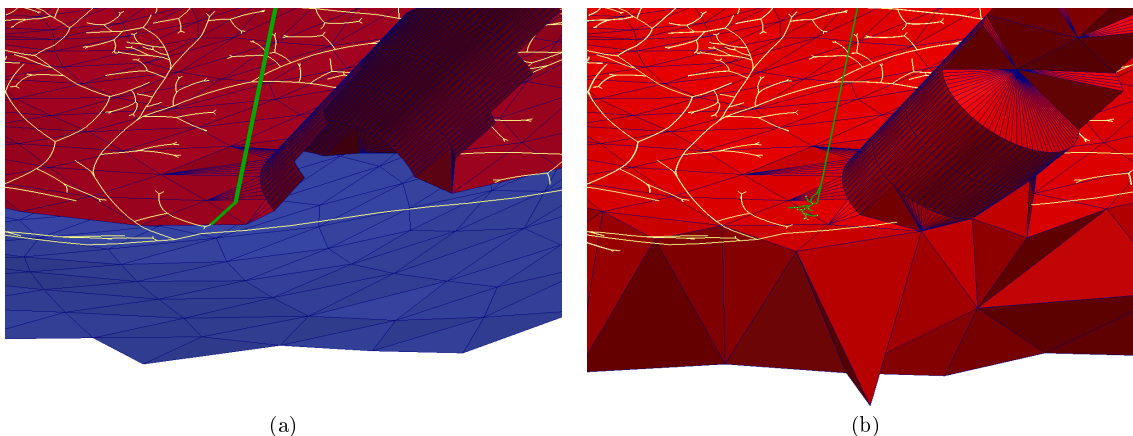


Figure 5.2: Different terminations of the false tendon (green) with Purkinje network (PN) (white). (a) False tendon directly connected to the main PN, on a left ventricular surface based on triangles with papillary muscle, where the endocardium is red and the epicardium is blue. (b) False tendon terminating in small Purkinje fibre branching, on a left ventricular volume mesh based on tetrahedra with papillary muscle, with myocardium in red.

of PMs and FTs. Therefore, an extension of the algorithm of Sebastian *et al.* [4] is proposed to account for these additional structures, as well as to adapt it for the RV.

The PN is algorithmically generated with an L-system. This iterative process uses two basic elements, *i.e.*, L- or Y-shaped structures, which are generated progressively from a given starting point. For the Y-structures, the direction of growth is from the lower part to the upper part, which then creates two new starting points. In L-structures, the growth starts at the lower left corner and advances toward the two endpoints, which in turn creates new starting points. At the next iteration, a new starting point is randomly selected from the set of starting points. With this implementation the resulting network depends on the angle of the L- or Y-structure, the length of the branches, and the number of points from which each of the segments are built, because they allow structure flexibility and thus the newly grown fibres can avoid the already existing network. More details can be found in [4].

The modified algorithm for the generation of a PN in the LV consists of three stages, where the first is landmark driven and the last two are deterministic rule-based. In the first stage the LBB and the three main branches are created (Fig. 5.3, (a)). To do so a Purkinje fibre is generated from the starting point of the LBB in the direction of

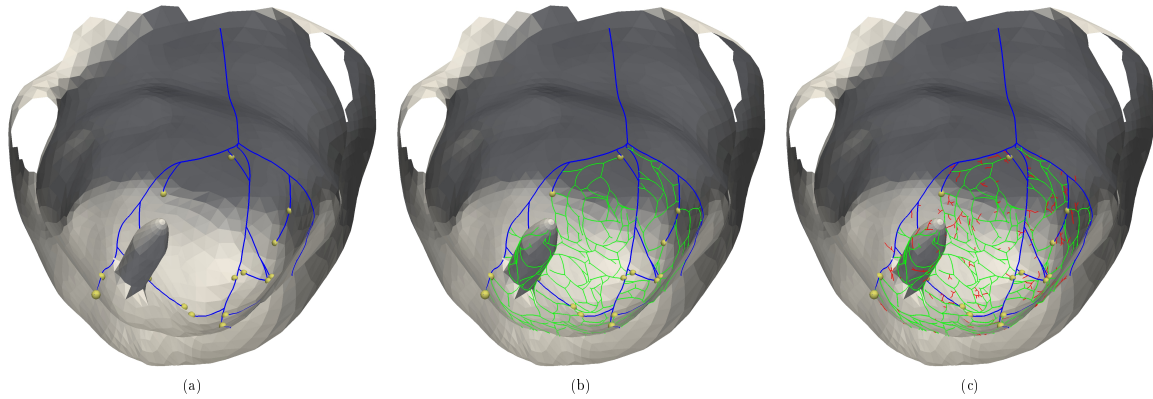


Figure 5.3: The three stages of the Purkinje growing algorithm. (a) First stage with main fibres in blue and endpoints marked by yellow sphere, (b) finer second stage in green and (c) with final branching of the last stage in red.

the ventricular apex, and branches after two-thirds of the way in the three main fibres. Two of these fibres proceed towards the posterior PM and anterior PM, respectively, and the third towards the apex. After reaching their landmarks all fibres are grown towards the base of the heart, where they stop 2 cm before reaching the basal plane. After the three main fibres have been grown with an L-rule, a deterministic fibre generation at the endpoints is started with an Y-rule. Note that all the branches are grown underneath the PM (Fig. 5.2, (a)) and continued on the endocardial surface after passing the PM. The second stage (Fig. 5.3, (b)) creates new Y-structures at the endpoints of the developing PN, which extend onto the PM. The last two stages create a homogeneous network with loops for redundancy, while the final stage (Fig. 5.3, (c)) increases the density of Purkinje-muscle junctions (PMJs), without creating looping Purkinje fibres. Therefore, based on the American Heart Association segment model [73], random points are selected from the previous PN and used as possible starting points. At some of these points smaller Y-structures are generated.

For the RV, the bundle is grown from the atrio-ventricular node towards the apex of the RV. Again, at two-thirds of the way the branch splits in two, where one branch progresses to the apex and the other crosses to the right ventricular wall [8]. The second and third stages are essentially the same as for the LV, and differing only in stage two, which begins with only two starting points and in which the fibres do not avoid each other.

The growth parameters for the LV and RV are summarised in Table 5.3.

5.2.4 Creation of False Tendons

After generating the PN, as detailed above, the main object of study of this chapter, the FT, is finally incorporated to the computational model of the electrical conduction system of the heart.

The FT model is based on clinical observations that 60% of FTs feature conductive tissue [19] and this tissue shows the same microscopic structure as the bundle of His. Moreover, the fibres are connected to the bundle of His [19,20,154], which suggests that the bundle of His radiates into the FTs [19,20]. For this reason, the FTs are modelled as additional Purkinje fibres, which are attached to either the ventricular free wall (VFW), the septum, or the PMs. This simplification has been made because the fast conduction tissue is the only tissue of the FT that influences the total activation time.

The modelling process begins by automatically selecting the starting point of the FT at the LBB, and by selecting the endpoint on the anterior PM, posterior PM, or the VFW, depending on the desired FT configuration. Due to the lack of knowledge on how the Purkinje fibre in the FT merges into the PM or ventricular muscle, two different connection type are distinguished at the endpoint. The first one is a direct connection of the Purkinje fibre in the FT to the PN on the LV, which is constructed by an additional Purkinje fibre segment that connects the endpoint of the FT to the closest Purkinje fibre point (Fig. 5.2, (a)). The second case is a delta connection, which branches from the endpoint of the FT into a tree of Purkinje fibres. This is achieved with the PN growing algorithm starting at the endpoint with a segment

	Second step		Third step	
	LV	RV	LV	RV
Branch Length [mm]	6 ± 0.3	4 ± 0.3	1 ± 0.03	1 ± 0.03
Branch angle [degree]	60 ± 40	60 ± 20	60 ± 40	60 ± 40
Number of Segments	10	10	5	5
Max. branches	300	800	600	1000

Table 5.3: Values used for the Deterministic Purkinje Network Growing in the Left Ventricle (LV) [4] and Right Ventricle (RV)

length of 0.2 ± 0.1 mm and a branching angle of $60.0 \pm 1.0^\circ$. The algorithm generates ten branches, which do not connect to the main PN. (Fig. 5.2, (b)).

5.2.5 Modelling of a Left Bundle Branch Block

In this study, the influence of FTs on hearts with conduction disturbances is investigated. Since the FT provides an additional conduction path from the bundle of His to the PN, it is important to understand its benefit in the presence of a LBB block.

The LBB block in the PN is modelled by assuming that the activation of the FT is not affected, which means the LBB block occurs downstream of the FT insertion point. This assumption is supported by the reported origin of the FT from the bundle of His and a recent publication [155], who reports a case of LBB block in the presence of a FT. In that particular case the FT is connected to the VFW and it is reported that the lateral LV wall contracted during systole and relaxed during diastole, whereas the septum expanded during systole and contracted during diastole [155]. This behaviour can originate from an AP travelling through the FT and activating the VFW.

The chosen region for the LBB block is assigned a flag in the computational model, such that in the AP propagation simulation the conduction velocity is assumed to be zero. This corresponds to a full conduction block.

5.2.6 Ventricular Activation Time Estimation

In the Section 5.3, the effects of FTs on the electrical activation of healthy hearts and on hearts with a LBB block is studied. To this end, AP propagation simulations need to be carried out, for which different modelling approaches exist. For the intended experiments an estimate of the ventricular activation time is needed, while the ionic currents over the cell membrane will not be altered or be of interest. For this reason, the eikonal equation is chosen to model the AP propagation. This describes the wave propagation according to a prescribed constant conduction velocity without modelling the cell membrane. More importantly, it has been shown that the eikonal approximation gives good approximation of the myocardial activation time [91–93] needed for our experiments. The monodomain and bidomain models (Sec. 2.1.3) are diffusion reaction models, which are usually solved with a spatial discretisation method, such as finite volumes or finite elements [156], on a high resolution volume mesh (1 000 000 vertices

or more). This makes the models computationally very demanding, and unsuitable for the large number of simulations we intend to run.

The following eikonal problem is solved with the fast marching method [101]

$$\begin{cases} \nabla u \mathbf{A} \mathbf{F} (\mathbf{A} \mathbf{F})^T \nabla u^T - 1 = 0 & x_i \in \Omega \\ u(x_i) = u_0(x_i) & x_i \in \partial\Omega, \end{cases} \quad (5.2)$$

where Ω is the problem domain, u_0 are the known activation times and u is the activation time to be obtained, the orthogonal matrix \mathbf{A} is composed from the unit vectors pointing along the myocardial fibre orientation and \mathbf{F} represents the conduction velocity on the diagonal.

For the simulation, tetrahedral volumetric meshes with approximately 70 000 vertices (Fig. 5.2, (b)) are generated from the ventricular surfaces with PMs using the **TetGen** library². For all vertices of the tetrahedral mesh, the myocardial fiber orientation is estimated using the Streeter model [34] with a linear interpolation between endocardium and epicardium. While for the RV and LV the same rules are applied for vertices in the PM the fiber orientation is aligned to the long axis of the PM as described in [157, 158] (Fig. 5.4). At the border between ventricle and PM the fibres are locally smoothed by the solver as it uses the average fibre orientation per tetrahedra.

The volumetric mesh together with the one dimensional PN provides the spatial domains Ω within which the eikonal equation is solved for the estimation of the activation time of the heart. Both domains are coupled at the endpoints of the PN, where the AP propagation from the PN to the myocardial system is delayed by 6 ms and 1 ms in the opposite direction [159, 160]. Here, the PN includes the FT, such that there is no additional delay between the normal PN and the FT fibre. In the case of a delta ending only, which connects the FT to the myocardium, a delay of 6 ms is applied.

The eikonal equation is solved with the fast marching method proposed in [101], where the myocardial conduction velocity is equal to 0.8 m s^{-1} in the longitudinal direction and to 0.3 m s^{-1} in the transversal direction. For the PN and for the FT, the conduction velocity is set to 3.5 m s^{-1} .

²The **TetGen** (<http://wias-berlin.de/software/tetgen/>) Delaunay tetrahedralization library is developed by the Numerical Mathematics and Scientific Computing research group at the Weierstrass Institute for Applied Analysis and Stochastics.

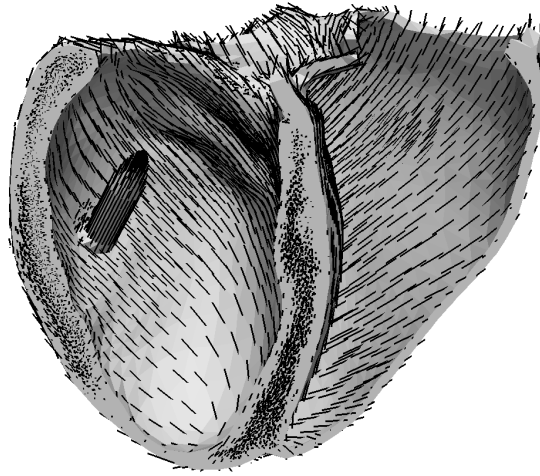


Figure 5.4: Myocardial fibre orientation generated with the Streeter model in one exemplary heart.

5.3 Virtual Population Experiments and Results

5.3.1 Sensitivity of the QRS_d to Different Purkinje Network Topologies

Before evaluating the computational model of the FTs, the variability of the QRS_d due solely to different configurations of the PN is estimated. Therefore, the mean ventricular mesh with PMs is used and a volumetric mesh with fibre orientations is generated. To this ventricular model the PN growing algorithm (Sec. 5.2.3) is applied with the parameters from Table 5.3, *i.e.*, for a total of 25 different PNs. Two parameters (length, branching angle) were varied following a Gaussian distribution (Table 5.3), while the remaining eight parameters were fixed. For each of the PN, the eikonal equation was solved with the same ventricular geometry and the myocardial activation time was estimated. From the myocardial activation time, the QRS_d was calculated as the time difference between the first myocardial activation and the time at which the entire myocardium has been activated. The electrical charge in the PN is negligible and will not be captured by a surface ECG [58, 161]. A mean QRS_d of 108 ± 6 ms was obtained with a range from minimal 94 ms to maximal 118 ms. For the aforementioned simulations the model did not include FTs.

5.3.2 Influence of False Tendons on the Ventricular Activation Time

The aim of the following experiment was to investigate the influence of different FTs configurations on the QRS_d . To do so, simulations with 560 different heart model configurations were conducted, based on the 70 virtual ventricle shapes as generated in Section 5.2.1. For each shape, a PN was constructed, which was then supplemented with the addition of a FT. Resulting in six new configurations (Fig. 5.5) where the FT connected into the posterior PM, the anterior PM or the VFW(three subtypes) and each of the FTs was created either with a direct connection at the end, or with a delta connection (two subtypes). All the simulations on these configurations were run with a PN featuring a LBB block and an additional simulation with the healthy PN without LBB block and FT. In total, this resulted in 8 different configurations per geometrical shape (*i.e.*, 560 simulation runs).

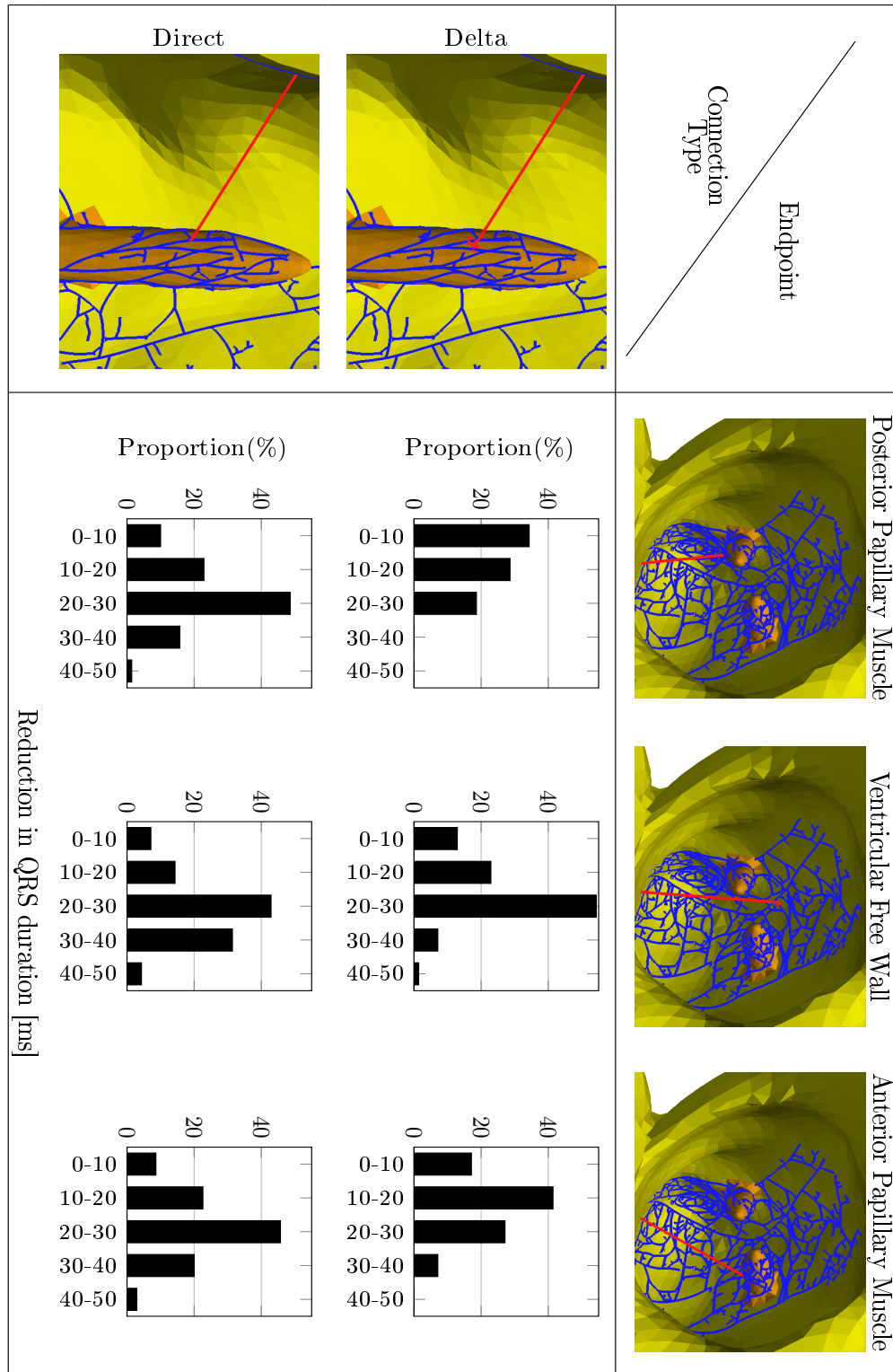


Figure 5.5: Shortening given for the direct and delta connected false tendon to various endpoints. The mean QRS duration without FT was 131.9 ± 7.1 ms

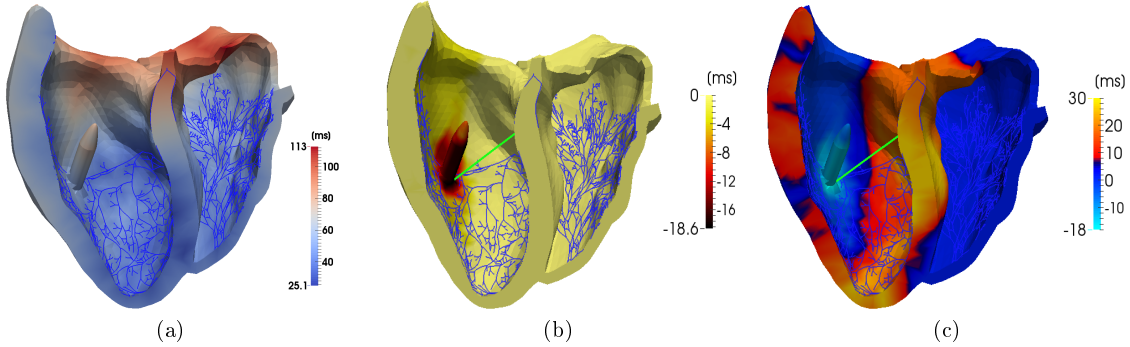


Figure 5.6: Comparison of the activation pattern with and without false tendon for the same heart. (a) The local activation times for the heart without FTs, (b) difference in the activation time of the heart with a FT to the ventricular free wall, (c) the same with a left bundle branch block and a FT to the anterior papillary muscle.

Quantification of the influence of the FT on the AP propagation was based on the reduction of the LBB block induced QRS_d prolongation observed between the "LBB block, no FT" and "LBB block with FT"-cases (the difference in QRS_d is denoted by QRS_{Diff}). As each 10 ms increase above the QRS_d of 80 ms has been associated with 10% increase in cardiovascular mortality risk [132], the FT-induced reduction of QRS_d is quantified by 10 ms intervals. Subsequently, it is tested whether the total ventricular activation time was reduced to such an extent that QRS_d would fall below $QRS_{d,TH}$, such that CRT would not be recommended by international guidelines. Finally, the Kolmogorov–Smirnov test is used to investigate the similarity of the population featuring a LBB block with FT and without FT to the healthy population.

For the healthy heart, the experiments revealed a QRS_d of 108 ± 7.1 ms, which is only slightly affected by a FT. However, the activation time near the FT attachment point decreases locally (Fig. 5.6 (b)). The control cases with a LBB block but without FTs show an increased mean QRS_d to 131 ± 9.8 ms. This is an expected result since the LBB block disrupts the conduction toward the PN, delaying the activation until its breakthrough at the septum from the RV.

However, the experiments with a LBB block shows a clear benefit from the presence of a FT. The simulations including FTs to the VFW show the shortest mean QRS_d , while a FT connecting to the posterior PM gave the only mean QRS durations above the threshold $QRS_{d,TH}$. In general, the direct connection results in shorter QRS_d than

QRS Duration	No FT		LBBB and Direct FT to			LBBB and Delta FT to		
	Healthy	LBBB	APM	PPM	VFW	APM	PPM	VFW
Mean [ms]	108.5 ± 7.1	131.9 ± 9.8	108.1 ± 7.5	110.1 ± 6.5	105.8 ± 7.1	116.0 ± 9.6	124.3 ± 11.74	111.5 ± 7.1
> T_{th} in %(n)	4 (3)	94 (66)	4 (3)	9 (6)	4 (3)	31 (22)	57 (40)	10 (7)

Table 5.4: The mean QRS duration for n=70 geometries and different configurations of the heart model, and the proportion with QRS duration longer than the threshold $Q_{d,TH}=120$ ms. (LBBB) Left bundle branch block, (PPM) posterior papillary muscle, (APM) the anterior papillary muscle, and (VFW) the ventricular free wall

the delta connection (Table 5.4), which may be explained by the fact that the electrical impulse propagates partly in the slow conduction myocardium before re-entering the PN.

In most cases, the presence of a FT decreased the QRS_d by more than 10 ms (Fig. 5.5). Badheka *et al.* [132] showed that this reduction indicates a more than 10% lower risk of cardiovascular mortality. FTs with direct connection showed a QRS_{Diff} of 20 ms or more, suggesting a stronger effect of the alternative conduction pathway produced by FTs of this type. In few cases the FT prolonged the QRS_d . This might be explained by an earlier onset of the AP in the myocardium due to the FT, but the total activation time is still determined by the AP front originating from the RV (Fig. 5.7).

Evaluating the QRS_d with respect to the CRT treatment recommendation showed a benefit from the FTs (Table 5.4 and Figure 5.8 (b)). To see this the subjects with LBB block and no FT are compared to subjects with LBB block and FT. In case of LBB block, the majority of the subjects, 94%(n=66), have a QRS_d longer than the threshold $QRS_{d,TH}$. For a LBB block in conjunction with a FT and delta connection, only 33%(n=69) of the subjects have a QRS_d longer than $QRS_{d,TH}$. With a direct connection of the FT, even fewer subjects remain over the threshold, 8%(n=16).

Subsequently, the differences in the cumulative distributions of the QRS_d (Fig. 5.8) are compared with a two sample Kolmogorov-Smirnov test, which confirmed with a significance of $\alpha = 0.01$ the similarity of the healthy heart with that featuring a FT with direct connection and a LBB block. In contrast, when comparing the healthy heart with a pathological heart due to a LBB block, the Kolmogorov-Smirnov test is still rejected at the much smaller $\alpha = 0.0001$.

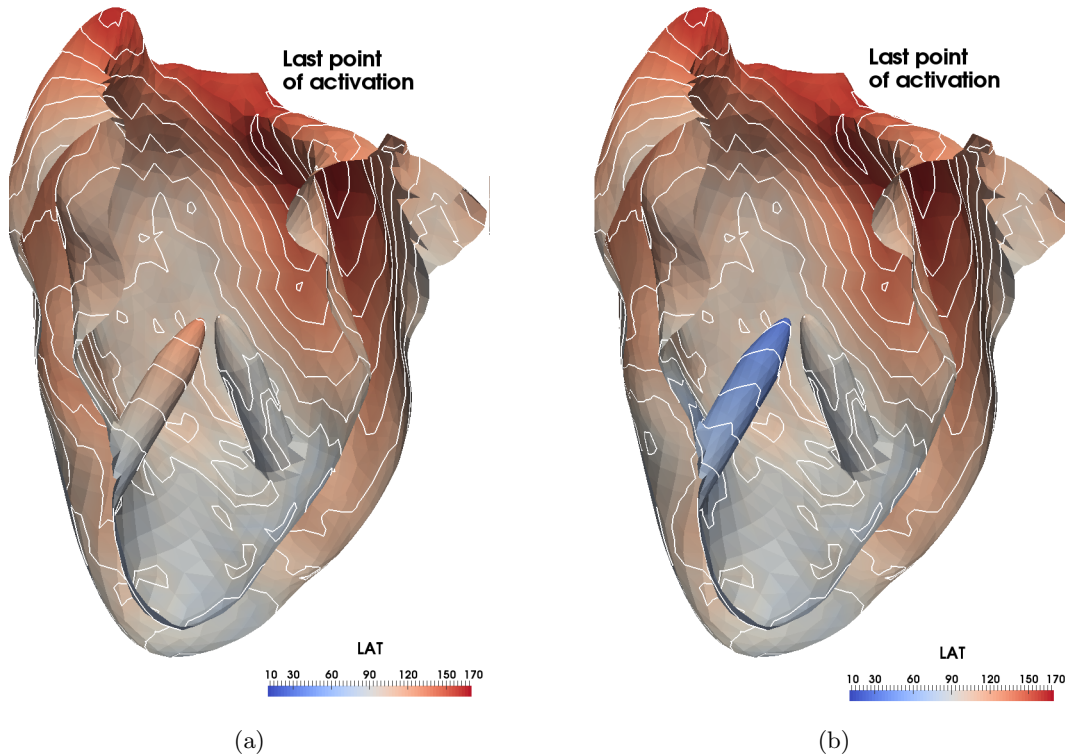


Figure 5.7: QRS_d prolongation. In a few cases the QRS duration may be prolonged by adding a false tendon. (a) without false tendon, the last point activated is still reached by the wave front from the right ventricle. (b) with false tendon there is an earlier onset of myocardial activation, here seen in the papillary muscle.

5.3.3 Synchrony in Left and Right Ventricular Activation

In this experiment, the synchronous activation of the LV and RV is examined for a healthy heart, a heart with a LBB block, and a heart with a LBB block and a FT. To do so, a cumulative histogram of activated tissue (Fig. 5.9) is employed.

To measure the synchronicity of the activation, the myocardium is manually divided in the LV and RV by a planar boundary in the middle of the septum (Fig. 5.10). Subsequently, the first activation time in the LV is extracted, as well as the time from the onset of the activation in the His bundle until the last point in the LV becomes activated. For the RV, the same measures were calculated. Finally, the time difference between the last point of activation in the RV and the last point of activation in the LV is calculated to evaluate the (dys)-synchrony of the cardiac activation.

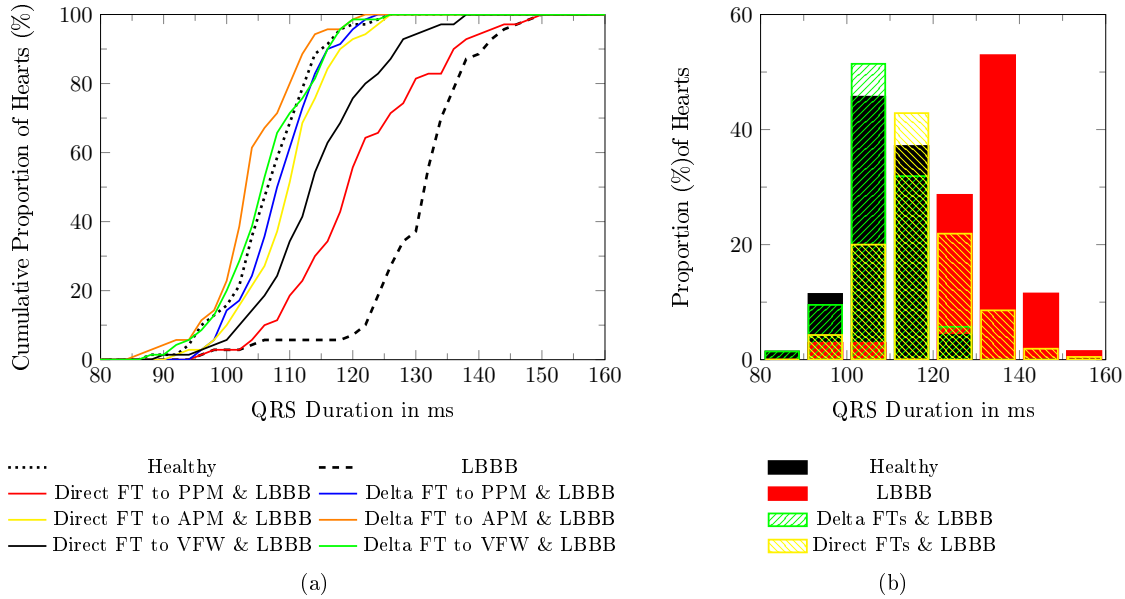


Figure 5.8: Histogram of the QRS_d in the study population ($n=70$). (a) Cumulative histogram for all sub groups, (b) Histogram for the healthy, the LBBB, all case with direct connected FT and LBBB and all case with delta connected FT and LBBB. (LBBB) left bundle branch block, (PPM) posterior papillary muscle, (APM) anterior papillary muscle, (VFW) ventricular free wall, (FT) false tendon.

The results (Table 5.5 and Figure 5.9) indicate that the dys-synchronous activation of the LV and RV in a LBB block is compensated for by the presence of the FT. The initial activation of the LV in the presence of a LBB block but without a FT occurs 12 ms later compared to the healthy heart. In the presence of a FT, however, this difference is reduced to 4 ms only. The third row in Table 5.5 shows that in the healthy case, the LV was fully activated after 97 ms, while in the case with a conduction block, 125 ms elapsed before full activation. This difference in activation time can be overcome by a FT, whereby the LV is activated 11 ms earlier. In the presence of a FT, the activation in the LV proceeds within the same period as in the healthy case, but from a different starting point (Fig. 5.6 (a) and (b)). The AP travels from the FT to the PM toward the septum and basal area. The activation in the direction of the basal area is comparable to the healthy case, but the activation of the apex and the septal region occurs later. Thus, even when the total activation times are within a healthy range, the contraction pattern needs to be evaluated before the efficiency of

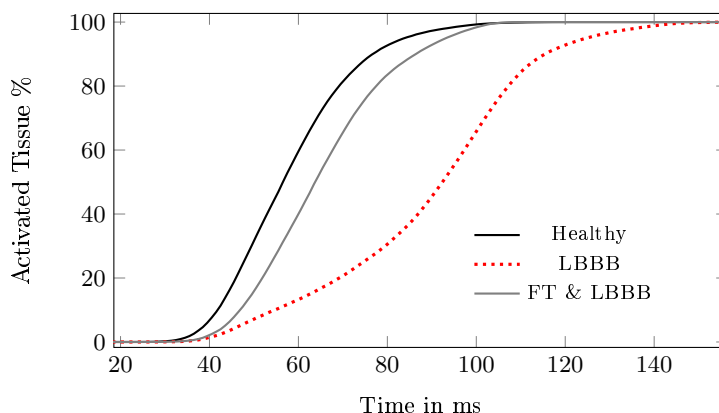


Figure 5.9: Percentage of activated tissue for the healthy heart, the same heart with left bundle branch block (LBBB), for a heart with a direct connected false tendon (FT) to the ventricular free wall and LBBB. The heart in healthy condition and the case of a LBBB with FT are similar, while in case of a LBBB the slope is smaller.

the contraction can be judged.

It is worth noting that the RV is affected in the same way by the LBB block and the FT. The main effect is the missing activation in the septal area due to the failure of activation from the LV.

5.3.4 The Effect of Heart Size and Shape on the False Tendon induced QRS_d Reduction

So far this study has looked at different types of FT across a virtual population of heart shapes to evaluate the possible benefit of a FT in case of a LBB block. An interesting additional question is: What influence do the shape of the heart, the size of the heart, or the FT configuration have individually on the ventricular activation time or when compared against each other? Therefore, an additional study is performed consisting of three different sample populations to characterise the influence of each of these three factors independently from each other. For simplicity, the size of the heart is defined as the LV length.

The first population (P1) was generated by choosing randomly four heart shapes of the 70 hearts in Section 5.3.2 and then scaling them to have LV length between 70 mm to 90 mm with 2 mm intervals. For each of the 44 hearts, a PN with and without FTs has been generated, where the attachment point of the FT to the anterior PM/posterior

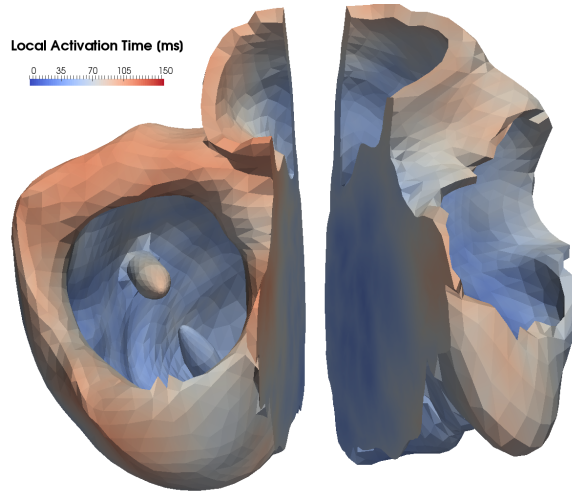


Figure 5.10: Manual division of the myocardium by a plane in left and right ventricle, used to estimate the activation time in the different ventricles.

PM was fixed on the top of the PM and the FT to the VFW was always attached at the same point on the VFW. This population was used to characterise the effect of size on ventricular activation time.

The second population (P2) was generated to characterise the effect of heart shape. It was built using all 70 shapes from Section 5.3.2, but rescaled to a fixed LV length. For each shape a PN was generated with all types of FT, where the attachment points were fixed to match those used in P1.

In the third population (P3), the FT attachment point on the VFW was varied. Therefore, the four heart shapes previously used to generate P1 were scaled to 80 mm LV length, and a PN without FT was generated. These four PNs were then used as a basis for PNs with FT connecting to the VFW. Randomly chosen attachment locations of the FT in the VFW were selected to generate 50 different PNs per shape.

By performing simulations using the eikonal model, it can be studied how the ventricular activation time is affected by the LV size in P1. To quantify this, the definition of QRS_{Diff} is recalled, which is the change in ventricular activation time observed between the "LBB block, no FT" and "LBB block with FT"-cases (Tab. 5.6). As one would expect, the ventricular activation time has a general tendency to increase as the LV length increases, as shown for one case in Figure 5.11 (top). Somewhat surprisingly, the suspicion that QRS_{Diff} would show the same behaviour turns out not to hold in this

Activation time [ms]	Healthy	LBBB	FT&LBBB
First LV	23	35	27
First RV	26	26	26
Total LV	97	125	86
Total RV	73	98	86

Table 5.5: For a healthy heart, the same heart with left bundle branch block (LBBB) and the same heart with direct connected false tendon (FT) to the ventricular free wall and LBBB times are compared. The time the action potential needs from the activation of the Bundle of His to the first activation in the left ventricle (LV) and right ventricle (RV) are compared, and the time elapsing from the first activation in the LV/RV to the last activation in the LV/RV. This reveals that in case of LBBB the RV and LV are not synchronous in activation, but a FT reinstates part of the synchrony.

particular case. Initially increasing with LV size, QRS_{Diff} seems to reach a particular value and then plateau out (Fig. 5.11, bottom). This may indicate that the size of the LV has relatively little influence on the reduction in ventricular activation time, or that the effect will at least be less pronounced for small hearts.

To compare the change in QRS_{Diff} across populations rather than just between individuals, the interquartile range of variation in the QRS_{Diff} is reported as measure over P1, P2, and P3 respectively in Tab. 5.7. Applied to QRS_{Diff} the interquartile range gives the range of improvement in which 50% of the measured data lie. As such, the interquartile range quantifies the range of data distribution.

The interquartile range in P2 is in almost all cases much larger than in P1, with as much as four times the values in P1. This means that the range of improvement is much larger for the shape population compared to the size population. This conclusion is further supported by the fact that the mean QRS_{Diff} varies considerably between subjects in P1 (Tab. 5.7). Both observations together are strong indicators that in this model the improvement of the QRS_d in LBB block is more sensitive to shape than LV length.

The same analyses can be done between P2 and P3 to compare the sensitivity of shape vs. FT location. This comparison is even more striking, as it can be seen that for certain configurations the observed interquartile range can vanish, which is also reflected in the smaller standard deviation in P3 (Tab. 5.7). At first this appears

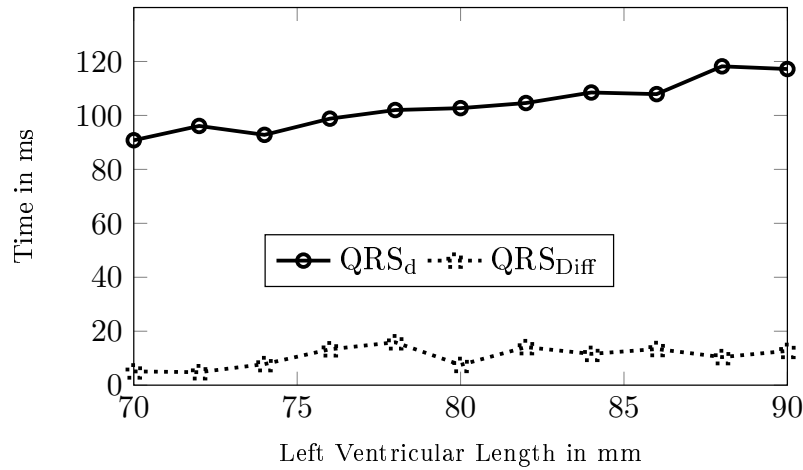


Figure 5.11: The QRS duration (QRS_d) for different sizes of the left ventricle, were a LBBB and a false tendon to the anterior papillary muscle is present. The improvement between the "LBBB, no FT" and "LBBB with FT"-case is given by QRS_{Diff} .

surprising, however an explanation is given by looking at the activation patterns. If the improvement by inserting a FT does not depend on the FT attachment location, it means that the last part of the heart to get activated is by an action potential arriving from the RV, which should be independent of the FT attachment point.

	PPM-Delta	PPM-Direct	APM-Delta	APM-Direct	VFW-Delta	VFW-Direct
P1: Case 1	4.69 ± 5.42	7.32 ± 4.46	4.16 ± 4.76	10.62 ± 3.60	8.46 ± 4.05	9.96 ± 3.91
P1: Case 2	9.41 ± 4.55	17.38 ± 4.26	17.00 ± 5.04	24.74 ± 3.55	19.22 ± 3.29	23.86 ± 2.23
P1: Case 3	8.95 ± 5.92	22.08 ± 4.87	11.55 ± 6.66	23.80 ± 5.33	21.30 ± 4.00	27.76 ± 3.99
P1: Case 4	10.83 ± 5.28	19.74 ± 3.63	8.96 ± 5.76	20.85 ± 2.83	21.24 ± 3.11	24.96 ± 2.53
P2	8.49 ± 8.64	18.96 ± 8.91	14.38 ± 8.80	21.23 ± 9.02	18.42 ± 8.23	23.73 ± 8.44
P3: Case 1	N.A.	N.A.	N.A.	N.A.	14.02 ± 0.00	14.02 ± 0.00
P3: Case 2	N.A.	N.A.	N.A.	N.A.	17.30 ± 2.36	20.26 ± 1.59
P3: Case 3	N.A.	N.A.	N.A.	N.A.	19.47 ± 2.68	23.86 ± 2.47
P3: Case 4	N.A.	N.A.	N.A.	N.A.	14.80 ± 2.44	15.91 ± 0.12

^{PPM} Posterior Papillary Muscle
^{APM} Anterior Papillary Muscle
^{VFW} Ventricular Free Wall
^{N.A.} Experiment Not Conducted

Table 5.6: Mean and Standard Deviation of the QRS_{Diff} [ms] in the Different Populations.

	P1 (size)				P2 (shape)	P3 (FT configuration)			
	Case 1	Case 2	Case 3	Case 4		Case 1	Case 2	Case 3	Case 4
PPM Delta	9.58	4.67	6.91	6.00	15.20	N.A.	N.A.	N.A.	N.A.
PPM Direct	8.16	6.03	4.57	3.41	9.64	N.A.	N.A.	N.A.	N.A.
APM Delta	6.07	5.57	10.67	10.29	10.51	N.A.	N.A.	N.A.	N.A.
APM Direct	5.68	3.48	5.32	3.72	10.83	N.A.	N.A.	N.A.	N.A.
VFW Delta	7.63	3.20	5.12	4.36	10.97	0.00	3.18	3.67	0.24
VFW Di- rect	6.50	2.40	4.19	2.32	9.29	0.00	1.61	3.23	0.00

^{PPM} Posterior Papillary Muscle

^{APM} Anterior Papillary Muscle

^{VFW} Ventricular Free Wall

N.A. Experiment Not Conducted

Table 5.7: Interquartile Range in [ms] of the QRS_d Improvement in each Population and Case.

5.4 Limitations

In this study, the eikonal equation was chosen for simulating AP propagation, which provides information on the activation times only. A limitation of this model is that it does not account for ionic currents in ventricular cells, and as such it is unable to simulate charge accumulation or arrhythmia. Even though the eikonal equation approximates the local activation times very well, the QRS_d estimated from a surface ECG can differ from the QRS_d measured on the endocardial surface.

Furthermore, the current model does not include multiple FTs in one heart, which

are occasionally observed [19], but our model could be extended to cover this possibility. A further limitation of the current model is that the FT is modelled as a single Purkinje fibre, whereas in the literature it has been observed that a FT can feature also myocardial and fibrous tissue, which could have a contribution in the electrical conduction. The work constitutes a first step towards more advanced simulations and one that is necessary to establish the importance of FTs in the study of cardiac physiology and function.

The current study does not investigate the exact relationship that the shape of the hearts and the FTs have on the reduction on QRS_d . Therefore, a parametrisation is needed where each parameter corresponds to clinically intuitive and identifiable features [162]. Such an approach would lend itself to visually assess FT effects on LBB block patients based on imaging data and supplementing the knowledge of the type of FT in question and surface ECG.

Measurements of the action potential in the PN are very limited and do not include systematic studies of the propagation of the AP. Moreover, reports of FTs in humans are very few and mostly limited to case studies, which makes it hard to validate our model against experimental data. Nevertheless, the eikonal equation and the PN model have been previously shown to reproduce local activation times reasonably accurately [91–93].

5.5 Discussion and Conclusions

This study demonstrates and quantifies for the first time the effect of the presence of the FT in terms of QRS_d . It has been carried out in anatomically accurate models of the heart in the presence of LBB block, where the FT is assumed to contain fast conducting fibres. This assumption is motivated by a recent observation by Irie *et al.* [155] and the similarities between Purkinje fibres in the FT and the bundle of His, but lacks extensive clinical evidence. However, the work provides a motivation for gathering further clinical evidence, as this study shows there are two possible ways in which the FT can influence the activation pattern. First, it may lead to a decreased cardiovascular mortality risk; and second, it may have practical implications on patient management.

The cardiovascular mortality risk is largely influenced by QRS_d as each 10 ms in-

crease above 80 ms has been associated with a 10% increase in the cardiovascular mortality risk, as shown by Badheka *et al.* [132]. In the *in silico* experiments, almost all cases show a QRS_d reduction, where the mean reduction was 20 ± 10 ms with a maximum of 45 ms. The shortened QRS_d is also reflected in an improved synchronous activation of the LV and RV. Overall, this indicates a substantial improvement, but also the treatment recommendation can be affected.

The amount of QRS_d reduction reported in this paper highlights the impact of FT on practical patient management. Current guidelines do not recommend CRT for LBB block patients with $QRS_d < 120$ ms. In this experiments 97% of simulation with no FT present had $QRS_d > 120$ ms, after introducing the effect of the FT, experienced a reduction in their QRS_d below the patient selection criteria. This effect however is dominantly present with FTs of the direct connection type. Therefore, both the presence of the FT and the structure of their attachment has to be taken into consideration. Overall, a FT seems to impact the QRS_d and affect the recommended management of LBB block patients. However, in the same way the presence of a FT can mask the severity of the LBB block.

By looking at the three parameters shape, LV length and FT attachment point, it has been established the QRS_d decrease seems to be most sensitive to shape, whereas size still influences the decrease to certain extent, and the FT location on the ventricular free wall has minor or no influence at all.

As any model, the model has limitations. With respect to this study, there are two important to keep in mind. First, the study was performed with the eikonal model, which only models wave propagation, but no charge accumulation or specific ion channels. The second is, that the treatment recommendations are with respect to the surface ECG, while our QRS_d are obtained within the heart.

Overall, the results demonstrated that in some cases of pathological conduction it is relevant to consider FTs in the electrical activity of the human heart. Future work should investigate FTs in more detail. A first step will be to further develop the model using the monodomain or bidomain equations and to refine the FT anatomical model. Such refined models could then be used to answer the question of how the FT might affect CRT outcome. Finally, the model could be used to begin explaining unusual ECG observations like inverted T waves.

Chapter 6

Automatic Creation of a Virtual Population to Investigate the Effect of the Purkinje Network Morphology on the ECG

In the previous chapter, it has been demonstrated that virtual population studies can be used to explore the false tendon (FT) in humans, where in this chapter a virtual population is used to explore how different coverages of the endocardium by the Purkinje network (PN) affect the electrocardiogram (ECG). This addresses the two remaining objectives: to present an automatic pipeline, and investigate the PN morphology.

The automatic pipeline presented in this chapter consist of five computer programs. The first, for the *in silico* generation of new heart shapes uses a purpose build statistical shape model (SSM) of the human heart. It proceeds with an application to grow the PN, where the coverage of the endocardium by the PN is controlled by four parameters. The third program generates the myocardial fibre orientation. The last two programs perform the simulation of the activation and the ECG, respectively. To understand better the effect the PN morphology has on the ECG, a virtual population study is conducted. The virtual population is generated by sampling the shape/Purkinje parameter space by a sparse grid interpolation algorithm. The sparse grid algorithm interpolates a cost function, which describes whether the ECG shows one or two R-spikes. For a given shape, this allows to describe Purkinje parameter values resulting in a single R-spike.

6.1 Motivation

As discussed in Chapter 1, the PN varies between species [7] and in particular from animals to humans. Nevertheless, the majority of morphological and physiological knowledge of the PN arises from animal studies [8,11,30]. For example, the PN growing algorithm in Section 5.2.3 was developed from observations made in calf and lamb hearts [99]. Studies of the human PN are limited to single subjects [9], and as a result it is unclear to which extent the PN may vary over a large population.

Besides the statistical investigation, the morphology of the PN could be understood from the genesis of the PN. There are two competing theories: in-growth, and out-growth hypotheses [163,164]. Both assume that the formation of the left bundle branch (LBB) and the three main branches is encoded in the genome. In the out-growth theory the remaining network is formed by advancing existing Purkinje fibre. The growth is directed such that local homogeneous activations patterns are generated. The same

objective exist for the in-growth theory, but new Purkinje fibre are recruited from the myocardium. This are grown towards the existing PN. Both theories have in common to follow and optimisation process.

The statistical observation and the analysis of the developing heart indicate that the bifurcation point and free basal area (both are described in more detail in Section 6.2.2) could depend on the heart shape. The earlier the bifurcation takes place the more of the septum is covered by the PN. Furthermore, the bifurcation point determinates the first point of myocardial activation and thereby the synchrony of the left and right ventricular activation, where the free basal area could have an influence on the total activation time of the heart.

It would be best to study the bifurcation point and the free basal area in a population. From such studies, statistical representative measurements of the PN can be obtained [99]. However, presently this investigation needs to be performed *ex vivo* [30,99], as *in vivo* images and electrophysiology measurements of the PN are insufficient to resolve the morphology of the PN. Due to the dependency on the species, the study would ideally be performed with healthy human hearts, which is ethically difficult. Consequently, an alternative to *ex vivo* study is favourable.

In this Chapter, the hypothesis that the PN morphology depends on the heart shape, is tested with a computational study. Therefore, a computational model of the PN is developed, which has four different parameters, two for the bundle bifurcation points and two for the free basal area to control the extent of the PN on the endocardium. To explore the dependencies of the four parameters on the shape, different heart shapes are taken in to consideration. This are realised by a virtual population, which is automatically generated from a SSM. The approach has the advantage of a parametrisation of the shape, which allows to explore shape dependency in a systematic way.

6.2 Methods

For the conduct of the virtual population study, an automatic pipeline for the creation of physiological heart shapes and the electrophysiology simulations is developed. The automatic pipeline begins with the construction of a heart shape from a SSM, based on 27 shape parameters. For the new shapes, a PN is generated depending on four Purkinje

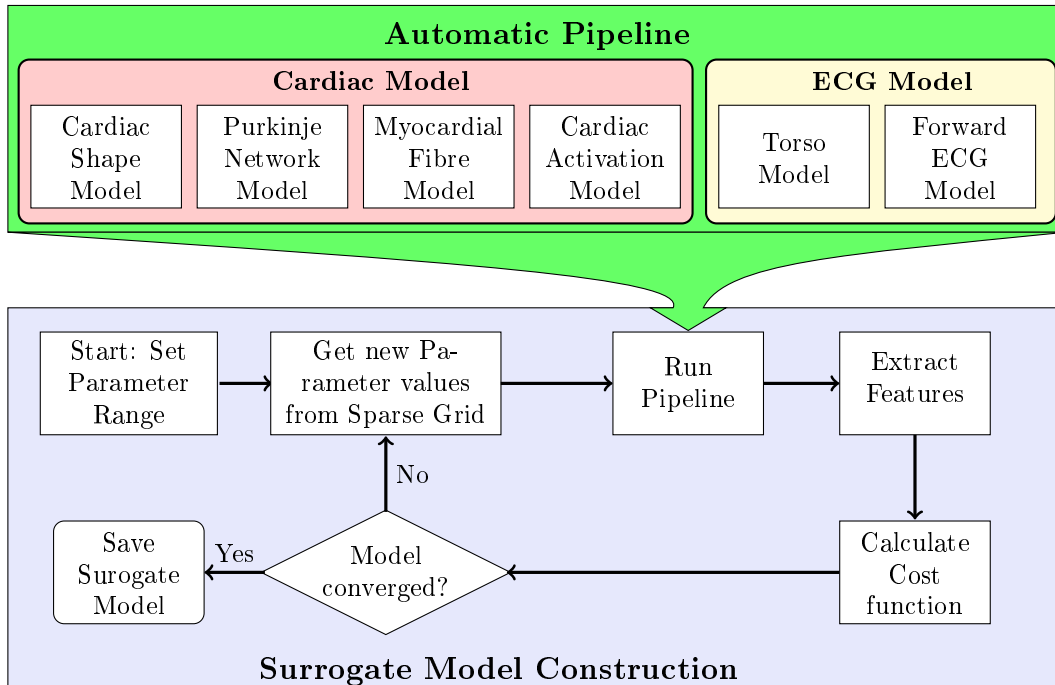


Figure 6.1: Overview of the automatic pipeline for simulation.

parameters, and the myocardial fibre orientation is generated. This is combined for the simulation of the activation time with an eikonal model. In the second part of the automatic pipeline, a forward ECG simulation is performed and all 12 leads of the ECG are extracted. An overview of the pipeline is shown in Figure 6.1.

6.2.1 Construction of a Statistical Shape Model of Cardiac Shape

To generate physiological heart shapes, the automatic pipeline uses a SSM of the heart shape. The SSM is constructed from 134 heart surface meshes obtained in the work of Hoogendoorn [68]. Point alignment and correspondents between different heart surface mesh is built with an algorithm published in [70], resulting in 2500 points for each shape. From the single value decomposition of the shape matrix, 133 modes of variation are obtained.

A subset of the eigenvectors is sufficient to achieve an acceptable reconstruction accuracy. In this chapter, the aim is an accuracy better than 6 mm (less than 3 pixel). To find the minimal set of eigenvectors needed to achieve this reconstruc-

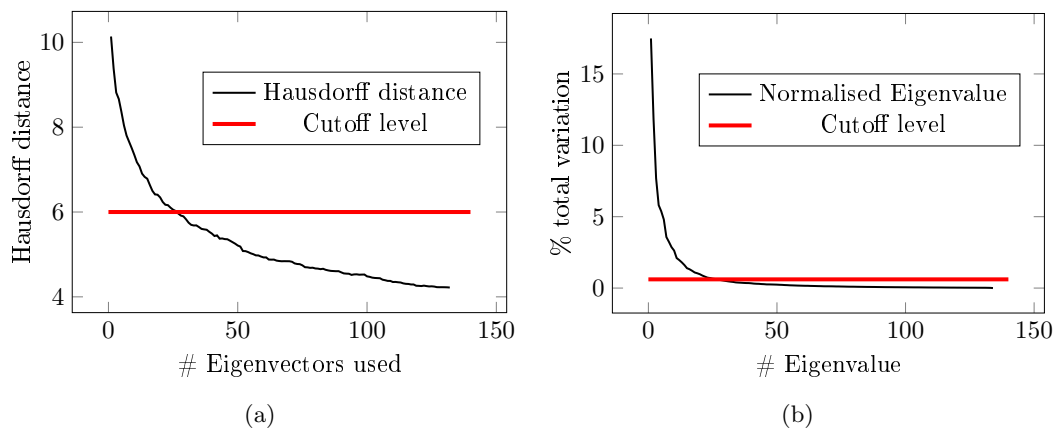


Figure 6.2: The compactness of the statistical shape model. (a) The accuracy dependency on the number of Eigenvectors used. (b) The percentage total variation explained by a given mode of variation. The red line shows the cut-off, such that an accuracy of less $6mm$ (3 pixel) is achieved.

tion accuracy, leave-one-out cross-validation is performed using n eigenvectors, where $n = 1, 2, \dots, 133$. The accuracy of the reconstruction is measured by the Hausdorff metric d_h

$$d_H(A, B) := \max(\sup_{a \in A} \inf_{b \in B} d(a, b), \sup_{b \in B} \inf_{a \in A} d(a, b)),$$

where d is the Euclidean metric. The evaluation shows, that the first 27 eigenvectors are sufficient for reconstruction (Fig. 6.2).

From the SSM, a volumetric heart mesh is required for the simulations. Therefore, the mean point distribution is used to generate a signed distance map. From the signed distance map the heart surface mesh is generated with a marching cubes algorithm. In a last step, this mesh is manually cleaned, i.e. to small triangles are merged and intersections are removed. The result is a smooth mesh with a homogeneous triangle area (Fig. 6.3), consisting of 8754 points and 17508 triangles. This mesh is later converted in a volumetric mesh.

6.2.2 The Automatic Pipeline

The automatic pipeline is formed by a series of computer programs, which are combined by a computer script. The computer programs implement the cardiac model and the ECG model, which are described in the following sections.

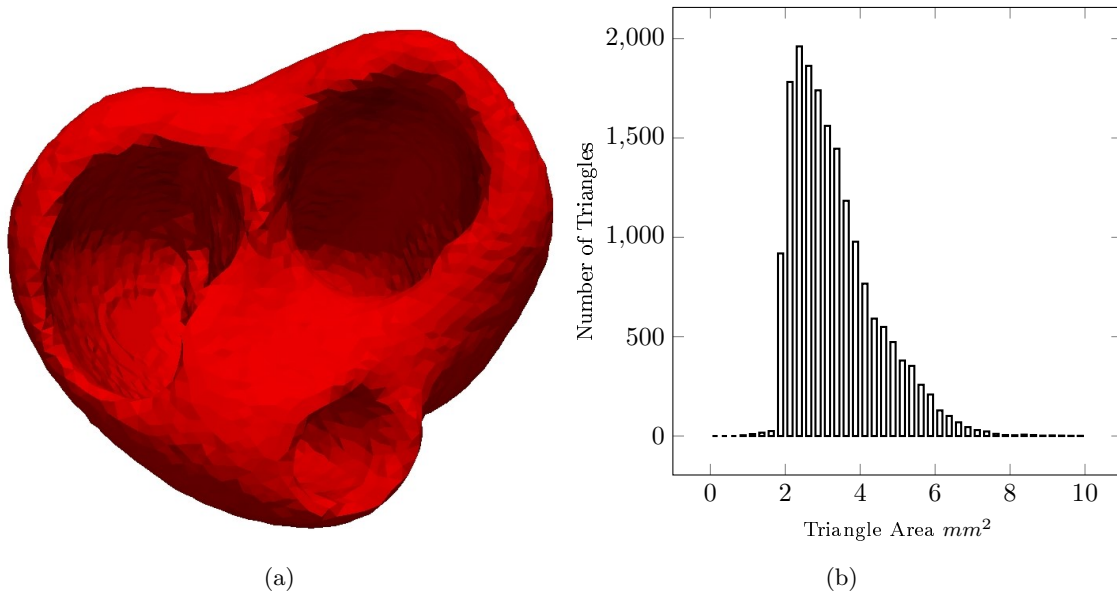


Figure 6.3: The surface reconstruction for the mean. a) mean heart surface mesh b) histogram of triangle surface

The Cardiac Model

The cardiac surface model creates a new heart surface mesh, based on 27 shape parameters. The shape parameters correspond to the weights given to each of the eigenvectors in the SSM. A new instant of the SSM is built by adding the weighted modes of variation to the mean, as described in Section 2.1.1. The new instant of the SSM consists of points only, to obtain the new heart surface mesh the mean surface mesh needs to be deformed. The deformation is based on the difference of the mean SSM and the new instance of the SSM. To interpolate the deformation on surface mesh radial basis functions are used [165]. From the surface mesh, a volumetric mesh is generated with TetGen [166].

On the surface mesh of the heart, a PN is grown. The main algorithm is the same presented in Section 5.2.3, however improvements have been made to control the coverage of the endocardium by the PN. In detail, there is one Purkinje parameter for the LBB bifurcation point and one for the right bundle branch (RBB) bifurcation point and two controlling the free basal area in left ventricle (LV) and right ventricle (RV) (Fig 6.4). The modified PN growing algorithm allows a physiological stimulation

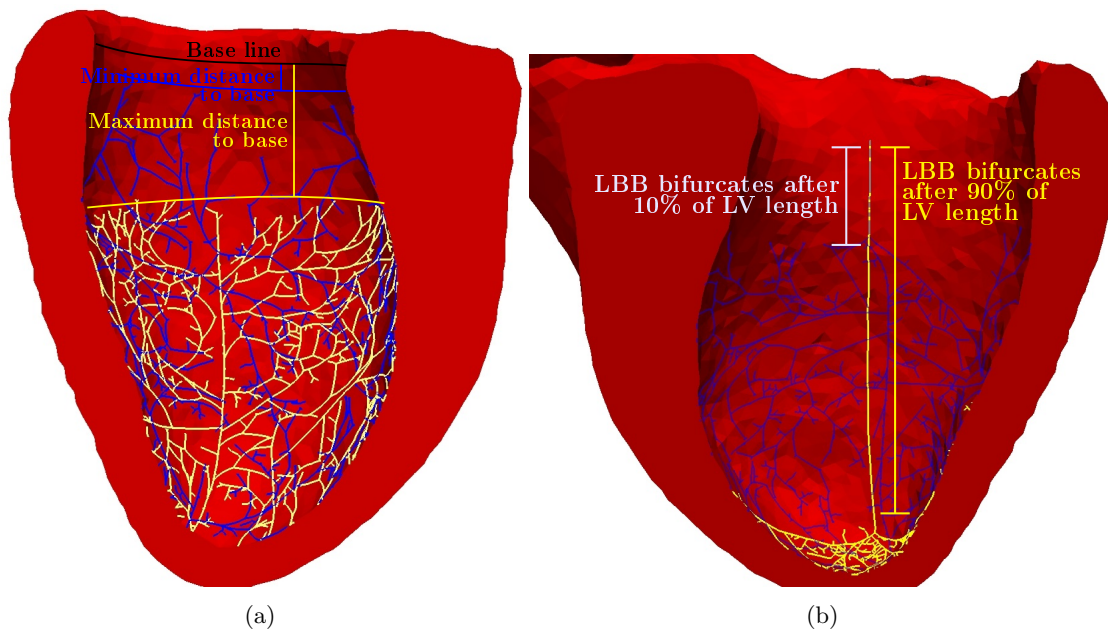


Figure 6.4: Four Purkinje parameter a) free basal area b) control of the LBB bifurcation point.

pattern of the heart, which can be adjusted for the heart shape and endocardial surface area.

For the volumetric heart mesh the myocardial fibre orientation is assigned based on a method described in [51]. In brief, the solution of the Laplace problem is used to parametrise the transmural change in fibre orientation from -41° on the endocardium to $+60^\circ$ on the epicardial surface. The implementation has been done in the *LifeV* library¹.

The activation times of the heart are estimated with the eikonal model Section 2.1.3, which is solved with the fast marching algorithm (Section 5.2.6). The activation times are converted to time-series of transmembrane potential (TMP) distributions. For each point in the volume mesh, the activation time is used as the time of upstroke (Phase 0) in the action potential (AP). The AP is sampled from a lookup table of the minimal ionic model [82]. For 150 time-steps, ranging from 0 ms to 300 ms, the TMP distribution is exported. The duration of 300 ms allows all myocytes to complete the AP, while the timestep is chosen to capture the upstroke in phase 0, which takes about 2 ms.

¹The *LifeV* (<http://www.lifev.org>) finite element library is the joint collaboration between four institutions: EPFL, Politecnico di Milano, INRIA, and Emory University.

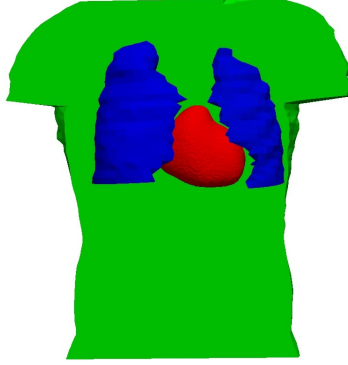


Figure 6.5: Torso (green), with lungs (blue) forming the torso domain Ω_T and the mean shape of the heart (red) Ω_H .

ECG Model

The second part of the automatic pipeline is the ECG model, which consists of the torso model and the forward ECG model.

The torso model describes the geometric modelling of the problem. In contrast to the cardiac shape model, the torso is a fixed geometry consisting of a skin and lung mesh from [167]. The third mesh is the heart surface mesh from the previous step. As the heart surface mesh has a varying shape it can be necessary to deform the lungs, to prevent intersection of lungs and heart. Therefore, a force field is created around the heart surface. Then the lungs are moved from far outside of the body to the physiological location, while the force deforms the lung surface. All surfaces are then supplied to TetGen [166] to generate a volumetric mesh, which outlines the region of lungs, heart and remaining torso (Fig. 6.5).

To simulate the ECG the extracellular potential on the torso surface generated by the heart is calculated. In Chapter 2.1.3 the equations have been developed (2.33)

$$\begin{aligned} -\nabla \cdot ((\tilde{\sigma}_i + \tilde{\sigma}_e)\nabla(\phi_T)) &= \nabla \cdot (\tilde{\sigma}_i\nabla(\varphi)) & \forall x \in \Omega_H \\ \nabla \cdot (\tilde{\sigma}_T\nabla(\phi_T)) &= 0. & \forall x \in \Omega_T \end{aligned} \quad (6.1)$$

$$\partial_n \phi_T|_{\partial\Omega_T} = 0 \quad (6.2)$$

where ϕ_T is the torso potential, φ is the TMP, and $\tilde{\sigma}_e, \tilde{\sigma}_i, \tilde{\sigma}_t$ are the extracellular, intracellular and torso conductivities. Two domains are distinguished (Fig. 6.5), $\Omega =$



Figure 6.6: The positioning of the electrodes on the torso, the colouring is according to European standard.

$\Omega_H \cup \Omega_T$ with Ω_H being the domain of the heart and Ω_T the domain of the torso without heart.

Thus, for a given TMP φ the torso potential ϕ_T can be obtained. To solve (6.1) numerically the computer program SCIRun² is used. The solution of the torso potential is obtained for all 150 time-steps of the TMP exported by the cardiac model.

The ECG is generated from the signal of different electrodes on the torso surface (Fig. 6.6). The three Einthoven leads are given by

$$I(t) = \phi_{LA} - \phi_{RA}, \quad (6.3)$$

$$II(t) = \phi_{LL} - \phi_{RA}, \quad (6.4)$$

$$III(t) = \phi_{LL} - \phi_{LA}, \quad (6.5)$$

where these are the torso potentials at the left leg (ϕ_{LL}), left arm (ϕ_{LA}), and right

²SCIRun: A Scientific Computing Problem Solving Environment, Scientific Computing and Imaging Institute (SCI), Download from: <http://www.scirun.org>

arm (ϕ_{RA}). Combination of electrodes are used for the three augmented leads

$$aV_L(t) = \phi_{LA} - 1/2(\phi_{LL} + \phi_{RA}), \quad (6.6)$$

$$aV_R(t) = \phi_{RA} - 1/2(\phi_{LA} + \phi_{RL}), \quad (6.7)$$

$$aV_F(t) = \phi_{LL} - 1/2(\phi_{LA} + \phi_{RA}). \quad (6.8)$$

To generate the precordial Wilson leads, the Wilson central terminal ϕ_{WCT} it needed. This lead is generated by connecting ϕ_{LA} , ϕ_{RA} , and ϕ_{LL} over a 5000Ω resistor each. As the sum of all currents needs to vanish one finds that

$$\phi_{WCT} = \frac{\phi_{LA} + \phi_{RA} + \phi_{LL}}{3}. \quad (6.9)$$

Thus, the six precordial Wilson leads are

$$v_1(t) = \phi_{WCT} - \phi_{V1}, \quad v_4(t) = \phi_{WCT} - \phi_{V4} \quad (6.10)$$

$$v_2(t) = \phi_{WCT} - \phi_{V2}, \quad v_4(t) = \phi_{WCT} - \phi_{V5} \quad (6.11)$$

$$v_3(t) = \phi_{WCT} - \phi_{V3}, \quad v_4(t) = \phi_{WCT} - \phi_{V6} \quad (6.12)$$

The time-series of the different leads is the output of the automatic pipeline.

6.2.3 The Surrogate Model

The aim is to construct a function, which based on the shape and Purkinje parameters predicts whether the ECG shows a double R-spike. Therefore, to any set of shape and Purkinje parameters a cost is assigned. The smaller the cost the more likely the parameter values will result in a single R-spike. As this function will be constructed from experiments, an interpolation is needed to predict the cost for not simulated parameter values. The interpolation gives the surrogate model, which is described by a hyperplane in the 32 dimensional space of cost and parameter (4 Purkinje parameters + 27 shape parameters + 1 cost).

In this chapter, the surrogate model is a piecewise linear sparse grid interpolant. The number of interpolation points of this linear interpolation is a compromise on the accuracy of the interpolation. This is necessary, since the execution of the pipeline for a single case can take more than an hour. To achieve the best compromise, a dimension-adaptive sparse grid is used. The algorithm starts with a fixed sparse grid for all

parameter dimension, which is refined in each iteration of the interpolation. If the cost of a newly refined set of parameter values can be predicted from the already constructed Surrogate model, that parameter dimension is no longer refined. The sparse grid algorithm is realised in a Matlab toolbox by A. Klimke [168,169]. The toolbox is based on [170], but has further improvements, particular for higher dimensions. This allows vectorisation of the execution of the automatic pipeline in a batch of jobs. For each set of parameter values in the batch, a new evaluation of the automatic pipeline is performed.

To evaluate the presents of a double R-spike, the lead II from the ECG is used to fit two Gauss-functions. The least-squares approximation is given by

$$g_{s_1, \mu_1, \sigma_1, s_2, \mu_2, \sigma_2}(t) = \underbrace{\frac{s_1}{\sqrt{2\sigma_1^2\pi}} \exp\left(-\frac{(x - \mu_1)^2}{2\sigma_1^2}\right)}_{N_1} + \underbrace{\frac{s_2}{\sqrt{2\sigma_2^2\pi}} \exp\left(-\frac{(x - \mu_2)^2}{2\sigma_2^2}\right)}_{N_2}. \quad (6.13)$$

For the interpolation, lets assume that $ECG(t)$ is the signal of lead II and the R-spike is at the origin $ECG(0) = \max(ECG)$. To interpolate $g(t)$ to this the L_2 error between the signal and $g(t)$ is minimized with a constrained minimisation. A regularisation terms r_1 is used to prevent both Gauss-function at the origin

$$\begin{aligned} E(s_1, \mu_1, \sigma_1, s_2, \mu_2, \sigma_2) &= \int (ECG(t) - g(t))^2 dt + \underbrace{\frac{1}{|\mu_1 - \mu_2|}}_{r_1}, s.t. \\ 0 &\geq \frac{s_2}{\sigma_2} - \frac{s_1}{\sigma_1} \\ \mu_1 &\in [-3, 3], \sigma_1 \in [10., 40], s_1 \in [-20, 200] \\ \mu_2 &\in [-50, 50], \sigma_2 \in [0.1, 50], s_2 \in [-0.1, 30] \end{aligned} \quad (6.14)$$

The constrains ensures that N_1 is the larger spike. The domain of the function E allows a negative amplitude, because the R-spike can become negative for some Purkinje parameter values.

From the fitting process six features $(s_1, \sigma_1, \mu_1, s_2, \sigma_2, \mu_2)$ are obtained, which are used to generate the cost. The cost becomes smaller if the double peaks get closer to each other and has a minimum if only one peak is detected. Therefore, the difference

between the detected amplitudes and the distance between the detected spikes is described by three functions. The first function uses the ratio between the two amplitudes of the Gauss-functions

$$f_1(\sigma_1, s_1, \sigma_2, s_2) := \text{sig}\left(100 \frac{s_2 \sigma_1}{s_1 \sigma_2}, 20\right). \quad (6.15)$$

The function becomes 0.5 or smaller if the fitting process resulted in one major amplitude and second amplitude, which can be neglect (less then 20% of the first amplitude). Here, the sigmoid function has been used

$$\text{sig}(x, x_0) = \frac{1}{1 + \exp(x_0 - x)}. \quad (6.16)$$

The second part of the cost comes from the separation of both Gauss-functions

$$f_2(\mu_1, s_1, \mu_2) := \text{sig}\left(\left(\frac{\mu_1 - \mu_2}{\mu_2}\right)^2, 2\right). \quad (6.17)$$

$$f_3 = \text{sig}(\sigma_1, 20) \quad (6.18)$$

Combining the contributions give the cost

$$\text{Cost}(s_1, \mu_1, \sigma_1, s_2, \mu_2, \sigma_2) := f_1 \cdot f_2 + 0.5 f_3 (1 - f_1). \quad (6.19)$$

This results in the cost function asymptotically approaching 1 far away from plausible configuration, which helps the sparse grid algorithm finding relevant sampling points.

After the cost is obtained, the surrogate model is updated. The process starts over with creating a new batch of parameter values. The exit criterion is that the sparse grid is evaluated to the second level. This means in each parameter dimension are not more than two refinements of the grid performed. If sufficient interpolation points have been evaluated, the surrogate model is saved and can be used to predict plausible PNs, based on the shape parameter values.

6.3 Results

The results section has three parts. In the first, the correct function of the automatic pipeline is shown, and the output of each step is visualised. The second is concerned with the behaviour of the cost function. In the last part, the actual virtual population study of the PN is conducted to constructed the surrogate model.

6.3.1 Running the Automatic Pipeline

The automatic pipeline has six steps, which produce output data and shape. This experiment visualises (Figure 6.7) the different data generated. For this illustration of the automatic pipeline, there are no preferred parameter values. Hence, for the shape parameter the mean shape is chosen. The Purkinje parameter values chosen to be in the middle of their parameter range. There is no particular reason for this choice.

6.3.2 Cost Function Behaviour

The cost function is constructed to guide the selection of the Purkinje parameter values such that simulations of the ECG result in a single R-spike, for a specific set of shape parameter values. Therefore, the cost function should be smooth and decaying if a series of Purkinje parameter values reduces the distance of the R-double spike. This experiment tests whether the cost function exhibits the behaviour, which is essential to find a correct set of Purkinje parameter values for a heart shape.

For the experiment, several different test ECG signals are constructed from two Gauss-function as they slide towards each other. The sliding of the Gauss-function represents an idealised way of a continuously better choice of Purkinje parameter, meaning a more synchronise activation of LV and RV. The Gauss-function with the larger amplitude is fixed at $\mu_1 = 0$ and a second function is added at positions in the range of $\mu_2 \in \{-40, 40\}$. For each selected μ_2 , a least-square fit with the function in (6.13) is obtained and the cost calculated. As a result, the cost can be plotted against the separation distance (Fig. 6.8).

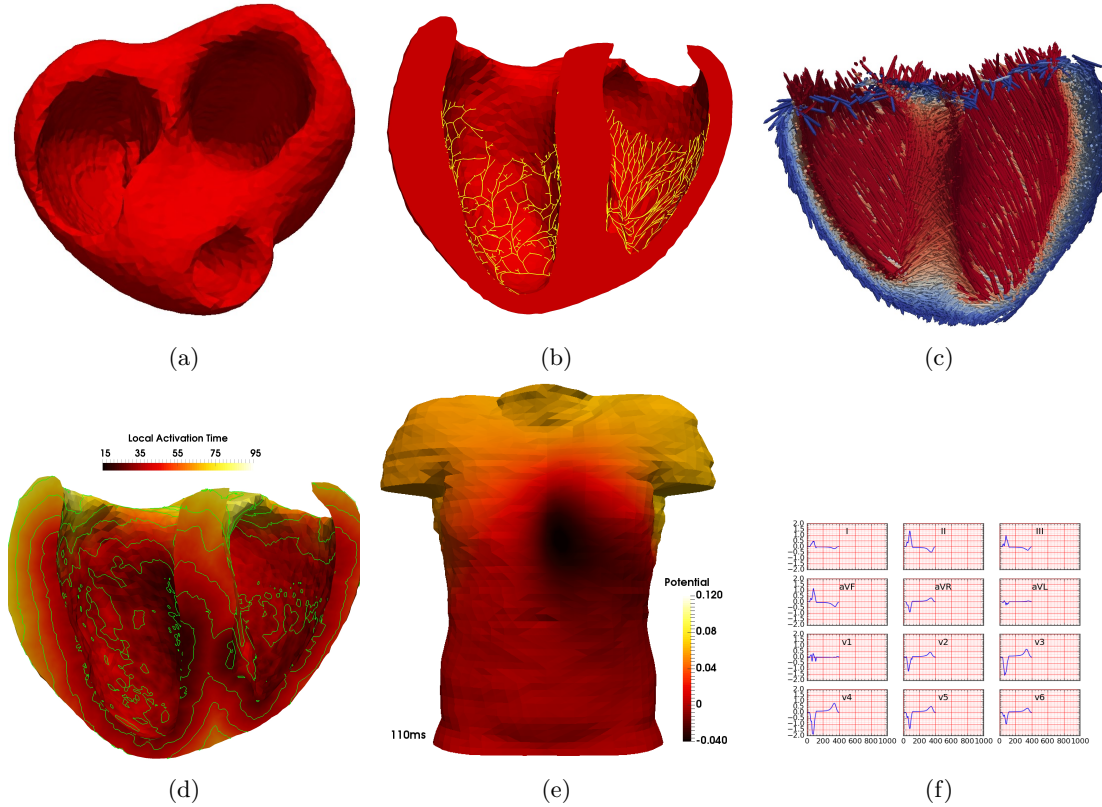


Figure 6.7: The output of each step in the automatic pipeline. a) Heart surface model b) The PN c) The myocardial fibre orientation d) Local activation times of the heart e) Volumetric torso mesh f) The resulting 12 lead ECG

6.3.3 The Surrogate Model

The surrogate model is constructed in an automatic process, which evaluates the automatic pipeline at desired parameter values. In this study, the construction of the surrogate model uses only the first mode of variation from the SSM. The reason is that tests with more modes of variation showed the problem is still computationally challenging and would need to be run in a high performance computing (HPC) facility

For the one shape parameter and four Purkinje parameter, the sparse grid algorithm generated 61 sets of parameter values. The automatic pipeline constructed the hearts shapes and PNs for the parameter values and then run the simulation. The signal of the second ECG lead was extracted and the cost (6.19) was calculated. The 61 combinations of parameter values and assigned cost form the surrogate model. The

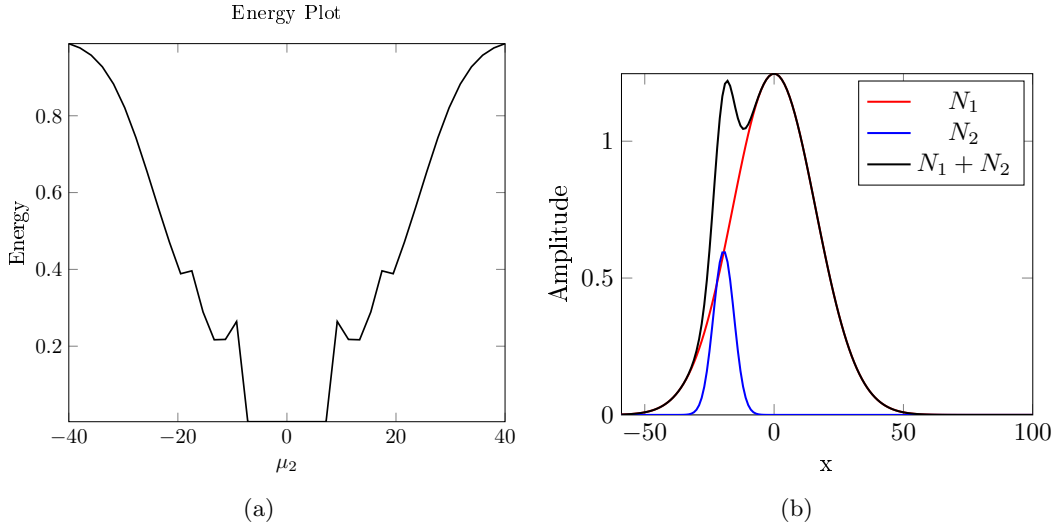


Figure 6.8: (a) Cost for different separations of the double spike, with the smallest cost for both peaks at the same position ($\mu_1 = \mu_2$). (b) Amplitude of the smaller Gauss-function (N_2) and the second Gauss-function (N_1).

complete evaluation was performed with a Dell Precision T7500 workstation and took three days.

The surrogate model was used to interpolate the cost over four different planes through the five dimensional parameter space. The first interpolation was the cost (6.19) in relation to the LBB bifurcation point and the first shape parameter (Fig. 6.9a). Then the cost function is visualised with respect to the RBB bifurcation point and the first shape parameter (Fig. 6.9b). Finally, the cost was plotted with respect to the LBB and RBB bifurcation point (Figure 6.10).

After the cost in dependency of the bifurcation points is interpolated and plotted, the same is done for free basal area (Fig. 6.11).

6.4 Discussion and Conclusions

The experiments do not confirm the hypothesis that the PN morphology depends on the heart shape, for the first mode of variation in the SSM. However, there are indications that the heart shape influence which bifurcation point position yields an ECG with a single R-spike.

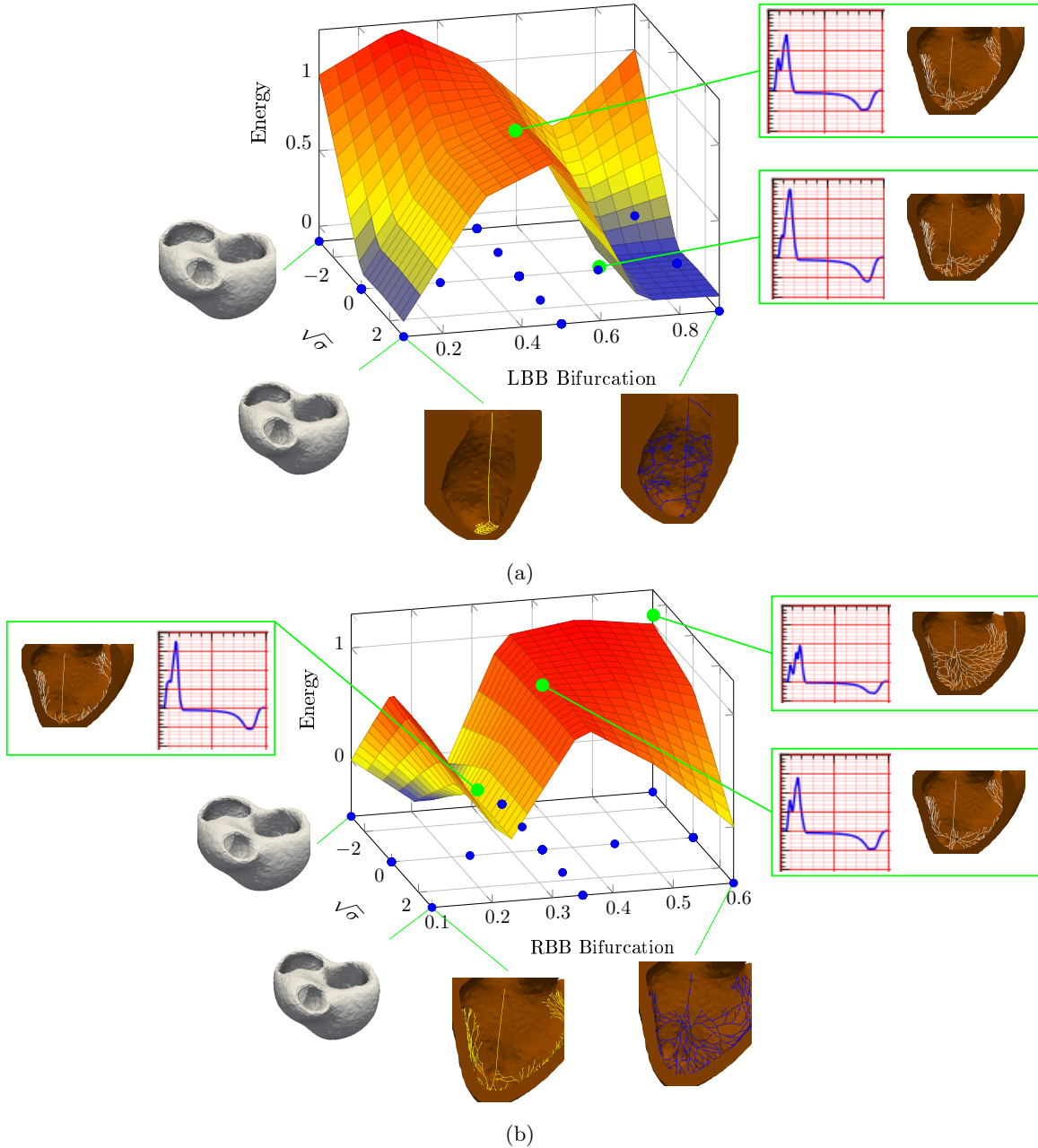


Figure 6.9: The cost as predicted from the surrogate model, where the blue circles indicate parameter values for which simulation where performed. The cost is shown in relation to the first shape parameter and (a) the LBB bifurcation point or (b) the RBB bifurcation point.

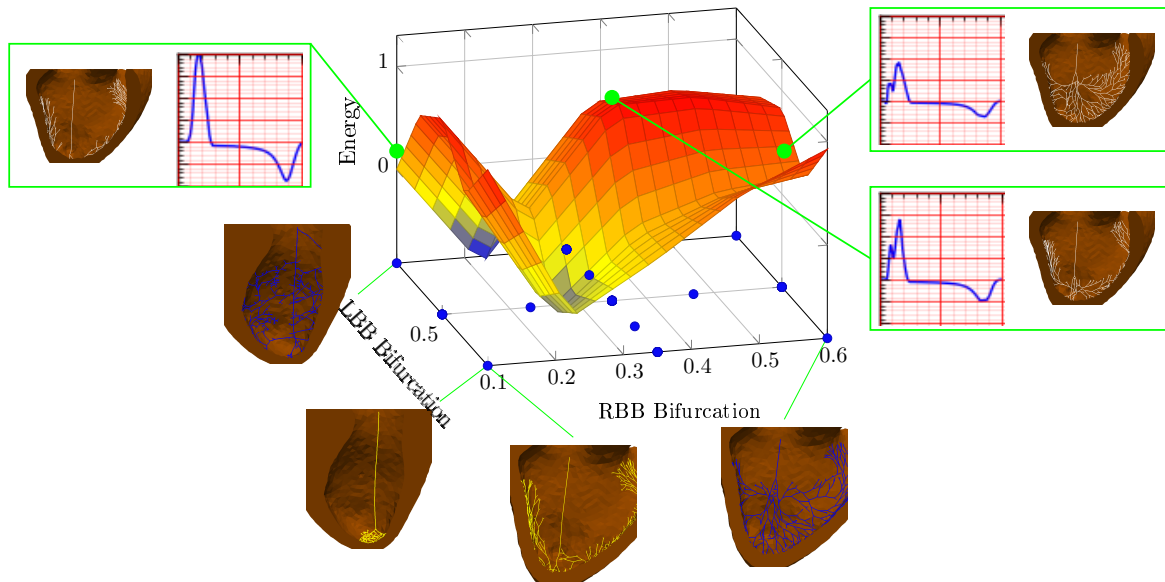


Figure 6.10: The cost function as predicted from the surrogate model, in relation to LBB bifurcation point and the RBB bifurcation point.

For the LBB bifurcation point (Fig. 6.9a) an early bifurcation near the base or a late bifurcation near the apex would be favoured by the computational model. The experiments with shape deformation in the negative direction of mode one yield an ECG with a double R-spike, for all tested bifurcation points of the LBB. This could indicate that all four Purkinje parameters need to be tuned simultaneously. Another explanation would be that shapes in negative direction of the first mode of variation are not physiological.

In case of the RBB bifurcation point the results are more conclusive and strongly favour a bifurcation point close to the apex. This observation is in agreement with literature reports that the RBB runs towards the apex and fans out from there on the right ventricular free wall [11, 171]. As for the LBB bifurcation a slight dependency on the shape is observed. However, for all shapes the same bifurcation point is favoured.

A correlation between the LBB and RBB bifurcation point is seen in Figure 6.10. As already seen in Figure 6.9 for both bundle branches exist parameter values for which the cost becomes small. However, only if both bifurcation parameters are chosen optimally an ECG with a single R-spike is produced. This was expected, because the bifurcation points determine the synchronous activation of LV and RV. It should be noted that

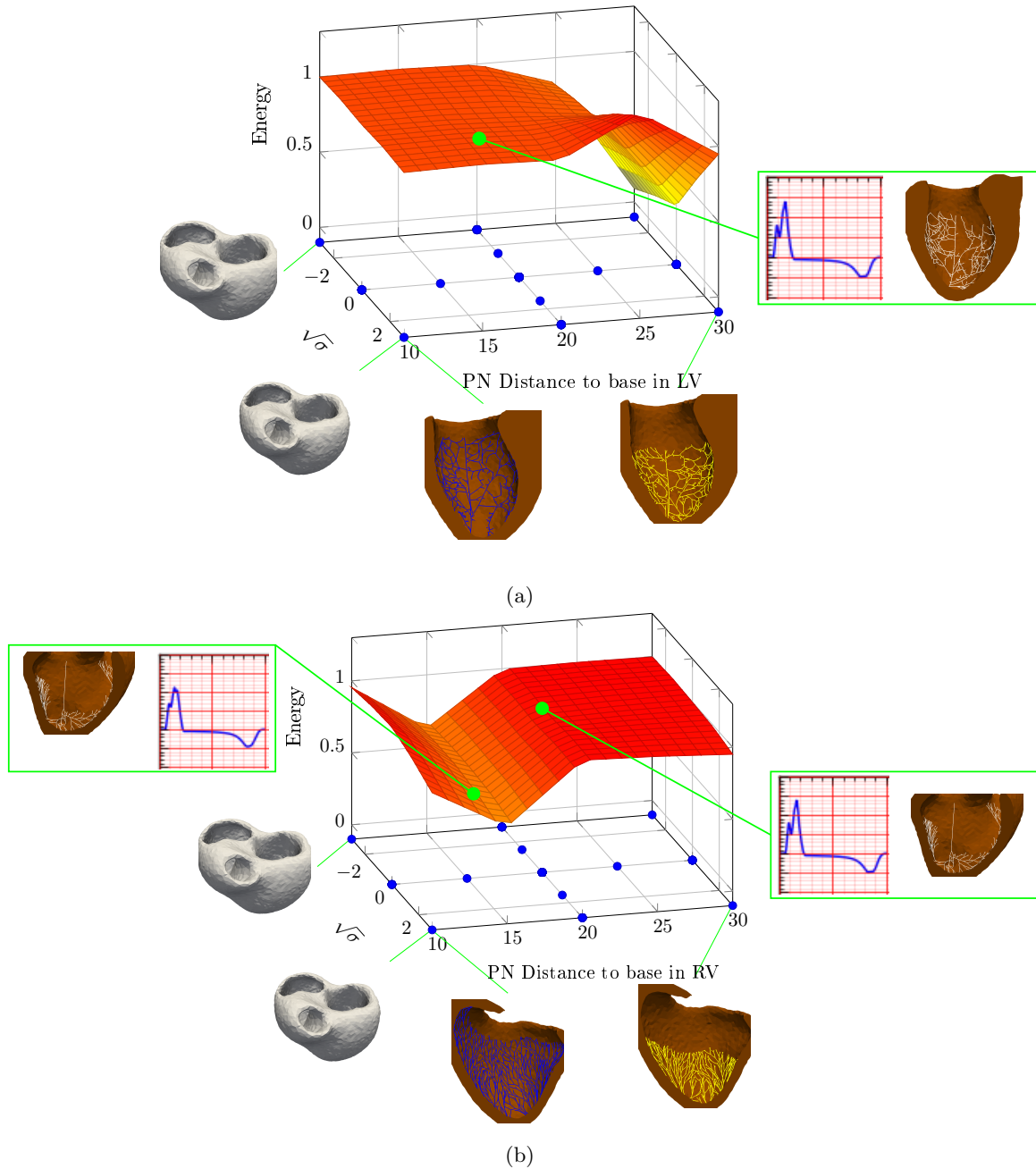


Figure 6.11: The cost function as predicted from the surrogate model, in relation to the first shape parameter and the free basal area in (a) Left Ventricle (b) Right ventricle point.

the plot is the result of a multidimensional interpolation, and in this particular example it shows negative cost, which do not exist by construction of the energy.

The free basal area in LV and RV has a smaller influence on the ECG (Fig. 6.11). With incorrectly chosen bifurcation points the free basal area in the LV has nearly no influence on the resulting ECG. Varying the free basal area in the RV can reduce the separation of the double spike. This could be related to the longer activation time in the RV if the free basal area increases. However, for all experiments the separation persisted.

In conclusion, the simulation showed that the bifurcation points of the LBB and RBB have a major impact on the correct activation sequence. Both parameters need to be tuned simultaneously until a healthy ECG is obtained. On the other hand, the simulation indicated minor importance of the free basal area for the correct formation of the ECG.

As do all studies, this study has limitations. One is the current sparse grid, which chose the middle of the parameter range as reference point. This means, that for many simulations non optimal bifurcation parameter are used. Taken the results for this study into account, it would be better if the sparse grid algorithm first searches for the correct LBB and RBB parameter and then explores other parameter dependencies. Otherwise, a bias towards the chosen bifurcation points exist. With such a technique, it might be possible to overcome the restriction to the first mode of shape variation in this study. Using a larger representation of the shape variation can give more insight in the shape dependency of the PN. Furthermore, this study uses only the lead 2 of the ECG. These means the PNs optimisation process evaluates only one of three axis.

The study shows two things, first the importance of the PN for the correct activation of the heart, and second the value of virtual population studies. Through the systematic exploration of different bifurcation points, and free basal areas in the LV and RV, it was found that the bifurcation points of the bundles need to be positioned correctly for the formation of a physiological ECG, where the free basal area is of minor importance.

The systematic exploration was possible because of the virtual population, which was generated from parametrised heart shape and Purkinje morphology. As the computational model is created from the SSM, specific heart shapes or PN can be added to the virtual population. Moreover, the virtual populations allowed to study how an unphysiological configuration of the bundle branching points in the PN affects the

ECG.

Chapter 7

Conclusion and Outlook

The aim of the thesis was to study the activation sequence of the heart for different morphologies of the human Purkinje network (PN) and heart shapes by utilising virtual populations. Following this aim, four objectives were set out in Chapter 1. In this conclusion, the objects are evaluated against the thesis.

The first objective to build an efficient electrophysiology model of the PN was addressed in Chapter 3 and 4. A numerical algorithm for the solution of the monodomain equation in the PN was developed based on the work of Vigmond and Clements [103]. In our algorithm, the mathematical formulation for the bifurcation of a Purkinje fibres in two has been changed, which improved the convergence of the algorithm with respect to the spatial discretisation. In the new formulation, linear convergence was reached and the convergence was the same for all three implementations pure central processing unit (CPU), pure graphic processing unit (GPU) and a hybrid implementation. The hybrid and pure GPU implementations reduced the computational time for simulation compared to the pure CPU substantially. The algorithm based on a pure-GPU implementation can solve the electrophysiology problem in the PN for one heart beat (400 ms) in less than 60 min on a desktop computer, while the pure CPU implementation needs nearly 6 h. With simulation times of under an hour for the electrophysiology of the PN, it becomes feasible to perform the simulation on a desktop computer, and run virtual population studies on high performance computing (HPC) facility with many GPUs.

The second objective was the development of an automatic pipeline for the generation of heart shapes and the simulation of their electrophysiology. In Chapter 6, such a pipeline was developed. One key component of that pipeline was the statistical shape model (SSM) of the heart, which was built for the pipeline such that heart shapes generated with that model have a smooth endocardial and epicardial surface, and in the triangle based surface mesh there are no intersecting triangles. The second key component was the PN growing algorithm, which offers parameters to control the left bundle branch (LBB) and right bundle branch (RBB) bifurcation point, as well as two parameter to control the basal free area of the PN in the left ventricle (LV) and right ventricle (RV). Additionally, the pipeline includes the numerical simulation of the electrocardiogram (ECG). To the best of the knowledge of the author, this is the first automatic pipeline able to simulate the ECG from shape and PN parameter values of the heart. The pipeline fulfils the requirements of the objects and provides

an important tool for conducting virtual population studies.

The third objective was to explore how false tendons (FTs) affect the heart activation pattern in LBB block condition, by the use of a virtual population. Therefore, the first computational model of a human heart that includes a FT and the papillary muscle (PM) has been developed in Chapter 5. The generation of the FT is integrated in the automatic PN growing process, and supports three different end points and two different connection types. The model has been used in a population of 70 virtual hearts to evaluate potential benefits of FTs in the pathological condition of LBB block. It was computationally shown that FT can provide a significant reduction of the total activation time in LBB block condition. Based on the literature regarding the relation of the QRS length and the cardiovascular mortality, the reductions are sufficient to reduce the cardiovascular mortality risk. Furthermore, the experiment showed that the activation time is affected by shape more than by the length of the ventricle or the attachment point of the FT. This shows the importance of virtual population studies, because there experiments are conducted for different heart shapes.

The last objective was to test the hypothesis that the extend to which the PN covers the endocardial surface depends on the heart shape. For the shape variation encoded in the first mode of variation of the SSM, the hypothesis was not confirmed. However, the study showed for the first time with a computational model of a realistic bi-ventricular heart the relevance of the correct bundle bifurcation points. Without a correctly chosen bifurcation point an ECG derived from the activation pattern will show a double R-spike. A phenomena, which is not observed in healthy physiology. Indicating that the LBB and RBB are tuned to each other, be it either by genetically encoding or by an optimisation of the activation pattern, as has been hypothesised for the PN [163, 164]. The surrogate model constructed in the thesis can be a first step towards a heuristic description of the optimal length for both bundle branches with respect to the heart shape.

Overall, the thesis has shown that virtual population studies are feasible and can augment the knowledge gained from *in vivo* or *ex vivo* studies, like the reduction in QRS duration gained by FT in LBB block condition. They are a complement to computational single-case study and offer the possibility to explore the effect of various model parameters, such as shape, on the simulation outcome. Furthermore, the thesis showed that the computational cost of virtual population study can vary greatly. While

it was possible to run simulation in excess of 700 cases for the FT model in a few days on a desktop computer, the automatic pipeline including ECG took already three days for only 62 simulations. Meaning, simple virtual population studies can be performed on the desktop computer, while more complex studies should still be performed in a HPC facility.

Consequently, the methods and models developed in this thesis have great potential for future applications and development. The automatic pipeline can be utilised to extend the surrogate model from Chapter 6 to more shape parameter. Therefore, it would need to be implemented on an HPC to be able to deal with the fast growing numbers of simulations needed when adding more shape parameter to the surrogate model. The automatic pipeline can also be combined with a segmentation tool of the heart and a registration tool which registers the segmentation to the SSM. This would offer the possibility to perform simulation for new segmented hearts.

Beside the application of the pipeline, there is potential for development. The current version of the automatic pipeline uses the eikonal model for the activation simulation, which is limited to simulation of healthy myocardial tissue. To overcome this limitation, the use of the monodomain model would be desirable. The integration of a monodomain model in the pipeline is uncomplicated, and the eikonal model can directly be replaced by the monodomain model. However, if the bidomain model should be used the uncoupling of the intracellular space and the extracellular space in the forward ECG is not possible. A fully coupled ECG forward solver or uncoupling of the heart domain and the torso domain would be required, as discussed in Section 2.3.

The use of the monodomain model for the automatic pipeline opens many new areas to explore, like ischaemia, re-entry, effect of different ionic models, or the effect of drugs on the heart, to name just a few. In ischaemic conditions the development of ventricular tachycardia (VT) can depend on the PN and the shape of the ischaemic region, which could be investigated further with the automatic pipeline. Such a study could provide additional information and the susceptibility of VT to a heart.

The FT model can be extended to incorporate more tissue, than only the Purkinje fibre. The additional tissue can have a contribution to the observed ECG. It is suspected that the additional tissue might be responsible for the reported T-wave inversions in conjunction with PN.

Chapter 8

Appendix

Table 8.1: Initial conditions used for the Stewart et al. 2009 model

V	Transmembrane potential [mV]	-75.6095
K_i	Potassium dynamics [mMol]	136.757
Na_i	Sodium dynamics [mMol]	0.80211
Ca_i	Intracellular calcium [mMol]	1.47164e-4
y	y gate	0.00780153
X_{r1}	Rapid time dependent potassium current	0.382558
X_{r2}	Rapid time dependent potassium current	0.37373
X_s	Slow time dependent potassium current	3.85284e-2
m	m gate	1.24135e-2
h	h gate	0.361832
j	j gate	0.102063
Ca_{ss}	Calcium dynamics [mMol]	5.49319e-4
d	L type Ca current d	1.21585e-4
f	L type Ca current f	0.611603
f_2	L type Ca current f_2	0.861484
f_{cass}	L-type Ca current	0.985735
s	Transient outward current s	0.925862
r	Transient outward current r	6.46602e-4
Ca_{SR}	Calcium in sarcoplasmic reticulum [mMol]	3.17519
R_{prime}	Calcium dynamics	0.851882

Bibliography

- [1] K. H. W. J. ten Tusscher and a. V. Panfilov, “Alternans and spiral breakup in a human ventricular tissue model.,” *Am. J. Physiol. Heart Circ. Physiol.*, vol. 291, no. 3, pp. H1088–100, 2006.
- [2] C. H. Luo and Y. Rudy, “A dynamic model of the cardiac ventricular action potential. I. Simulations of ionic currents and concentration changes,” *Circ. Res.*, vol. 74, no. 6, pp. 1071–1096, 1994.
- [3] D. Di Francesco and D. Noble, “A model of cardiac electrical activity incorporating ionic pumps and concentration changes.,” *Philos. Trans. R. Soc. Lond. B Biol. Sci.*, vol. 307, no. 1133, pp. 353–398, 1985.
- [4] R. Sebastian, V. Zimmerman, D. Romero, D. Sanchez-Quintana, and A. F. Frangi, “Characterization and modeling of the peripheral cardiac conduction system.,” *IEEE Trans. Med. Imaging.*, vol. 32, no. 1, pp. 45–55, 2013.
- [5] K. H. W. J. ten Tusscher and a. V. Panfilov, “Modelling of the ventricular conduction system.,” *Prog. Biophys. Mol. Biol.*, vol. 96, no. 1-3, pp. 152–70, 2008.
- [6] H. Dobrzynski, R. H. Anderson, A. Atkinson, Z. Borbas, A. D’Souza, J. F. Fraser, S. Inada, S. J. R. J. Logantha, O. Monfredi, G. M. Morris, and *et al.*, “Structure, function and clinical relevance of the cardiac conduction system, including the atrioventricular ring and outflow tract tissues.,” *Pharmacol. Ther.*, vol. 139, no. 2, pp. 260–88, 2013.
- [7] D. J. Pennisi, S. Rentschler, R. G. Gourdie, G. I. Fishman, and T. Mikawa, “Induction and patterning of the cardiac conduction system.,” *Int. J. Dev. Biol.*, vol. 46, no. 6, pp. 765–75, 2002.

- [8] A. Ansari, S. Y. Ho, and R. H. Anderson, "Distribution of the Purkinje fibres in the sheep heart.," *Anat. Rec.*, vol. 254, no. 1, pp. 92–7, 1999.
- [9] S. Tawara, *Das Reizleitungssystem des Saeugetierherzens*. Jena: von Gustav Fischer, 1906.
- [10] S. Ryu, S. Yamamoto, C. R. Andersen, K. Nakazawa, F. Miyake, and T. N. James, "Intramural Purkinje cell network of sheep ventricles as the terminal pathway of conduction system.," *Anat. Rec. (Hoboken)*, vol. 292, no. 1, pp. 12–22, 2009.
- [11] A. Atkinson, S. Inada, J. O. Li, J. and Tellez, J. Yanni, R. Sleiman, E. A. Allah, R. H. Anderson, H. Zhang, M. R. Boyett, and H. Dobrzynski, "Anatomical and molecular mapping of the left and right ventricular His-Purkinje conduction networks.," *J. Mol. Cell. Cardiol.*, vol. 51, no. 5, pp. 689–701, 2011.
- [12] J. H. Sounders, G. R. Ferrier, and G. K. Moe, "Conduction block associated with transient depolarizations induced by acetylstrophanthidin in isolated canine Purkinje fibers.," *Circ. Res.*, vol. 32, no. 5, pp. 610–617, 1973.
- [13] B. I. Sasyniuk and C. Mendez, "A mechanism for reentry in canine ventricular tissue.," *Circ. Res.*, vol. 28, no. 1, pp. 3–15, 1971.
- [14] R. F. Gilmour and M. Watanabe, "Dynamics of circus movement re-entry across canine Purkinje fibre-muscle junctions.," *J. Physiol.*, vol. 476, no. 3, pp. 473–85, 1994.
- [15] T. Desplantez, E. Dupont, N. J. Severs, and R. Weingart, "Gap junction channels and cardiac impulse propagation.," *J. Membr. Biol.*, vol. 218, no. 1-3, pp. 13–28, 2007.
- [16] P. H. Luetmer, W. D. Edwards, J. B. Seward, and A. J. Tajik, "Incidence and distribution of left ventricular false tendons: an autopsy study of 483 normal human hearts.," *J. Am. Coll. Cardiol.*, vol. 8, no. 1, pp. 179–83, 1986.
- [17] M. Kervanciolu, D. Ozba, P. Kervanciolu, E. S. Hatipolu, M. Kilin, F. Yilmaz, and M. Deniz, "Echocardiographic and morphologic examination of left ventricular false tendons in human and animal hearts.," *Clin. Anat.*, vol. 16, no. 5, pp. 389–95, 2003.

- [18] M. Deniz, M. Kiliç, and E. S. Hatipoğlu, “Morphologic study of left ventricular bands,” *Surg. Radiol. Anat.*, vol. 26, no. 3, pp. 230–4, 2004.
- [19] M. Loukas, R. G. Louis, B. Black, D. Pham, M. Fudalej, and M. Sharkees, “False tendons: an endoscopic cadaveric approach,” *Clin. Anat.*, vol. 20, no. 2, pp. 163–9, 2007.
- [20] A. K. Abdulla, A. Frustaci, J. E. Martinez, R. A. Florio, J. Somerville, and E. G. Olsen, “Echocardiography and pathology of left ventricular “false tendons” .,” *Chest*, vol. 98, no. 1, pp. 129–32, 1990.
- [21] M. H. Draper and M. Mya-Tu, “A comparison of the conduction velocity in cardiac tissues of various mammals.,” *Q. J. Exp. Physiol. Cogn. Med. Sci.*, vol. 44, no. 1, pp. 91–109, 1959.
- [22] A. Casta and W. J. Wolf, “Left ventricular bands (false tendons): echocardiographic and angiocardiographic delineation in children.,” *Am. Heart J.*, vol. 111, no. 2, pp. 321–4, 1986.
- [23] O. Abouezzeddine, M. Suleiman, T. Buescher, S. Kapa, P. a. Friedman, A. Jahangir, J. a. Mears, D. J. Ladewig, T. M. Munger, S. C. Hammill, and *et al.*, “Relevance of endocavitary structures in ablation procedures for ventricular tachycardia.,” *J. Cardiovasc. Electrophysiol.*, vol. 21, no. 3, pp. 245–54, 2010.
- [24] T. Betsuyaku, H. Muto, E. Sugiyama, A. Minoshima, and M. Sato, “False tendon-related polymorphic ventricular tachycardia.,” *Pacing. Clin. Electrophysiol.*, vol. 35, no. 12, pp. e341–4, 2012.
- [25] A. r. N. Borg, C. Miller, and M. Schmitt, “Localised myocardial scar related to left ventricular false tendons.,” *Eur. Heart J. Cardiovasc. Imaging.*, vol. 13, no. 9, p. 795, 2012.
- [26] M. Suwa, Y. Hirota, H. Nagao, M. Kino, and K. Kawamura, “Incidence of the coexistence of left ventricular false tendons and premature ventricular contractions in apparently healthy subjects,” *Circulation*, vol. 70, no. 5, pp. 793–798, 1984.
- [27] M. Suwa, Y. Hirota, K. Kaku, Y. Yoneda, A. Nakayama, K. Kawamura, and K. Doi, “Prevalence of the coexistence of left ventricular false tendons and pre-

- mature ventricular complexes in apparently healthy subjects: a prospective study in the general population.," *J. Am. Coll. Cardiol.*, vol. 12, no. 4, pp. 910–4, 1988.
- [28] J. Salazar, "Left ventricular anomalous muscle band and electrocardiographic repolarization changes.," *Pediatr. Cardiol.*, vol. 18, no. 6, pp. 434–6, 1997.
- [29] M. G. Sutton, S. Dubrey, and P. J. Oldershaw, "Muscular false tendons, aberrant left ventricular papillary musculature, and severe electrocardiographic repolarisation abnormalities: a new syndrome.," *Br. Heart J.*, vol. 71, no. 2, pp. 187–90, 1994.
- [30] R. Bordas, V. Grau, R. A. B. Burton, P. Hales, J. E. Schneider, D. Gavaghan, P. Kohl, and B. Rodriguez, "Integrated approach for the study of anatomical variability in the cardiac Purkinje system: From high resolution MRI to electrophysiology simulation," in *2010 Annu. Int. Conf. IEEE Eng. Med. Biol.*, pp. 6793–6796, IEEE, 2010.
- [31] N. Wiener and A. Rosenblueth, "The mathematical formulation of the problem of conduction of impulses in a network of connected excitable elements, specifically in cardiac muscle.," *Arch. Inst. Cardiol. Mex.*, vol. 16, no. 3, pp. 205–65, 1946.
- [32] S. Abboud, O. Berenfeld, and D. Sadeh, "Simulation of high-resolution QRS complex using a ventricular model with a fractal conduction system. Effects of ischemia on high-frequency QRS potentials.," *Circ. Res.*, vol. 68, no. 6, pp. 1751–60, 1991.
- [33] D. Durrer, R. T. van Dam, G. E. Freud, M. J. Janse, F. L. Meijler, and R. C. Arzbaecher, "Total excitation of the isolated human heart.," *Circulation*, vol. 41, no. 6, pp. 899–912, 1970.
- [34] D. D. Streeter, H. M. Spotnitz, D. P. Patel, J. Ross, and E. H. Sonnenblick, "Fiber orientation in the canine left ventricle during diastole and systole.," *Circ. Res.*, vol. 24, no. 3, pp. 339–47, 1969.
- [35] D. D. Cook and D. J. Robertson, "The generic modeling fallacy: Average biomechanical models often produce non-average results!," *J. Biomech.*, vol. 49, no. 15, 2016.

- [36] T. Lassila, M. Lange, A. R. Porrás Pérez, K. Lekadir, X. Albà, G. Piella, and A. F. Frangi, “Electrophysiology model for a human heart with ischemic scar and realistic Purkinje network,” in *International Workshop on Statistical Atlases and Computational Models of the Heart*, pp. 90–97, Springer, 2016.
- [37] A. R. Porrás, G. Piella, A. Berruezo, C. Hoogendoorn, D. Andreu, J. Fernandez-Armenta, M. Sitges, and A. F. Frangi, “Interventional endocardial motion estimation from electroanatomical mapping data : application to scar characterization,” *IEEE Trans Biomed Eng.*, vol. 60, no. 5, pp. 1217–1224, 2013.
- [38] S. Palamara, C. Vergara, D. Catanzariti, E. Faggiano, M. Centonze, C. Pangrazzi, M. Maines, and A. Quarteroni, “Computational generation of the Purkinje network driven by clinical measurements: the case of pathological propagations,” *Int. J. Num. Meth. Biomed. Eng.*, vol. 30, no. 12, pp. 1558–1577, 2014.
- [39] M. Viceconti, A. Henney, and E. Morley-Fletcher, “In silico clinical trials: How computer simulation will transform the biomedical industry. Research and technological development roadmap,” tech. rep., Avicenna Consortium, 2016.
- [40] M. Sermesant, R. Chabiniok, P. Chinchapatnam, T. Mansi, F. Billet, P. Moireau, J. M. Peyrat, K. Wong, J. Relan, K. Rhode, and *et al.*, “Patient-specific electromechanical models of the heart for the prediction of pacing acute effects in CRT: A preliminary clinical validation,” *Med. Image Anal.*, vol. 16, no. 1, pp. 201–215, 2012.
- [41] S. Palamara, C. Vergara, E. Faggiano, and F. Nobile, “An effective algorithm for the generation of patient-specific Purkinje networks in computational electrocardiology,” *J. Comput. Phys.*, vol. 283, pp. 495–517, 2015.
- [42] N. A. Trayanova and P. M. Boyle, “Advances in modeling ventricular arrhythmias: From mechanisms to the clinic,” *Wiley Interdiscip. Rev. Syst. Biol. Med.*, vol. 6, no. 2, pp. 209–224, 2014.
- [43] N. Haouchine, J. Dequidt, I. Peterlik, E. Kerrien, M. O. Berger, and S. Cotin, “Image-guided simulation of heterogeneous tissue deformation for augmented reality during hepatic surgery,” in *2013 IEEE Int. Symp. Mix. Augment. Reality, ISMAR 2013*, pp. 199–208, 2013.

- [44] C. Hoogendoorn, A. Pashaei, R. Sebastián, F. M. Sukno, O. Cámara, and A. F. Frangi, “Influence of geometric variations on LV activation times: A study on an atlas-based virtual population,” in *Lect. Notes Comput. Sci. (including Subser. Lect. Notes Artif. Intell. Lect. Notes Bioinformatics)*, vol. 6364 LNCS, pp. 242–251, 2010.
- [45] A. Pashaei, C. Hoogendoorn, R. Sebastián, D. Romero, O. Cámara, and A. F. Frangi, “Effect of scar development on fast electrophysiological models of the human heart: In-silico study on atlas-based virtual populations,” in *Proceedings of the 6th International Conference on Functional Imaging and Modeling of the Heart, FIMH’11*, (Berlin, Heidelberg), pp. 427–436, Springer-Verlag, 2011.
- [46] D. Romero, R. Sebastian, B. H. Bijnens, V. Zimmerman, P. M. Boyle, E. J. Vigmond, and A. F. Frangi, “Effects of the purkinje system and cardiac geometry on biventricular pacing: a model study.,” *Ann. Biomed. Eng.*, vol. 38, no. 4, pp. 1388–98, 2010.
- [47] M. Dupraz, S. Filippi, A. Gizzi, A. Quarteroni, and R. Ruiz-Baier, “Finite element and finite volume-element simulation of pseudo-ECGs and cardiac alternans,” *Math. Methods Appl. Sci.*, vol. 38, no. 6, 2015.
- [48] S. Niederer, E. Kerfoot, A. P. Benson, M. O. Bernabeu, O. Bernus, C. Bradley, E. M. Cherry, R. Clayton, F. H. Fenton, A. Garny, and *et al.*, “Verification of cardiac tissue electrophysiology simulators using an N-version benchmark.,” *Philos. Trans. A. Math. Phys. Eng. Sci.*, vol. 369, no. 1954, pp. 4331–51, 2011.
- [49] R. H. Clayton, “Influence of cardiac tissue anisotropy on re-entrant activation in computational models of ventricular fibrillation,” *Phys. D Nonlinear Phenom.*, vol. 238, no. 11-12, pp. 951–961, 2009.
- [50] M. Abbasi and R. Clayton, “A comparison of two models of human ventricular tissue: Simulated ischaemia and re-entry,” in *Comput. Cardiol. 2013*, pp. 385–388, 2013.
- [51] S. Rossi, T. Lassila, R. Ruiz-Baier, A. Sequeira, and A. Quarteroni, “Thermodynamically consistent orthotropic activation model capturing ventricular systolic

- wall thickening in cardiac electromechanics,” *Eur. J. Mech. - A/Solids*, vol. 48, pp. 129–142, 2013.
- [52] F. Nobile, A. Quarteroni, and R. Ruiz-Baier, “An active strain electromechanical model for cardiac tissue,” *Int. j. numer. method. biomed. eng.*, vol. 28, no. 1, pp. 52–71, 2012.
- [53] F. B. Sachse, G. Seemann, M. B. Mohr, and A. V. Holden, “Mathematical modelling of cardiac electro-mechanics: From protein to organ,” *Int. J. Bifurc. Chaos*, vol. 13, no. 12, pp. 3747–3755, 2003.
- [54] P. M. Nielsen, I. J. Le Grice, B. H. Smaill, and P. J. Hunter, “Mathematical model of geometry and fibrous structure of the heart.,” *Am. J. Physiol.*, vol. 260, no. 4 Pt 2, pp. H1365–1378, 1991.
- [55] C. Stevens, E. Remme, I. LeGrice, and P. Hunter, “Ventricular mechanics in diastole: Material parameter sensitivity,” *J. Biomech.*, vol. 36, no. 5, pp. 737–748, 2003.
- [56] F. J. Vetter and A. D. McCulloch, “Three-dimensional analysis of regional cardiac function: A model of rabbit ventricular anatomy,” 1998.
- [57] K. H. W. J. ten Tusscher, R. Hren, and A. V. Panfilov, “Organization of ventricular fibrillation in the human heart,” *Circ. Res.*, vol. 100, no. 12, pp. e87–e101, 2007.
- [58] S. Krishnamoorthi, L. E. Perotti, N. P. Borgstrom, O. A. Ajijola, A. Frid, A. V. Ponnaluri, J. N. Weiss, Z. Qu, W. S. Klug, D. B. Ennis, and A. Garfinkel, “Simulation methods and validation criteria for modeling cardiac ventricular electrophysiology,” *PLoS One*, vol. 9, no. 12, p. e114494, 2014.
- [59] M. Plotkowiak, B. Rodriguez, G. Plank, J. E. Schneider, D. Gavaghan, P. Kohl, and V. Grau, *High performance computer simulations of cardiac electrical function based on high resolution MRI datasets*, pp. 571–580. Berlin, Heidelberg: Springer Berlin Heidelberg, 2008.
- [60] M. Pop, M. Sermesant, D. Lepiller, M. V. Truong, E. R. McVeigh, E. Crystal, A. Dick, H. Delingette, N. Ayache, and G. A. Wright, “Fusion of optical imaging

- and MRI for the evaluation and adjustment of macroscopic models of cardiac electrophysiology: A feasibility study,” *Med. Image Anal.*, vol. 13, no. 2, pp. 370–380, 2009.
- [61] M. Jolley, J. Stinstra, S. Pieper, R. MacLeod, D. H. Brooks, F. Cecchin, and J. K. Triedman, “A computer modeling tool for comparing novel ICD electrode orientations in children and adults,” *Hear. Rhythm.*, vol. 5, no. 4, pp. 565–572, 2008.
- [62] Y. Wang, D. R. Haynor, and Y. Kim, “An investigation of the importance of myocardial anisotropy in finite-element modeling of the heart: methodology and application to the estimation of defibrillation efficacy,” *IEEE Trans. Biomed. Eng.*, vol. 48, no. 12, pp. 1377–1389, 2001.
- [63] M. S. Aslan, A. Shalaby, H. Abdelmunim, and A. A. Farag, “Probabilistic shape-based segmentation method using level sets,” *Comput. Vision, IET*, vol. 8, no. 3, pp. 182–194, 2014.
- [64] Z. Pan and J. Lu, “A Bayes-based region-growing algorithm for medical image segmentation,” *Comput. Sci. Eng.*, vol. 9, no. 4, pp. 32–38, 2007.
- [65] X. Chen, J. K. Udupa, U. Bagci, Y. Zhuge, and J. Yao, “Medical image segmentation by combining graph cuts and oriented active appearance models,” *IEEE Trans. Image Process.*, vol. 21, no. 4, pp. 2035–46, 2012.
- [66] W. E. Lorensen and H. E. Cline, “Marching cubes: A high resolution 3D surface construction algorithm,” in *Proc. 14th Annu. Conf. Comput. Graph. Interact. Tech. - SIGGRAPH '87*, vol. 21, pp. 163–169, 1987.
- [67] T. F. F. Cootes, C. J. Taylor, D. H. Cooper, and J. Graham, “Active shape models - Their training and applications,” *Comput. Vis. Image Underst.*, vol. 61, no. 1, pp. 38–59, 1995.
- [68] C. Hoogendoorn, N. Duchateau, D. Sánchez-Quintana, T. Whitmarsh, F. M. Sukno, M. De Craene, K. Lekadir, and A. F. Frangi, “A high-resolution atlas and statistical model of the human heart from multislice CT,” *IEEE Trans. Med. Imaging.*, vol. 32, no. 1, pp. 28–44, 2013.

- [69] J. C. Gower, "Generalized procrustes analysis," *Psychometrika*, vol. 40, no. 1, pp. 33–51, 1975.
- [70] N. Ravikumar, A. Gooya, S. Cimen, A. F. Frangi, and Z. A. Taylo, *A multi-resolution T-mixture model approach to robust group-wise alignment of shapes*, pp. 142–149. Cham: Springer International Publishing, 2016.
- [71] A. a. Young and A. F. Frangi, "Computational cardiac atlases: from patient to population and back.," *Exp. Physiol.*, vol. 94, no. 5, pp. 578–96, 2009.
- [72] H. Lombaert, J.-M. Peyrat, P. Croisille, S. Rapacchi, L. Fanton, F. Cheriet, P. Clarysse, I. Magnin, H. Delingette, and N. Ayache, "Human atlas of the cardiac fiber architecture: study on a healthy population.," *IEEE Trans. Med. Imaging*, vol. 31, no. 7, pp. 1436–47, 2012.
- [73] M. D. Cerqueira, N. J. Weissman, V. Dilsizian, A. K. Jacobs, S. Kaul, W. K. Laskey, D. J. Pennell, J. a. Rumberger, T. Ryan, and M. S. Verani, "Standardized myocardial segmentation and nomenclature for tomographic imaging of the heart. A statement for healthcare professionals from the cardiac imaging committee of the council on clinical cardiology of the american heart association," *Int. J. Cardiovasc. Imaging.*, vol. 18, no. 1, pp. 539–42, 2002.
- [74] K. Lekadir, M. Lange, V. A. Zimmer, C. Hoogendoorn, and A. F. Frangi, "Statistically-driven 3D fiber reconstruction and denoising from multi-slice cardiac DTI using a Markov random field model," *Med. Image Anal.*, vol. 27, pp. 105–116, 2016.
- [75] J. Sundnes, L. G. Terju, C. Xing, B. F. Nielsen, K.-A. Mardal, and A. Tveito, *Computing the electrical activity in the heart*. Springer, 2006.
- [76] E. J. Vigmond, F. Vadakkumpadan, V. Gurev, H. Arevalo, M. Deo, G. Plank, and N. Trayanova, "Towards predictive modelling of the electrophysiology of the heart.," *Exp. Physiol.*, vol. 94, no. 5, pp. 563–77, 2009.
- [77] G. T. Lines, M. L. Buist, P. Grottum, A. J. Pullan, J. Sundnes, and A. Tveito, "Mathematical models and numerical methods for the forward problem in cardiac electrophysiology," *Comput. Vis. Sci.*, vol. 5, no. 4, pp. 215–239, 2002.

- [78] J. Keener and J. Sneyd, *Mathematical physiology I: Cellular physiology*, vol. 8/1 of *Interdisciplinary Applied Mathematics*. New York, NY: Springer New York, 2nd ed., 2009.
- [79] P. Colli Franzone and L. F. Pavarino, “A parallel solver for reaction-diffusion systems in computational electrocardiology,” *Math. Models Methods Appl. Sci.*, vol. 14, no. 06, pp. 883–911, 2004.
- [80] R. H. Clayton, O. Bernus, E. M. Cherry, H. Dierckx, F. H. Fenton, L. Mirabella, a. V. Panfilov, F. B. Sachse, G. Seemann, and H. Zhang, “Models of cardiac tissue electrophysiology: Progress, challenges and open questions,” *Prog. Biophys. Mol. Biol.*, vol. 104, no. 1-3, pp. 22–48, 2011.
- [81] A. L. Hodgkin and A. F. Huxley, “A quantitative description of membrane current and its application to conduction and excitation in nerve,” *J. Physiol.*, vol. 117, no. 4, pp. 500–544, 1952.
- [82] A. Bueno-Orovio, E. M. Cherry, and F. H. Fenton, “Minimal model for human ventricular action potentials in tissue.,” *J. Theor. Biol.*, vol. 253, no. 3, pp. 544–60, 2008.
- [83] K. H. W. J. ten Tusscher, D. Noble, P. J. Noble, and a. V. Panfilov, “A model for human ventricular tissue.,” *Am. J. Physiol. Heart Circ. Physiol.*, vol. 286, no. 4, pp. H1573–89, 2004.
- [84] C. H. Luo and Y. Rudy, “A dynamic model of the cardiac ventricular action potential. I. Simulations of ionic currents and concentration changes.,” *Circ. Res.*, vol. 74, no. 6, pp. 1071–1096, 1994.
- [85] D. Noble, “A modification of the Hodgkin–Huxley equations applicable to Purkinje fibre action and pace-maker potentials.,” *J. Physiol.*, vol. 160, pp. 317–52, 1962.
- [86] P. Stewart, O. V. Aslanidi, D. Noble, P. J. Noble, M. R. Boyett, and H. Zhang, “Mathematical models of the electrical action potential of Purkinje fibre cells.,” *Philos. Trans. A. Math. Phys. Eng. Sci.*, vol. 367, no. 1896, pp. 2225–55, 2009.

-
- [87] R. H. Clayton and a. V. Panfilov, “A guide to modelling cardiac electrical activity in anatomically detailed ventricles.,” *Prog. Biophys. Mol. Biol.*, vol. 96, no. 1-3, pp. 19–43, 2008.
- [88] K. H. W. J. ten Tusscher and P. a. V., “Modelling of the ventricular conduction system,” *Prog. Biophys. Mol. Biol.*, vol. 96, no. 13, pp. 152 – 170, 2008.
- [89] J. P. Keener and J. Sneyd, *Mathematical physiology*. New York: Springer, 1998.
- [90] P. C. Franzone and L. Guerri, “Spreading of excitation in 3-D models of the anisotropic cardiac tissue. I. Validation of the eikonal model.,” *Math. Biosci.*, vol. 113, no. 2, pp. 145–209, 1993.
- [91] P. Colli Franzone, L. Guerri, M. Pennacchio, and B. Taccardi, “Spreading excitation in 3-d models of the anisotropic cardiac tissue, ii. effects of the fiber architecture and ventricular geometry.,” *Math. Biosci.*, vol. 2, no. 147, pp. 131–171, 1998.
- [92] M. Sermesant, E. Konukoğu, H. Delingette, Y. Coudire, P. Chinchapatnam, K. Rhode, R. Razavi, and N. Ayache, “An anisotropic multi-front fast marching method for real-time simulation of cardiac electrophysiology,” in *Functional Imaging and Modeling of the Heart* (F. B. Sachse and G. Seemann, eds.), vol. 4466 of *Lecture Notes in Computer Science*, pp. 160–169, Springer Berlin Heidelberg, 2007.
- [93] A. Pashaei, D. Romero, R. Sebastian, O. Camara, and A. F. Frangi, “Comparison of phenomenological and biophysical cardiac models coupled with heterogenous structures for prediction of electrical activation sequence,” in *Comput. Cardiol.*, 2010, pp. 871–874, 2010.
- [94] J. P. Keener, “An eikonal-curvature equation for action potential propagation in myocardium,” *J Math Biol*, vol. 29, no. 7, pp. 629–651, 1991.
- [95] C. J. Clements and E. J. Vigmond, “Construction of a cardiac conduction system subject to extracellular stimulation,” in *Conf. Proc. IEEE Eng. Med. Biol. Soc.*, pp. 4235–4238, IEEE, 2005.

-
- [96] a. E. Pollard and R. C. Barr, “The construction of an anatomically based model of the human ventricular conduction system,” *IEEE Trans. Biomed. Eng.*, vol. 37, no. 12, pp. 1173–1185, 1990.
- [97] O. Berenfeld and J. Jalife, “Purkinje-muscle reentry as a mechanism of polymorphic ventricular arrhythmias in a 3-dimensional model of the ventricles,” *Circ. Res.*, vol. 82, no. 10, pp. 1063–1077, 1998.
- [98] T. Ijiri, T. Ashihara, T. Yamaguchi, K. Takayama, T. Igarashi, T. Shimada, T. Namba, R. Haraguchi, and K. Nakazawa, “A procedural method for modeling the purkinje fibers of the heart.,” *J. Physiol. Sci.*, vol. 58, no. 7, pp. 481–6, 2008.
- [99] R. Sebastian, V. Zimmerman, D. Romero, and A. F. Frangi, “Construction of a computational anatomical model of the peripheral cardiac conduction system,” *IEEE Trans. Biomed. Eng.*, vol. 58, no. 12, pp. 3479–82, 2011.
- [100] F. Sahli Costabal, D. E. Hurtado, and E. Kuhl, “Generating Purkinje networks in the human heart.,” *J. Biomech.*, vol. 49, no. 12, pp. 2455–2465, 2015.
- [101] A. Pashaei, D. Romero, R. Sebastian, O. Camara, and A. F. Frangi, “Fast multiscale modeling of cardiac electrophysiology including Purkinje system.,” *IEEE Trans. Biomed. Eng.*, vol. 58, no. 10, pp. 2956–60, 2011.
- [102] R. M. Bordas, K. Gillow, D. Gavaghan, B. Rodriguez, and D. Kay, “A bidomain model of the ventricular specialized conduction system of the heart,” *SIAM J. Appl. Math.*, vol. 72, no. 5, pp. 1618–1643, 2012.
- [103] E. J. Vigmond and C. Clements, “Construction of a computer model to investigate sawtooth effects in the Purkinje system.,” *IEEE. Trans. Biomed. Eng.*, vol. 54, no. 3, pp. 389–99, 2007.
- [104] M. Boulakia, S. Cazeau, M. A. Fernández, J. Gerbeau, and N. Zenzemi, “Mathematical modeling of electrocardiograms: A numerical study,” *Ann. Biomed. Eng.*, vol. 38, no. 3, pp. 1071–1097, 2010.
- [105] M. Lange, S. Palamara, T. Lassila, C. Vergara, A. Quarteroni, and A. F. Frangi, “Efficient numerical schemes for computing cardiac electrical activation over realistic purkinje networks: method and verification,” *In: H. van Assen, P. Boven-*

- deerd, T. Delhaas (Eds.) *Proc. 8th Int. Conf. Functional Imag. Model. Heart (FIMH 2015)*, June 25–27, Maastricht, 2015.
- [106] M. Lange, S. Palamara, T. Lassila, C. Vergara, A. Quarteroni, and A. F. Frangi, “Improved hybrid/GPU algorithm for solving cardiac electrophysiology problems on Purkinje networks,” *Int. j. numer. method. biomed. eng.*, pp. n/a–n/a, 2016.
- [107] L. L. Cooper, K. E. Odening, M.-S. Hwang, L. Chaves, L. Schofield, C. A. Taylor, A. S. Gemignani, G. F. Mitchell, J. R. Forder, B.-R. Choi, and G. Koren, “Electromechanical and structural alterations in the aging rabbit heart and aorta,” *Am. J. Physiol. Heart Circ. Physiol.*, vol. 302, no. 8, pp. H1625–H1635, 2012.
- [108] P. a. Boyden, C. Barbaiya, T. Lee, and H. E. D. J. Ter Keurs, “Nonuniform Ca²⁺ transients in arrhythmogenic Purkinje cells that survive in the infarcted canine heart,” *Cardiovasc. Res.*, vol. 57, pp. 681–693, 2003.
- [109] A. Nogami, “Purkinje-related arrhythmias part I: Monomorphic ventricular tachycardias,” *Pacing Clin. Electrophysiol.*, vol. 34, no. 5, pp. 624–650, 2011.
- [110] F. Bogun, E. Good, S. Reich, D. Elmouchi, P. Igic, D. Tschopp, S. Dey, A. Wimmer, K. Jongnarangsin, H. Oral, and *et al.*, “Role of Purkinje fibers in post-infarction ventricular tachycardia,” *J. Am. Coll. Cardiol.*, vol. 48, no. 12, pp. 2500–2507, 2006.
- [111] C. Vergara, M. Lange, S. Palamara, T. Lassila, A. F. Frangi, and A. Quarteroni, “A coupled 3D1D numerical monodomain solver for cardiac electrical activation in the myocardium with detailed Purkinje network,” *J. Comput. Phys.*, vol. 308, pp. 218–238, 2016.
- [112] R. Artebrant, A. Tveito, and G. T. Lines, “A method for analyzing the stability of the resting state for a model of pacemaker cells surrounded by stable cells,” *Math. Biosci. Eng.*, vol. 7, no. 3, pp. 505–526, 2010.
- [113] T. Stankovicová, V. Bitó, F. Heinzl, K. Mubagwa, and K. R. Sipido, “Isolation and morphology of single Purkinje cells from the porcine heart,” *Gen. Physiol. Biophys.*, vol. 22, no. 3, pp. 329–340, 2003.

-
- [114] P. Colli Franzone, L. F. Pavarino, and S. Scacchi, *Mathematical cardiac electrophysiology*, vol. 13 of *Modeling, Simulation & Applications*. Springer Cham Heidelberg New York Dordrecht London, 2014.
- [115] C. Vergara, M. Lange, S. Palamara, T. Lassila, A. F. Frangi, and A. Quarteroni, “A coupled 3D-1D numerical monodomain solver for cardiac electrical activation in the myocardium with detailed Purkinje network,” *J. Comput. Phys.*, vol. 308, pp. 218–238, 2016.
- [116] M. Naumov, “Parallel solution of sparse triangular linear systems in the preconditioned iterative methods on the GPU,” Tech. Rep. NVR-2011-001, NVIDIA, 2011.
- [117] A. Tveito and G. T. Lines, “A condition for setting off ectopic waves in computational models of excitable cells,” *Math. Biosci.*, vol. 213, no. 2, pp. 141–50, 2008.
- [118] J. Rinzel and J. B. Keller, “Traveling wave solutions of a nerve conduction equation,” *Biophys. J.*, vol. 13, no. 12, pp. 1313–37, 1973.
- [119] H. McKean Jr., “Nagumo’s equation,” *Adv. Math.*, vol. 4, no. 3, pp. 209–223, 1970.
- [120] A. Mena and J. F. Rodriguez, “Using graphic processor units for the study of electric propagation in realistic heart models,” in *Computing in Cardiology (cinc)*, vol. 39, pp. 37–40, 2012.
- [121] B. M. Rocha, F. O. Campos, G. Plank, R. W. Dos Santos, M. Liebmann, and G. Haase, “Simulations of the electrical activity in the heart with graphic processing units,” in *Lect. Notes Comput. Sci. (including Subser. Lect. Notes Artif. Intell. Lect. Notes Bioinformatics)*, vol. 6067 LNCS, pp. 439–448, 2010.
- [122] E. J. Vigmond, P. M. Boyle, L. J. Leon, and G. Plank, “Near-real-time simulations of bioelectric activity in small mammalian hearts using graphical processing units,” in *Proc. 31st Annu. Int. Conf. IEEE Eng. Med. Biol. Soc. Eng. Futur. Biomed. EMBC 2009*, pp. 3290–3293, 2009.

- [123] A. Mahajan, Y. Shiferaw, D. Sato, A. Baher, R. Olcese, L.-H. Xie, M.-J. Yang, P.-S. Chen, J. G. Restrepo, A. Karma, and *et al.*, “A rabbit ventricular action potential model replicating cardiac dynamics at rapid heart rates.,” *Biophys. J.*, vol. 94, no. 2, pp. 392–410, 2008.
- [124] A. Neic, M. Liebmann, E. Hoetzel, L. Mitchell, E. J. Vigmond, G. Haase, and G. Plank, “Accelerating cardiac bidomain simulations using graphics processing units.,” *IEEE Trans. Biomed. Eng.*, vol. 59, no. 8, pp. 2281–90, 2012.
- [125] M. Lange, L. Y. Di Marco, K. Lekadir, T. Lassila, and A. F. Frangi, “Protective role of false tendon in subjects with left bundle branch block: A virtual population study,” *PLOS ONE*, vol. 11, no. 1, pp. 1–23, 2016.
- [126] M. R. Bhatt, C. E. Alfonso, A. M. Bhatt, S. Lee, A. C. Ferreira, T. Salerno, and E. de Marchena, “Effects and mechanisms of left ventricular false tendons on functional mitral regurgitation in patients with severe cardiomyopathy.,” *J. Thorac. Cardiovasc. Surg.*, vol. 138, no. 5, pp. 1123–8, 2009.
- [127] S. H. Lee, H. M. Ryu, J. H. Lee, H. Lee, S. H. Park, M. H. Bae, and D. H. Yang, “A case of an anomalous hypertrophied muscle band in the left ventricle.,” *J. Cardiovasc. Ultrasound.*, vol. 20, no. 2, pp. 97–9, 2012.
- [128] J. Ker, “Sub aortic tendon induced ST segment elevation—a new echo electrocardiographic phenomenon?,” *Cardiovasc. Ultrasound.*, vol. 7, p. 13, 2009.
- [129] S. Philip, K. M. Cherian, M.-h. Wu, and H.-c. Lue, “Left ventricular false tendons: echocardiographic, morphologic, and histopathologic studies and review of the literature.,” *Pediatr. Neonatol.*, vol. 52, no. 5, pp. 279–86, 2011.
- [130] M. Loukas, Z. Klaassen, R. S. Tubbs, T. Derderian, D. Paling, D. Chow, S. Patel, and R. H. Anderson, “Anatomical observations of the moderator band.,” *Clin. Anat.*, vol. 23, no. 4, pp. 443–50, 2010.
- [131] P. Haataja, K. Nikus, M. Kahonen, H. Huhtala, T. Nieminen, A. Jula, A. Reunanen, V. Salomaa, S. Sclarovsky, S. Nieminen, and E. M., “Prevalence of ventricular conduction blocks in the resting electrocardiogram in a general population: The health 2000 survey,” *Int. J. Cardiol.*, vol. 167, no. 5, pp. 1953 – 1960, 2013.

- [132] A. Badheka, V. Singh, N. J. Patel, A. Deshmukh, N. Shah, A. Chothani, K. Mehta, P. Grover, G. T. Savani, S. Gupta, and *et al.*, “Qrs duration on electrocardiography and cardiovascular mortality (from the national health and nutrition examination surveyiii),” *Am. J. Cardiol.*, vol. 112, no. 5, pp. 671–677, 2013.
- [133] M. Brignole, A. Auricchio, G. Baron-Esquivias, P. Bordachar, G. Boriani, O.-A. Breithardt, J. Cleland, J.-C. Deharo, V. Delgado, P. M. Elliott, and *et al.*, “2013 esc guidelines on cardiac pacing and cardiac resynchronization therapy,” *Eur. Heart J.*, vol. 34, no. 29, pp. 2281–2329, 2013.
- [134] A. M. Russo, R. F. Stainback, S. R. Bailey, A. E. Epstein, P. A. Heidenreich, M. Jessup, S. Kapa, M. S. Kremers, B. D. Lindsay, and L. W. Stevenson, “Accf/hrs/aha/ase/hfsa/scai/scct/scmr 2013 appropriate use criteria for implantable cardioverter-defibrillators and cardiac resynchronization therapy: A report of the american college of cardiology foundation appropriate use criteria task force, heart rhythm society, american heart association, american society of echocardiography, heart failure society of america, society for cardiovascular angiography and interventions, society of cardiovascular computed tomography, and society for cardiovascular magnetic resonance,” *J. Am. Coll. Cardiol.*, vol. 61, no. 12, pp. 1318–1368, 2013.
- [135] L. M. Gerlis, H. M. Wright, N. Wilson, F. Erzenigin, and D. F. Dickinson, “Left ventricular bands. A normal anatomical feature.,” *Br. Heart. J.*, vol. 52, no. 6, pp. 641–7, 1984.
- [136] M. T. Boyd, J. B. Seward, A. Jamil Tajik, and W. D. Edwards, “Frequency and location of prominent left ventricular trabeculations at autopsy in 474 normal human hearts: Implications for evaluation of mural thrombi by two-dimensional echocardiography,” *J. Am. Coll. Cardiol.*, vol. 9, no. 2, pp. 323–326, 1987.
- [137] M. Grzybiak, D. Lotkowski, and D. Kozowski, “False tendons in the left ventricle of the heart in humans during pre- and postnatal periods.,” *Folia. Morphol. (Warsz)*, vol. 55, no. 2, pp. 89–99, 1996.
- [138] M. Okamoto, S. Nagata, Y. D. Park, Y. Masuda, S. Beppu, C. Yutani, H. Sakakibara, and Y. Nimura, “[Visualization of the false tendon in the left ventricle

- with echocardiography and its clinical significance (author's transl)].," *J. Cardiogr.*, vol. 11, no. 1, pp. 265–70, 1981.
- [139] T. Nishimura, M. Kondo, T. Shimada, Y. Shimono, and N. Mukohyama, "[Echocardiographic features of false tendons: with special reference to phonocardiographic significance (author's transl)].," *J. Cardiogr.*, vol. 11, no. 1, pp. 253–63, 1981.
- [140] L. W. Perry, R. N. Ruckman, S. R. Shapiro, K. S. Kuehl, F. M. Galioto, and L. P. Scott, "Left ventricular false tendons in children: prevalence as detected by 2-dimensional echocardiography and clinical significance.," *Am. J. Cardiol.*, vol. 52, no. 10, pp. 1264–6, 1983.
- [141] K. R. Sethuraman, R. Sriram, and J. Balachandar, "Left ventricular false tendons: echocardiographic incidence in India and clinical importance.," *Int. J. Cardiol.*, vol. 6, no. 3, pp. 385–7, 1984.
- [142] J. I. Brenner, K. Baker, R. E. Ringel, and M. A. Berman, "Echocardiographic evidence of left ventricular bands in infants and children.," *J. Am. Coll. Cardiol.*, vol. 3, no. 6, pp. 1515–20, 1984.
- [143] Z. Vered, R. S. Meltzer, P. Benjamin, M. Motro, and H. N. Neufeld, "Prevalence and significance of false tendons in the left ventricle as determined by echocardiography.," *Am. J. Cardiol.*, vol. 53, no. 2, pp. 330–2, 1984.
- [144] J. Malouf, W. Gharzuddine, and F. Kutayli, "A reappraisal of the prevalence and clinical importance of left ventricular false tendons in children and adults.," *Br. Heart. J.*, vol. 55, no. 6, pp. 587–91, 1986.
- [145] M. M. Cangelosi, F. Leggio, M. Gaudio, G. Stollo, M. R. Martinez, and A. Saponaro, "[The incidence and clinical significance of the echocardiographic finding of false chordae tendineae].," *Ann. Ital. Med. Int.*, vol. 7, no. 2, pp. 102–5, 1992.
- [146] M. Cocchieri and G. Bardelli, "[False chordae tendineae].," *Minerva Cardioangiolog.*, vol. 40, no. 10, pp. 353–8, 1992.

- [147] Y. Liu, N. Mi, Y. Zhou, P. An, Y. Bai, Y. Guo, C. Hong, Z. Ji, P. Ye, and C. Wu, "Transverse false tendons in the left ventricular cavity are associated with early repolarization," *PLoS ONE*, vol. 10, p. e0125173, 05 2015.
- [148] M. Gao, C. Chen, S. Zhang, Z. Qian, D. Metaxas, and L. Axel, "Segmenting the papillary muscles and the trabeculae from high resolution cardiac ct through restoration of topological handles," in *Inf. Process. Med. Imaging* (J. C. Gee, S. Joshi, K. M. Pohl, W. M. Wells, and L. Zöllei, eds.), vol. 7917 of *Lecture Notes in Computer Science*, pp. 184–195, Springer Berlin Heidelberg, 2013.
- [149] M. Hosapatna, A. D. Souza, A. Das, S. Padmashali, V. H. Ankolekar, and A. S. D. Souza, "Morphology of papillary muscles in human adults : A cadaveric study," *Ibnosina Journal of Medicine and Biomedical Sciences*, vol. 6, no. 4, pp. 168–172, 2014.
- [150] D. Ozbag, Y. Gumusalan, and A. Demirant, "The comparative investigation of morphology of papillary muscles of left ventricle in different species.," *Int. J. Clin. Pract.*, vol. 59, no. 5, pp. 529–36, 2005.
- [151] E. O. Aktas, F. Govsa, A. Kocak, B. Boydak, and I. C. Yavuz, "Variations in the papillary muscles of normal tricuspid valve and their clinical relevance in medicolegal autopsies.," *Saudi. Med. J.*, vol. 25, no. 9, pp. 1176–85, 2004.
- [152] E. H. Estes, F. M. Dalton, L. E. Mark, and H. B. D. Ii, "The anatomy and blood supply of the papillary muscles of the left ventricle," *Am. Heart. J.*, vol. 71, no. 3, pp. 356–62, 1966.
- [153] G. R. Nigri, L. J. Di Dio, and C. a. Baptista, "Papillary muscles and tendinous cords of the right ventricle of the human heart: morphological characteristics.," *Surg. Radiol. Anat.*, vol. 23, no. 1, pp. 45–9, 2001.
- [154] U. Kucuk, S. Demirkol, T. Celik, S. Balta, and M. Yokusoglu, "Three-dimensional echocardiographic imaging of biventricular false tendons mimicking hypertrophic cardiomyopathy.," *Echocardiography.*, vol. 29, no. 7, pp. E178–9, 2012.
- [155] T. Irie, K. Kurosawa, Y. Kaneko, T. Nakajima, R. Tateno, and M. Kurabayashi, "Left intraventricular dyssynchrony caused by a false tendon.," *J. Arrhythm.*, vol. 31, no. 3, pp. 163–166, 2015.

- [156] K.-J. Bathe, *Finite element procedures*. Upper Saddle River: Prentice, 1th ed., 1996.
- [157] R. A. Greenbaum, S. Y. Ho, D. G. Gibson, A. E. Becker, and R. H. Anderson, "Left ventricular fibre architecture in man.," *Br. Heart. J.*, vol. 45, no. 3, pp. 248–63, 1981.
- [158] R. D. Veenstra, R. W. Joyner, and D. A. Rawling, "Purkinje and ventricular activation sequences of canine papillary muscle. Effects of quinidine and calcium on the Purkinje-ventricular conduction delay," *Circ. Res.*, vol. 54, no. 5, pp. 500–515, 1984.
- [159] R. T. Wiedmann, R. C. Tan, and R. W. Joyner, "Discontinuous conduction at purkinje-ventricular muscle junction," *Am. J. Physiol.*, vol. 271, no. 4, pp. H1507–H1516, 1996.
- [160] D. A. Rawling and R. W. Joyner, "Purkinje and ventricular muscle cells of canine. ventricular subendocardium," *Circ. Res.*, vol. 60, no. 4, pp. 580–585, 1987.
- [161] J. Malmivuo and R. Plonsey, *Bioelectromagnetism: Principles and applications of bioelectric and biomagnetic fields*. New York: Oxford University Press, 1995.
- [162] E. Remme, A. A. Young, K. F. Augenstein, B. Cowan, and P. J. Hunter, "Extraction and quantification of left ventricular deformation modes," *IEEE Trans. Biomed. Eng.*, vol. 51, no. 11, pp. 1923–1931, 2004.
- [163] D. C. Myers and G. I. Fishman, "Molecular and functional maturation of the murine cardiac conduction system.," *Trends. Cardiovasc. Med.*, vol. 13, no. 7, pp. 289–95, 2003.
- [164] T. Mikawa and R. Hurtado, "Development of the cardiac conduction system.," *Semin. Cell Dev. Biol.*, vol. 18, no. 1, pp. 90–100, 2007.
- [165] A. Gooya, C. Davatzikos, and A. F. Frangi, "A bayesian approach to sparse model selection in statistical shape models," *SIAM J. Imaging Sci.*, vol. 8, no. 2, pp. 858–887, 2015.
- [166] S. Hang, "TetGen, a delaunay-based quality tetrahedral mesh generator," *ACM Trans. Math. Softw.*, vol. 41, no. 2, pp. 1–36, 2015.

- [167] R. S. MacLeod, C. R. Johnson, and P. R. Ershler, *Construction of an inhomogeneous model of the human torso for use in computational electrocardiography*, vol. 13, pp. 688–689. Publ by IEEE, pt 2 ed., 1991.
- [168] A. Klimke and B. Wohlmuth, “Algorithm 847: spinterp: Piecewise multilinear hierarchical sparse grid interpolation in MATLAB,” *ACM Trans. Math. Software*, vol. 31, no. 4, 2005.
- [169] A. Klimke, “Sparse grid interpolation toolbox – user’s guide,” Tech. Rep. IANS report 2007/017, University of Stuttgart, 2007.
- [170] T. Gerstner and M. Griebel, “Dimension-adaptive tensor-product quadrature,” *Computing*, vol. 71, no. 1, pp. 65–87, 2003.
- [171] K. H. W. J. ten Tusscher and A. V. Panfilov, “Modelling of the ventricular conduction system,” *Prog. Biophys. Mol. Biol.*, vol. 96, no. 1, pp. 152–170, 2008.